International
Progress Report

IPR-06-20

Äspö Hard Rock Laboratory

Äspö Task Force on modelling of groundwater flow and transport of solutes

Modelling of Task 6D, 6E, and 6F, flow and transport simulations in fracture networks

Hua Cheng
Vladimir Cvetcovic

Royal Institute of Technology
Stockholm Sweden

June 2006

Svensk Kärnbränslehantering AB
Swedish Nuclear Fuel
and Waste Management Co
Box 5864
SE-102 40 Stockholm Sweden
Tel 08-459 84 00
+46 8 459 84 00
Fax 08-661 57 19
+46 8 661 57 19

Äspö Hard Rock Laboratory

Report no.
IPR-06-20
No.
F65K
Author
Hua Cheng
Vladimir Cvetkovic
Date
June 2006
Checked by
Jan-Olof Selroos
Date
December 2006
Approved
Anders Sjöland
Date
2007-01-25

Äspö Hard Rock Laboratory

Äspö Task Force on modelling of groundwater flow and transport of solutes

Modelling of Task 6D, 6E, and 6F, flow and transport simulations in fracture networks

Hua Cheng
Vladimir Cvetcovic

Royal Institute of Technology
Stockholm Sweden

June 2006

Keywords: Flow, Transport, Tracer test, Fracture, Fracture network, Retention, Simulation, Heterogeneity

Abstract

In this report the modelling results of Task 6D, 6E, and 6F by the WRE/KTH team using the LaSAR modelling approach (Cvetkovic et al., 1999) are presented.

The Task 6D, 6E and 6F modelling is based on a semi-synthetic hydro-structural model developed within Task 6C. The three-dimensional hydro-structural model of the fracture network from Task 6C is implemented for the flow and particle tracking simulations. All of the fracture structures (including the background fractures) have been accounted for in the implementation.

Three factors influence the breakthrough curves: (1) the distribution of water residence time τ and hydrodynamic control parameter β, (2) the surface sorption coefficient K_a, and (3) the material retention parameter group κ. An inverse-Gaussian distribution is assumed for τ, the moments of τ are obtained from the ensemble mean and variance of the simulated τ values. β is assumed to have a linear relationship with τ, and the linear relation is obtained by fitting the simulated τ - β data. K_a is calculated from the distribution coefficient K_d for fracture coatings. κ is essentially determined by the porosity θ and by K_d of the rock matrix. An effective value of θ and K_d for the entire rock matrix is obtained by accounting for in-depth heterogeneity of the retention parameters. The parameters θ, K_d (therefore κ) are both tracer-dependent and penetration-depth dependent.

The tracers included in the model are I-129, Ca-47, Cs-137, Ra-226, Tc-99 and Am-241. Breakthrough curves (BTCs) for the injection conditions defined by the Task specifications (e.g., experimental injection, extended pulse injection, Dirac pulse injection, etc) are provided. The breakthrough times at 5%, 50%, and 95% mass recovery and maximum release rates are also given.

Sammanfattning

I den här rapporten presenteras WRE/KTH:s modelleringsresultat för Task 6D, 6E och 6F som utförts med LaSAR modelleringsmetodik (Cvetkovic et al., 1999).

Modelleringen i Task 6D, 6E och 6F baserar sig på en semi-syntetisk hydrostruktur-modell som skapades inom Task 6C. Den tredimensionella hydrostrukturmodellen av spricknätverket från Task 6C implementerades för simulering av flöde och partikeltransport. Alla sprickor (inklusive bakgrundssprickor) har tagits hänsyn till vid implementeringen.

Tre faktorer påverkar genombrottskurvorna: (1) fördelningen av uppehållstiden för vatten τ and den hydrodynamiska kontrollparametern β, (2) ytsorptionskoefficienten K_a, och (3) den materialberoende retentionsparametern κ-värdet. En invers Gaussisk fördelning antas för τ, momenten för τ erhålls från ensemblemedelvärde och varians av de simulerade τ-värdena. β antas ha ett linjärt samband med τ, och det linjära sambandet erhålls genom anpassning till simulerade τ - β data. K_a beräknas från fördelningskoefficienten K_d för det material som sitter på sprickväggarna. κ bestäms huvudsakligen av porositeten θ och av K_d för bergmatrisen. Ett effektivt värde för θ och K_d för hela bergmatrisen erhålls genom att beakta djupberoende heterogenitet hos retentionsparametrarna. Parmametrarna θ, K_d (och därmed κ) är både spårämnesberoende och penetrationsdjupsberoende.

De spårämnen som ingår i modellen är I-129, Ca-47, Cs-137, Ra-226, Tc-99 och Am-241. Genombrottskurvor för de injektionsförhållanden som definierats i specifikationen för Task 6 (t ex experimentell injektion, förlängd pulsinjektion, Dirac pulsinjektion, etc) presenteras. Genombrottstiderna vid 5%, 50%, och 95% massgenombrott och maximala utsläppshastigheterna av spårämnen presenteras också.

Contents

1 Introduction **17**
1.1 Background 17
1.2 Objectives 19
1.3 Outline of report 19

2 Modelling Tasks **21**
2.1 Task 6C - Semi-synthetic hydro-structural model 21
2.2 Task 6D – Block scale transport on a tracer test time scale 22
2.2.1 The TRUE Block Scale tracer test C2 22
2.3 Task 6E – Block scale transport on a PA time scale 22
2.4 Task 6F – Test bench 23
2.5 Task 6F2 - Sensitivity study 23

3 Model description **25**
3.1 Implementation of the Task 6C semi-syntehtic hydrostructural model 25
3.2 Geometrical description 25
3.2.1 Fracture network 25
3.2.2 Pore space 32
3.3 Flow model 37
3.3.1 Processes considered 37
3.3.2 Mathematical description 37
3.3.3 Numerical implementation 38
3.3.4 Parameters 40
3.4 Transport model 40
3.4.1 Processes considered 40
3.4.2 Mathematical description 40
3.4.3 Numerical implementation 43
3.4.4 β and τ relationship 44
3.4.5 Parameters 49

4 Task 6D **53**
4.1 Modelling strategy 53
4.2 Model calibration 53
4.3 Results 54
4.3.1 Flow 54
4.3.2 Transport 56
4.4 Sensitivity analysis 59
4.4.1 Effect of discretization on β and τ parameters 59
4.4.2 Effects of the background structures 61
4.4.3 Depth-dependence of the porosity θ, the diffusivity D and sorption coefficient K_d 63

5 Task 6E **71**
5.1 Modelling strategy 71
5.2 Model calibration 71
5.3 Depth-dependence of the retention parameters 71
5.3.1 Complexity factor 71
5.3.2 Effective retention parameters 74
5.4 Results 79
5.4.1 Flow 79
5.4.2 Transport 83
5.4.3 Sensitivity analysis 90

6 Task 6F **91**
6.1 Modelling strategy 91
6.2 Model description 91
6.2.1 Flow model 91
6.2.2 Transport model 92
6.3 Calculated cases 93
6.4 Effective values of θ and K_d 93
6.4.1 Structure 1S 93
6.4.2 Structure 4S 96
6.5 Results 99

7 Task 6F2 **101**
7.1 Modelling strategy 101
7.2 Model description 102
7.3 Correlation between β and τ 102
7.3.1 Analytical solution 102
7.3.2 Calculated cases 102
7.4 Results 103
7.5 Correlation between β and Q 105
7.5.1 Analytical solution 105
7.5.2 Simulation cases 105
7.5.3 Results 106

8 Discussion and conclusions **109**
8.1 Summary and discussions of the results 109
8.1.1 Flow-dependent parameters 109
8.1.2 Interpretation of the immobile zones in the rock matrix 109
8.1.3 Complexity factor 110
8.1.4 Heterogeneity of retention parameters 110
8.1.5 Results of Task 6D 110
8.1.6 Results of Task 6E 111
8.2 Main conclusions 111
8.3 Lessons learned and implications for Task 6 objectives 112

9 References **113**

List of Tables

Table 3-1.	Properties of geological structure of Type 1.	33
Table 3-2.	Properties of geological structure of Type 2.	34
Table 3-3.	Porosity profile in depth for structure Type 2.	34
Table 3-4.	Porosity depth profile in depth for Part A of the rock matrix of structure Type 1.	36
Table 3-5.	Porosity depth profile in depth for Part B of the rock matrix of structure Type 1.	36
Table 3-6.	Data for source section used in Task 6E. Coordinates are given in the ÄSPÖ96 system.	44
Table 3-7.	Moments of water residence time for Task 6D.	46
Table 3-8.	Summary of simulated τ and β moments for Task 6E.	48
Table 3-9.	Effective diffusivities for individual tracers in contact with different rock materials. The diffusivities have been calculated using the formation factor, F, and the tabulated water diffusivities, D_w.	50
Table 3-10.	Summary of K_d values for different rock materials in contact with the TRUE Block Scale groundwater.	51
Table 3-11.	Summary of surface sorption coefficient K_a.	51
Table 4-1.	Parameters used for calculating the BTCs from the calibration procedure.	54
Table 4-2.	Drawdown at injection and pumping borehole for Task 6D.	55
Table 4-3.	Moments of water residence time for Task 6D.	55
Table 4-4.	Moments of parameter β for Task 6D.	56
Table 4-5.	Times of 5%, 50% and 95% mass recovery for the measured injection for Task 6D.	57
Table 4-6.	Breakthrough times of recovery of 5, 50 and 95% for Dirac pulse injection for Task 6D.	58
Table 4-7.	Maximum release rate for measured injection for Task 6D.	59
Table 4-8.	Maximum release rate for Dirac pulse injection for Task 6D.	59
Table 4-9.	Moments of τ and β from the simulations with finer and coarser discretizations.	60
Table 4-10.	Moments of τ and β with and without background structures.	62

Table 4-11. Initial retention parameters from the altered zone and times of 85% mass recovery from the BTCs in Figure 4-9. 64

Table 4-12. Penetration depths at 15% relative concentration of different tracers in structure Type 2. 65

Table 4-13. Penetration depths, effective porosities and effective K_d values in structure Type 1. 67

Table 4-14. Travel time and transport distance (example from one particle). 68

Table 4-15. Values of θ and K_d obtained by simplification of the deterministic and background structures. 68

Table 5-1. Complexity factors assigned to the synthetic structures in Task 6C. 72

Table 5-2. Assigned values of the complexity factor used in Task 6E. 72

Table 5-3. Complexity factors and the geological structure types for the example flow path shown in Figure 3-18. 73

Table 5-4. Summary of the average geological type, the complexity factors, and the percentage of each structure type at three CPs. 74

Table 5-5. Initial values of sorption and diffusion parameters used in Task 6E at x = 1920 m (Altered zone) and the times for 85% mass recovery. 75

Table 5-6. Penetration depths at 15% relative concentration of different tracers in structure Type 2 and the effective porosities based on the depths. 77

Table 5-7. Penetration depths and effective K_d values. 78

Table 5-8. Summary of effective sorption and diffusion parameters at x = 1920 m based on penetration depths. 78

Table 5-9. Summary of effective sorption and diffusion parameters at x = 1880 m and x = 1800 m (from intact rock). 79

Table 5-10. Times for 5%, 50% and 95% mass recovery of the injected mass at x = 1920 m for the extended pulse injection. 87

Table 5-11. Times for 5%, 50% and 95% mass recovery of the injected mass at x = 1880 m for the extended pulse injection. 87

Table 5-12. Times for 5%, 50% and 95% mass recovery of the injected mass at x = 1800 m for the extended pulse injection. 87

Table 5-13. Times for 5%, 50% and 95% mass recovery of the injected mass at x = 1920 m for the Dirac pulse injection. 89

Table 5-14. Times for 5%, 50% and 95% mass recovery of the injected mass at x = 1880 m for the Dirac pulse injection. 89

Table 5-15. Times for 5%, 50% and 95% mass recovery of the injected mass at x = 1800 m for the Dirac pulse injection. 90

Table 5-16. Maximum release rates for the extended pulse injection (Bq/y). 90

Table 5-17. Maximum release rates for the Dirac pulse injection (1/y). 90

Table 6-1. Properties of selected structures. 91

Table 6-2. Head boundary conditions for different cases. 91

Table 6-3. Temporal moments and slope k for Structure 1S. 92

Table 6-4. Temporal moments and slope k for Structure 4S. 92

Table 6-5. Simulation cases for Task 6F. 93

Table 6-6. Initial values of θ and K_d for Structure 1S. 93

Table 6-7. Initial retention parameters and times of 85% mass recovery for Cases A1 and B1. 93

Table 6-8. Initial retention parameters and times of 85% mass recovery for Cases C1 from intact rock. 94

Table 6-9. Penetration depths and effective parameters for Case A1. 94

Table 6-10. Penetration depths and effective parameters for Case B1. 95

Table 6-11. Penetration depths and effective parameters for Case C1. 96

Table 6-12. Summary of effective retention parameters for Structure 1S. 96

Table 6-13. Initial values of θ and K_d for Structure 4S. 96

Table 6-14. Initial retention parameters and times of 85% mass recovery for Cases A2 from Altered zone. 96

Table 6-15. Penetration depths and effective parameters for Case A2. 97

Table 6-16. Initial retention parameters and times of 85% mass recovery for Cases B2 from Altered zone. 97

Table 6-17. Penetration depths and effective parameters for Case B2. 98

Table 6-18. Summary of effective retention parameters for Structure 4S. 98

Table 6-19. β values for all cases in Task 6F. 99

Table 6-20. Maximum release rates for Task 6F. 100

Table 7-1. Cases investigated for β and τ correlation. 102

Table 7-2. Comparison of statistical moments of normalized β and τ. 105

Table 7-3. Simulation cases for β and Q correlation. 105

List of Figures

Figure 3-1. A schematic representation of a single fracture. The green area is the fracture zone. The rest is the rock matrix. The water flows only in the fracture zone. 26

Figure 3-2. Velocity calculation along four sides of a square element. 26

Figure 3-3. Two interacting fractures in a 2-dimensional domain. The purple elements are the FIZ. 27

Figure 3-4. A single fracture in a 3-dimensional domain. 28

Figure 3-5. Flow into and out of an element and the velocities on the six faces of the element. 28

Figure 3-6. Two fractures interacting in a 3-dimensional domain. 29

Figure 3-7. Deterministic 100 m scale structures in the Task 6C model. 30

Figure 3-8. Deterministic and synthetic structures in the Task 6C model. 30

Figure 3-9. Background fractures in the Task 6C model. The blue region represents fractures of the Shallow set. The yellow region is the NNW set of fractures. 31

Figure 3-10. Visualization of the geological structure Type 1 (fault) (reproduced from Dershowitz et al., 2003). 32

Figure 3-11. Visualization of the geological structure Type 2 (non-fault) (reproduced from Dershowitz et al., 2003). 33

Figure 3-12. Distribution of the retention zones in structure Type 2. 35

Figure 3-13. Distribution of the retention zones in structure Type 1. 36

Figure 3-14. Configuration of the inner domain in the second step flow simulation. 38

Figure 3-15. Boundary conditions for the 200 m cubic block flow simulation. 39

Figure 3-16. Scattergram of the simulated τ and β data in the inner 100 m block including all structures for Task 6D. 45

Figure 3-17. Scattergram of simulated τ and β at x = 1920 m. 46

Figure 3-18. Scattergram of simulated τ and β at x = 1880 m. 47

Figure 3-19. Scattergram of simulated τ and β at western boundary. 48

Figure 3-20. Comparison of τ and β scattergrams at three CPs 49

Figure 4-1. Visualization of two flow paths for Task 6D. 54

Figure 4-2. Water residence time distribution for Task 6D. The red line is the inverse-Gaussian distribution fitting with the moments from the corresponding simulation values. 55

Figure 4-3. Cumulative distribution function of β parameter for Task 6D. 56

Figure 4-4. Calculated BTCs for measured injection for Task 6D. Lines are the simulated BTCs. Symbols are the measured BTCs. 57

Figure 4-5. Calculated BTCs for Dirac pulse injection for Task 6D. 58

Figure 4-6. Effects of discretization on β and τ simulation results. The red symbols are β and τ results from finer discretization. The green symbols are those for coarser discretization. 60

Figure 4-7. BTCs for coarser and finer discretizations. The solid lines are the modeled BTCs from the finer discretization. The dashed lines are the modelled BTCs from the coarser discretization. The symbols are the measured data. 61

Figure 4-8. Comparison of τ and β scattergrams with and without background structures. The green symbols represent τ and β scattergram with only the deterministic structures. The red symbols designate τ and β scattergram with all structures. 62

Figure 4-9. BTCs with and without background fractures. The solid lines are the modelled BTCs with all structures. The dashed lines are the modelled BTCs with only deterministic structures. The symbols are the measured data. 63

Figure 4-10. Penetration profiles for all tracers in the altered zone in structure Type 2. 65

Figure 4-11. Penetration profiles Part A of the matrix in structure Type 1. 66

Figure 4-12. Penetration profiles for Part B of the matrix in structure Type 1. 66

Figure 4-13. Comparison of modelled BTCs based on the parameters from the calibration (solid lines with the parameters from Table 4-1), and the BTCs based on the parameters from the penetration analysis (dashed lines with the parameters from Table 4-15). 69

Figure 5-1. An example of a flow path illustrating the calculation of the percentage of each geological structure type in the flow path. 73

Figure 5-2. Penetration profiles for all of the tracers in the altered zone in structure Type 2. The profiles are calculated at the times of 85% mass recovery shown in Table 5-5. The times are 936y for I-129, 3969y for Ca-47, 7.82E+5y for Ra-226, 2.05E+6y for Cs-137, 4.88E+6y for Tc-99 and 1.45E07 for Am-241. 75

Figure 5-3. Penetration profile for Part A of the matrix in structure Type 1. The profiles are calculated at the times of 85% mass recovery. The times are 936y for I-129, 3969y for Ca-47, 7.82E+5y for Ra-226, 2.05E+6y for Cs-137, 4.88E+6y for Tc-99 and 1.45E07 for Am-241. 76

Figure 5-4. Penetration profile for Part B of the matrix in structure Type 1. The profiles are calculated at the times of 85% mass recovery. The times are 936y for I-129, 3969y for Ca-47, 7.82E+5y for Ra-226, 2.05E+6y for Cs-137, 4.88E+6y for Tc-99 and 1.45E07 for Am-241. 76

Figure 5-5. Visualization of flow paths at x = 1920 m. 79

Figure 5-6. Visualization of flow paths at x = 1880 m. 80

Figure 5-7. Visualization of flow paths at x = 1800 m. 80

Figure 5-8. Cumulative distribution function (CDF) and complementary Cumulative distribution function (CCDF) of the water residence time at x =1920 m. 81

Figure 5-9. Cumulative distribution function (CDF) and complementary Cumulative distribution function (CCDF) of the water residence time at x = 1880 m. 81

Figure 5-10. Cumulative distribution function (CDF) and complementary Cumulative distribution function (CCDF) of the water residence time at x = 1800 m. 82

Figure 5-11. Cumulative distribution function (CDF) and complementary Cumulative distribution function (CCDF) of the β parameter at x = 1920 m. 83

Figure 5-12. Cumulative distribution function (CDF) and complementary Cumulative distribution function (CCDF) of the β parameter at x = 1880 m. 84

Figure 5-13. Cumulative distribution function (CDF) and complementary Cumulative distribution function (CCDF) of the β parameter at x = 1800 m. 84

Figure 5-14. Calculated BTCs for extended pulse injection at x = 1920 m. The red line is for I-129, green line for Ca-47, blue for Ra-226, cyan for Cs-137, orange for Tc-99 and purple for Am-241. 85

Figure 5-15. Calculated BTCs for extended pulse injection at x=1880 m. The red line is for I-129, green line for Ca-47, blue for Ra-226, cyan for Cs-137, orange for Tc-99 and purple for Am-241. 86

Figure 5-16. Calculated BTCs for extended pulse injection at x = 1800 m. The red line is for I-129, green line for Ca-47, blue for Ra-226, cyan for Cs-137, orange for Tc-99 and purple for Am-241. 86

Figure 5-17. Calculated BTCs for the Dirac pulse injection at x = 1920 m. 88

Figure 5-18. Calculated BTCs for the Dirac pulse injection at x = 1880 m. 88

Figure 5-19. Calculated BTCs for the Dirac pulse injection at x = 1800 m. 89

Figure 6-1. Description of geometry and boundary conditions (Example for structure 4S). 92

Figure 6-2. Penetration profiles for Case A1. 94

Figure 6-3. Penetration profiles for Case B1. 95

Figure 6-4. Penetration profiles for Case C1. 95

Figure 6-5. Penetration profile for Case A2. 97

Figure 6-6. Penetration profiles for Case B2. 98

Figure 6-7. Breakthrough curves for various cases in Structure 1S. 99

Figure 6-8. Breakthrough curves for Structure 4S. 100

Figure 7-1. (a) Configuration of three connected fractures; (b) a typical realization of trajectories with W = 5.0 m. 101

Figure 7-2. Comparison of simulated β and τ correlation for the cases considered in Table 7-1 and analytical solution (7-1). (a) Case 1; (b) Case 2; (c) Case 3; (d) Case 4; (e) Case 5; (f) Case 6. Solid lines are power-law fits with correlation coefficient in parenthesis. Dashed lines are analytical solution (7-1). Note that β and τ are normalized by β_0 and τ_0 defined in Paper VI in Cheng, (2005). 104

Figure 7-3. Scattergram of normalized β and Q for the four cases considered in Table 7-3 and for W=5.0 m: (a) Case 1; (b) Case 2; (c) Case 3; and (d) Case 4. Solid lines are the best power-law fits. Dashed lines are analytical solution (7-2). 106

Figure 7-4. Scattergram of normalized β and Q for the four cases considered in Table 7-3 and for W=0.1 m: (a) Case 1; (b) Case 2; (c) Case 3; and (d) Case 4. Solid lines are the best power-law fits. Dashed lines are analytical solution (7-2). 107

1 Introduction

1.1 Background

In Sweden as well as in many other countries, the spent nuclear fuel from nuclear power plants will be deposited in deep geological formations. Some suitable geological formations are the crystalline granitic rocks. The objective of this disposal option is to guarantee that no or only acceptably small amounts of radionuclides reach the biosphere over long time, up to hundreds of million years. In a repository of spent fuel, the metal canister and the engineered buffer (compact bentonite clay and backfill materials) form man-made barriers for the retention of radionuclides. The surrounding crystalline rocks will form the natural barrier since water access to the repository cannot be excluded and integrity of the canister and the buffer cannot be assumed over the long time period required for safety. Realistic estimates and predictions of the geosphere retention capacity are thus critical for any safety assessment of a repository.

Transport of radionuclides in crystalline rocks is governed by the flowing groundwater in the available fracture system. The crystalline rocks themselves will provide retardation of radionuclide transport by dispersion, matrix diffusion with associated sorption on inner pore surfaces of the rock matrix, and sorption on different rock materials adjacent to water-conducting fracture surfaces. To facilitate the understanding of the migration and retention properties of the crystalline rocks, injection-pumping tracer test experiments have been conducted by several nuclear waste management agencies in their underground laboratories (e.g., for SKB, see Winberg et al., 2000; Andersson et al., 2002b; and for Nagra, see Frick et al., 1992; Haderman and Heer, 1996; Heer and Smith, 1998). In the following, we will present only the SKB tracer test experiments carried out at the Äspö Hard Rock Laboratory (HRL). The underground facilities provide an opportunity for research, development and demonstration in a realistic and relatively undisturbed crystalline rock environment at depths comparable to that of a future repository.

To improve the understanding of radionuclide retention mechanisms in the Swedish crystalline rocks, the Swedish Nuclear Fuel and Waste Management Company (SKB) has initiated a tracer test program referred to as Tracer Retention Understanding Experiments (TRUE) (Bäckblom and Olsson, 1994). The basic idea of the TRUE program is to perform a series of experiments with increasing complexity in terms of the involved retention processes and spatial scale, and to verify the capability of various modelling approaches in predicting radionuclide migration and retention. The TRUE experiments were performed at the Äspö Hard Rock Laboratory (HRL) in southeastern Sweden. The TRUE program has progressed in different stages. The first stage (TRUE-1) was focused on a detailed scale (<10 m) in a single feature (e.g., Cvetkovic et al., 2000, Winberg et al., 2000). The basic objective of TRUE-1 was to perform and analyze transport experiments with non-sorbing and sorbing tracers in a discrete singular fracture in crystalline rock. The second stage was performed on a block scale (10 – 50 m) with possible multiple geological structures (e.g., Cvetkovic and Cheng, 2002, Poteri et al., 2002). The general objective of the Block Scale tracer test was to provide data and to predict by modeling the transport in a fracture network in a block scale (Andersson et al., 2002b). The locations of the detailed scale test and the block scale test at the Äspö HRL were shown in Figure 1.3 in Winberg et al. (2000). To further address

the questions of fracture structure complexities that had not been clearly answered in the TRUE Block Scale experiments, the TRUE Block Scale Continuation (BSC) experiments were also conducted. The TRUE BSC aimed at performing sorbing tracer tests involving background fractures and subsequent predictions and evaluations (Andersson et al., 2005; Cheng and Cvetkovic, 2005).

The rock volume of the Äspö area is mainly of granitic composition with different types of Småland granite belonging to the Transcandinavian Igneous Belt. At the depth of the Äspö drift the Småland granite grades into the more mafic Äspö diorite. Faults and ductile zones were formed in association with some old metamorphism and subsequent replacement of younger granites. These faults and older ductile zones were reactivated several times. Fracture zones at Äspö have a wide range of orientations and styles.

Several hydraulic features have been defined at the TRUE-1 (the detailed scale test) site, for example, Feature A. Feature A was in the main focus of the TRUE-1 tracer test and modeling. Feature A is a reactivated mylonite, i.e. a ductile mylonite that has later experienced brittle deformation. The brittle reactivation is associated with one major fault plane which is assumed to represent the water conducting part of Feature A. Tracer tests have been performed in several flow paths in Feature A (and one in Feature B) over distances ranging from about 2 m up to 10 m between injection and withdrawal points. Various test set-ups, either in radially converging or dipole flow geometry, were used. Among those test set-ups, the results from the set-ups of STT-1, STT-1b and STT-2 have been evaluated by modelling approaches. (Winberg et al., 2000; Cvetkovic et al., 2000).

During the period of mid 1996 through mid 1999 a 200×250×100 m rock volume was characterised at the Äspö HRL with the purpose of furnishing the basis for successful tracer experiments in a network of conductive structures at the block scale (10 - 100 m) (Andersson et al., 2002a; Andersson et al., 2002b; Poteri et al., 2002; Winberg et al., 2003). The TRUE Block Scale site is located in the southwestern part of the experimental level at the Äspö HRL. A comprehensive series of cross-hole hydraulic interference and tracer dilution and tracer tests were carried out.

There were three tracer test phases: Phase A was focused on identifying the best pumping (sink) section (Andersson et al, 2000a), Phase B was devoted to demonstrating sufficiently high mass recovery of non-sorbing species to allow usage of radioactive sorbing tracers (Andersson et al, 2000b), and Phase C (Andersson et al, 2001) included performance of four injections with radioactive sorbing tracers in three sections. The results of phase C tests have been extensively modelled and evaluated (Poteri et al., 2002, Cvetkovic and Cheng, 2002).

In connection with the TRUE program, an international cooperation has been established in the framework of Äspö Task Force on groundwater flow and transport. A series of tasks focusing on different aspects of test and modelling within the program have been defined.

Task 6 seeks to provide a connection between site characterisation (SC) and performance assessment (PA). Task 6 aims at performing performance assessment (PA) modelling using site characterization (SC) data. The PA modelling approach and the SC modelling approach are based on similar physical concepts and processes but focus on different aspects of the transport. The SC approach focuses on the detailed and site-specific modelling of experiments in a rock volume. The PA approach, on the other

hand, accounts for different scenarios of the repository evolution after the closure of the repository. In Task 6, modelling approaches have been applied for the SC scale boundary conditions and for the PA scale boundary conditions, respectively.

The first three sub-tasks within Task 6 were: Task 6A, 6B and 6B2 (Cheng and Cvetkovic, 2003). The three subtasks aimed at performing both the SC and PA modelling approaches on a detailed spatial scale (5 - 10 m) using the results of the tracer test experiments in the TRUE-1 test, especially from the set-ups of STT-1b.

The subsequent Task 6C, Task 6D and Task 6E have all been based on data from several programs at the Äspö HRL. The models have mainly employed the networks of major conductive features that were identified in the Äspö TRUE Block Scale experiments. The details of the different tasks will be described in the next chapter of this report.

Task 6F is a "test bench" for comparing different models used in Task 6. Task 6F2 is a sensitivity study.

1.2 Objectives

Task 6D and 6E of the Äspö Task Force consist of a set of numerical modelling approaches. All modelling approaches use a semi-synthetic hydro-structural model developed in Task 6C (Dershowitz et al., 2003) as a common basis for the performance assessment (PA) modelling and the site characterisation (SC) modelling. The results of these simulations can then be readily compared with each other to fulfill the following generic requirements in Task 6 (Benabderrahmane et al, 2000):

1. To assess the legitimacy of different simplifications used in PA models,
2. To determine if the tracer test and the flow experiments can provide constraints for the range of parameters used in PA models,
3. To provide support for the design of site characterisation programs which will ensure that the results thus obtained have optimal values for use in the performance assessment calculations,
4. To facilitate a better understanding of the site-specific flow and transport behaviour at different scales using site characterisation models.

1.3 Outline of report

In this report the modelling results of Task 6D, 6E, 6F and 6F2 by the WRE/KTH team using Lagrangian Stochastic Advection-Reaction (LaSAR) approach (Cvetkovic et al., 1999, 2000) are presented. The LaSAR approach has been used in the modelling work in the first stage (detailed scale) of the TRUE program (Cvetkovic et al., 2000). The same approach has later been extended to modelling a network of fractures in the second stage (block scale) of the TRUE program (Cvetkovic and Cheng, 2002), and for modelling the transport involving background fracture in TRUE Block Scale Continuation project (Cheng and Cvetkovic, 2005).

In Chapter 2, the modelling tasks of Task 6 included in this report will be presented, including Task 6D, 6E, 6F and 6F2. Task 6C hydro-structural model will be summarized. The tracer test C2 will also be presented. In Chapter 3, we will present implementations of the Task 6C semi-synthetic, hydro-structural model. The flow and transport models will be described, the modelling concepts and procedures will be presented. In Chapter 4, we summarize the modelling strategy and results as well as the results of the sensitivity study for Task 6D. The sensitivity study includes the effect of discretization and the effect of the background fracture on the modelled breakthrough curves (BTCs). We will also investigate the effect of retention heterogeneity and provide estimates on depth-dependent retention parameters. In Chapter 5, we present the modeling strategy and results for Task 6E. The modeling results for Task 6F will be presented in Chapter 6. In Chapter 7, the modeling results for Task 6F2 are summarized. Finally in Chapter 8 we discuss the results, draw conclusions and summarize the lessons learned.

2 Modelling Tasks

The tasks are performed by the Task Force modelling groups. The tasks have been performed in different phases ranging from simple to more complicated fracture systems (Benabderrahmane et al., 2000). The complexity of the fracture systems varies from one single fracture to a fracture network, from small spatial scales (e.g., 5m) to large spatial scales (e.g., 100 m), and from short time scales (a few hours) to long time scales corresponding to that used in the performance assessment.

A more detailed description of Tasks 6C, 6D, 6E, 6F and 6F2 will be given in the following sections.

2.1 Task 6C - Semi-synthetic hydro-structural model

In Task 6C a semi-synthetic hydro-structural model of a fracture network of conductive structures has been developed based on the geological characteristics at the TRUE Block Scale site at the Äspö HRL (Dershowitz et al., 2003, referred to as Task 6C model hereafter). Task 6C model focused on a 200 m × 200 m × 200 m cubic rock block. The block is within the domain of the 2000 m site scale model. The Task 6C model forms the basis for the Task 6D and 6E modelling. The Task 6C model includes three types of structures: deterministic structures, synthetic structures and background structures. The deterministic structures are the major structures identified at the TRUE Block Scale site. The synthetic structures and many background structures are characterized from other site investigations like the Prototype Repository site.

The database of the Prototype Repository project includes ten high quality cross-hole interference tests. No tracer tests have been performed at this site. The deterministic structures consist of only 2-3 subparallel, vertical structures and do not suffice to form a conducting network. Some stochastic background fractures have to be used to achieve block-scale connectivity.

At the TRUE Block Scale site, however, the hydro-structural model can be built up based on the connected major deterministic structures. The database generated from many projects at this site includes the cross-hole hydraulic interference, tracer dilution and tracer tests.

Two types of microstructural models for conductive structures were defined in the Task 6C model: Type 1 (Fault) and Type 2 (Non-fault). Type 1 includes structures associated with faulting such as fault gouge, cataclasite and /or mineral coatings. Type 2 is not associated with faulting and consists of intact wall rock with some alteration. A combination of the two types could also be involved in the model. Depending on how a given structure is formed from the two structure types, a complexity factor is assigned to each macrostructure in the Task 6C model. The complexity factor varies between 1 and 5.

2.2 Task 6D – Block scale transport on a tracer test time scale

Task 6D aims at simulating solute transport of C2 test in TRUE Block Scale project using Task 6C model. The tracers are injected through one structure (structure #23) and pumped through another structure (structure #21). The tracers are transported through a network of several structures. The prescribed head boundary condition is obtained from the Task 6D data delivery. The simulation will be performed for both experimental injection and Dirac pulse injection. The breakthrough curves (BTCs) of the following tracers are simulated: I-129, Ca-47, Cs-137, Ra-226, Tc-99 and Am-241.

2.2.1 The TRUE Block Scale tracer test C2

The tracer test C2 was performed at the TRUE Block Scale site (Andersson et al., 2002b). The tracers were injected in borehole KI0025F03:P7 and pumped from borehole KI0023B. The structures 23, 22,20 and 21 were involved in the C2 test. The tracers in the C2 test included Re-186 (conservative), Ca-47 (slightly sorbing), Ba-131 (moderately sorbing) and Cs-137 (strongly sorbing).

In the Task 6D modelling, the injection time history of I-129 is assumed to be identical to that of Re-186. The simulated BTC of I-129 may be compared to that of Re-186 from the C2 experiments. The injection time histories of Ra-226, Tc-99 and Am-241 are assumed to be identical to that of Cs-137. However no comparisons can be made for them with the experimental results.

2.3 Task 6E – Block scale transport on a PA time scale

Task 6E extends the Task 6D transport calculations to a reference set of PA time scales and boundary conditions (Elert and Selroos, 2002, 2004). Tasks 6E also deals with the modelling of solute transport over longer distances including several geological features. The basis for the modelling of Task 6E is also the Task 6C model (Dershowitz et al., 2003) over 200 m cubic block. The flow and transport would occur in a number of deterministic features and many background fractures. The water flow will occur under natural gradient boundary conditions giving water travel times corresponding to the "*Performance assessment time scale"*.

Simulations of tracer transport in Task 6E are to be undertaken at post-closure conditions. The boundary conditions are simplified with fixed head boundary conditions on the east and the west sides of the 200 m block, while the other sides are treated as no-flow boundaries:

- The eastern side (X=2000 m): Head=1 m
- The western side (X=1800 m): Head=0 m

The boundary conditions will give a gradient from east to west with a magnitude of about 0.5%. In Task 6D the gradient was about 1000% over the Euclidean distance.

The tracer source section has been chosen to be at the injection point of tracer test C2 in the deterministic feature 23D, i.e. at the same location as in Task 6D. This section is located near the center of the 200 m block. The source is assumed to be an intersecting fracture with a linear extension of 3 m. The source would be modelled as several point sources on a line.

In Task 6E, the breakthrough curves of the tracers I-129, Ca-47, Cs-137, Ra-226, Tc-99 and Am-241 are simulated. Simulations are performed for both Dirac pulse input and an extended pulse of 1 MBq/year with duration of 1000 years.

The breakthrough curves are simulated at the following planes: (1) the intersection with a vertical plane defined by Easting = 1920 m, i.e. a Cartesian distance about 10 m from the release point; (2) the intersection with a vertical plane defined by elevation = 1880 m, i.e. a Cartesian distance about 50 m from the release point; (3) the western boundary of the 200 m block.

2.4 Task 6F – Test bench

Task 6F is aimed as "a test bench" for comparing different models used in Task 6. The task consists of simulating flow and transport in a purely single Type 1 and a Type 2 structure, respectively. The structures will follow the geometrical description from Task 6C.

The following two structures are selected for the purpose of Task 6F:

- Geological Type 1: Synthetic feature 1S
- Geological Type 2: Synthetic feature 4S

For the purpose of this exercise the fracture should be assumed to have homogeneous properties. The effect of heterogeneity is to be studied within the Task 6F2 Sensitivity analysis.

A selection of tracers from Task 6E will be used, i.e. I-129, Cs-137 and Am-241. The transport and sorption data for these tracers should be as prescribed for Task 6E.

The source term is a Dirac pulse from a spatially extended source as in Task 6E. Breakthrough curves over a "collection line" at a distance of 20 meters downstream will be calculated for the performance measures.

2.5 Task 6F2 - Sensitivity study

We study the impact of global and internal heterogeneities on the statistical properties (moments) on β, τ and Q and their correlations. We construct a series of stepped single fractures and study the correlation between β and τ, between β and Q for different degrees of global and internal heterogeneities. We also study the effect of width of source section W on β and Q correlation.

3 Model description

3.1 Implementation of the Task 6C semi-syntehtic hydrostructural model

In this section, we will describe how to represent a single fracture and a fracture network using staggered elements in a 2-dimensional domain and in a 3-dimensional domain in our model. The 2-dimensional representation will not be used in our modelling work, but is included here for an introductory description and visual presentation of the representation methodology. The methodology will eventually be used for the fracture network in a 3-dimensional domain.

3.2 Geometrical description

3.2.1 Fracture network

A single fracture in a 2-dimensional domain

A single fracture is assumed to be located in a 2-dimensional rectangular rock plate. The rock plate has a length L and a width W, and is discretized into M×N square elements. It should be noted that the fracture is not represented explicitly in the model, but different values of transmissivity will be assigned to the elements that build up the fracture. The aperture of the fracture is related to the transmissivity by Doe's law (e.g., Outters and Shuttle, 2000):

$$T = 4e^2 \qquad (3\text{-}1)$$

where T is the transmissivity ($m^2\ s^{-1}$) and e is the aperture (m).

The fracture itself is represented by a series of sequentially connected staggered elements (the green elements in Figure 3-1) along the direction of the real fracture (the red line in Figure 3-1). Two distinct regions in the rock plate have also been indicated in the figure. The first region is the fracture (the green elements), and the second region is the rock matrix (the rest of the elements in Figure 3-1). It should be noted that the size of the elements is a result of numerical discretization and does not represent the size of the fracture aperture. The size of the aperture is related to the transmissivity that is assigned different values for different elements that represent either the fracture or the rock matrix.

In all elements of the rock matrix, no flow is assumed, i.e., they are impermeable (inactive in numerical simulations).

Given certain boundary conditions, the head distribution can be solved for the domain of the rock plate. The velocity of the groundwater flow is then solved by Darcy's law along each of the four sides of every element (Figure 3-2).

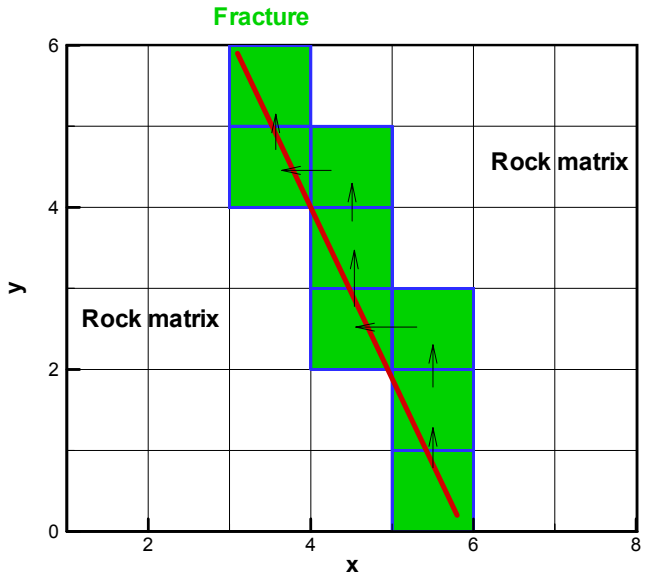

Figure 3-1. *A schematic representation of a single fracture. The green area is the fracture zone. The rest is the rock matrix. The water flows only in the fracture zone.*

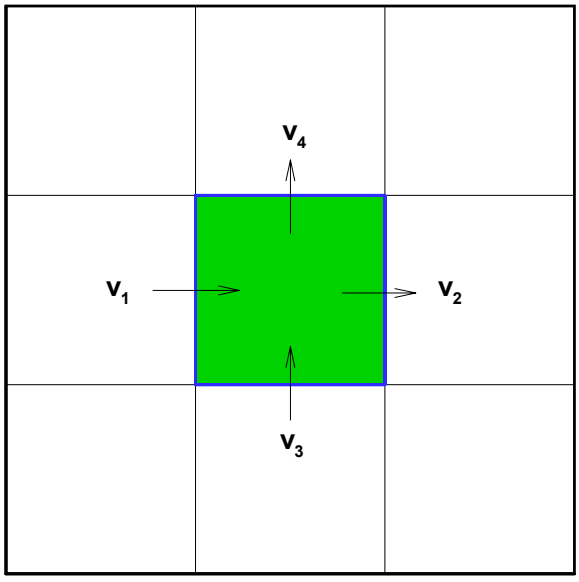

Figure 3-2. *Velocity calculation along four sides of a square element.*

Fracture network and fracture intersection zone (FIZ)

A fracture network is a network consisting of several fractures. These fractures may or may not interact with each other. If a fracture does not interact with other fractures, it will then be modelled as a single fracture (as shown in Figure 3-1). If two or more fractures intersect, there will be a so-called fracture intersection zone (FIZ). Figure 3-3 shows an example of two interacting fractures where Fracture 1 is represented by the green elements and Fracture 2 consists of the cyan elements. The purple elements are the FIZ.

We now discuss how to represent the FIZ in our model. When two or more fractures intersect the water flow at the node of intersection (the FIZ) will be dominated by the fracture that has the largest aperture when other conditions are the same. A larger aperture implies a larger transmissivity. Therefore the largest transmissivity value of all the intersecting fractures will be taken for the FIZ elements.

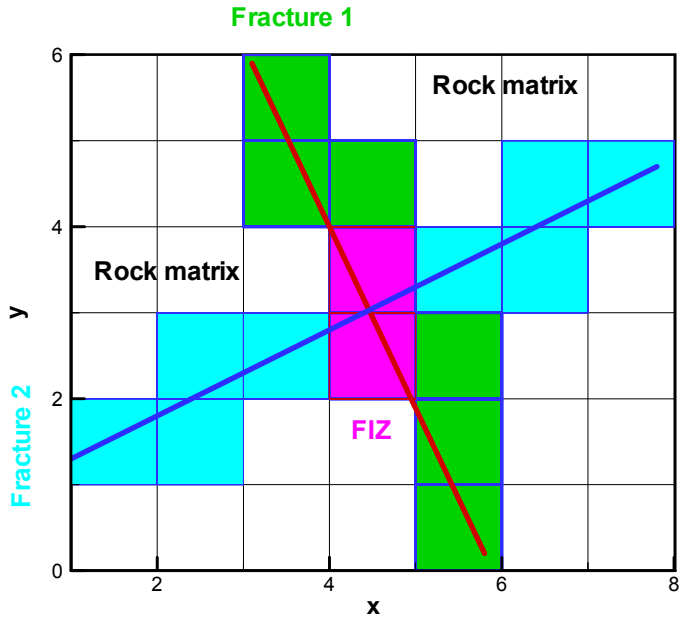

Figure 3-3. *Two interacting fractures in a 2-dimensional domain. The purple elements are the FIZ.*

A single fracture in a 3-dimensional domain

The methodology used in modelling a 3-dimensional domain is essentially the same as that used in the 2-dimensional plate. Assume that there is a single fracture in a 3-dimensional rock volume. The 3-dimensional rock volume (L×W×H) will be discretized into M×N×K cubic elements. A single fracture in the 3-dimensional block is presented by a series of staggered elements as shown in Figure 3-4. These staggered elements follow the tracks of the fracture plane. It should be noted again that, the same as in the case of the 2-dimensional modelling, the size of the elements is not related to the fracture aperture. Every fracture element should have a hydraulic conductivity value. Two distinct regions are also distinguished in the rock volume. In addition to the fracture elements, we have the elements of the rock matrix. The elements of the rock matrix are assumed as well to be not active in the flow simulations (no flow).

Since only the transmissivity values are available in the data delivery within the TRUE program, the conductivity of an element is obtained from the transmissivity value of the fracture divided by the size of the element in the vertical direction (z-direction), $K = T/\Delta l$ where Δl is the size of the cubic element, i.e., $\Delta l = \Delta x = \Delta y = \Delta z$. Velocities are calculated on the six faces of each cubic element (Figure 3-5).

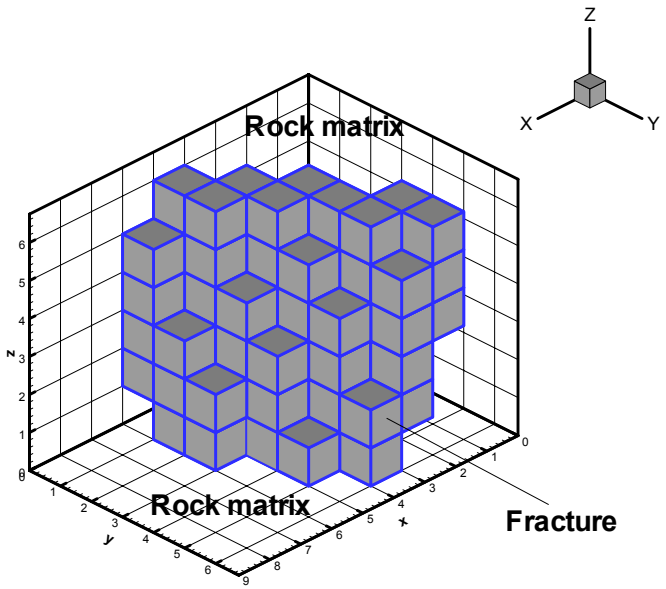

Figure 3-4. *A single fracture in a 3-dimensional domain.*

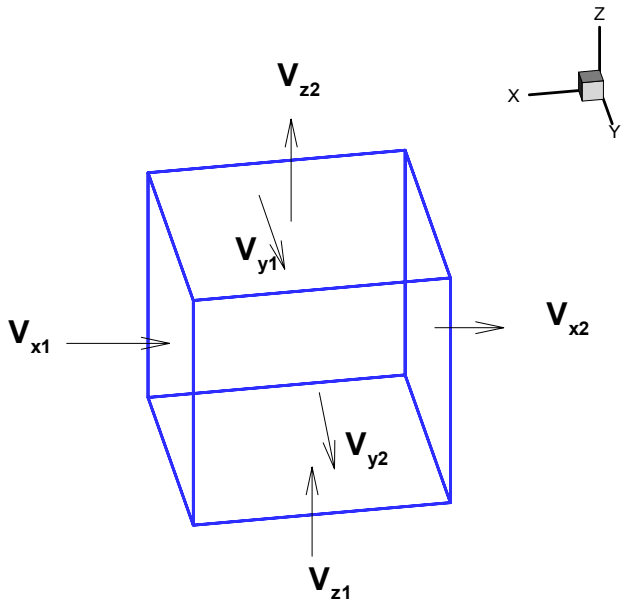

Figure 3-5. *Flow into and out of an element and the velocities on the six faces of the element.*

Two fractures interacting in the 3-dimensional domain

Two orthogonal interacting fractures are shown in Figure 3-6. In the Task 6D simulations, a constant *T* value is assigned to all elements in a given fracture. When two fractures intersect, we take the larger value of the transmissivities of the two fractures to represent the value of the FIZ, as what has been done for the 2-dimensional rock plate. If more fractures intersect, the largest transmissivity among the fractures is assigned to the FIZ elements.

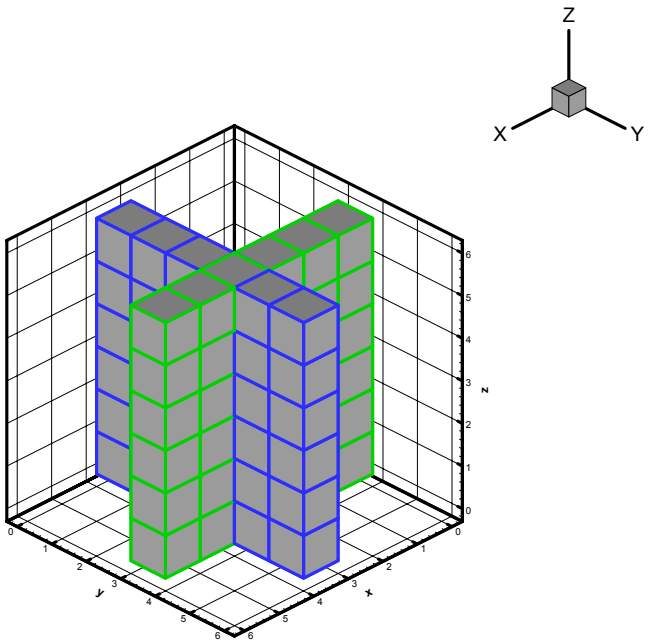

Figure 3-6. *Two fractures interacting in a 3-dimensional domain.*

Three-dimensional fracture network in Task 6C : Geometric description

The basic model for the fracture network is the Task 6C model (Dershowitz et al, 2003). All the structures are assumed to be planar. The rock block of 200 m contains 11 deterministic structures, 25 synthetic structures and more than 5000 background fractures.

The center of the 200 m block is located at the following position according to the Äspö coordinates:

Easting (x): 1900 m,

Northing (y): 7170 m,

Elevation (z): -450 m.a.s.l..

The 200 m block is aligned North-South in the Äspö coordinates, with ± 100 m in each direction.

The deterministic structures are the primary conductive structures in the TRUE Block Scale rock volume. A deterministic structure is specified by the coordinates of its four corners together with its transmissivity (for detailed information see Dershowitz et al., 2003). The deterministic structures are shown in Figure 3-7.

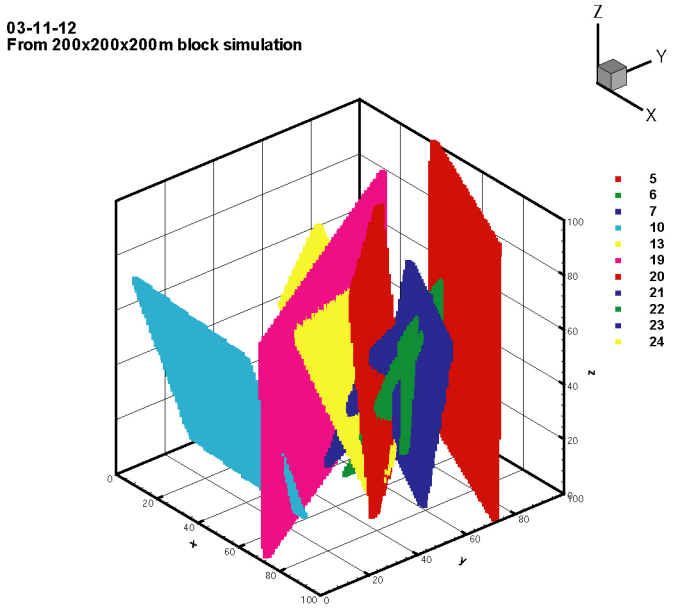

Figure 3-7. *Deterministic 100 m scale structures in the Task 6C model.*

The synthetic structures are the structures located at the periphery of the 200 m block and are fitted in the network of the deterministic structures. The synthetic structures are generated based upon the statistical analysis of the deterministic structures. Figure 3-8 shows both the deterministic (green) and the synthetic structures (cyan). The background fractures are typically less than 50 m in scale with relatively low conductivity (Figure 3-9), and fit in the network of the deterministic and synthetic structures. The background fractures have generally smaller transmissivities than those of the deterministic and synthetic structures.

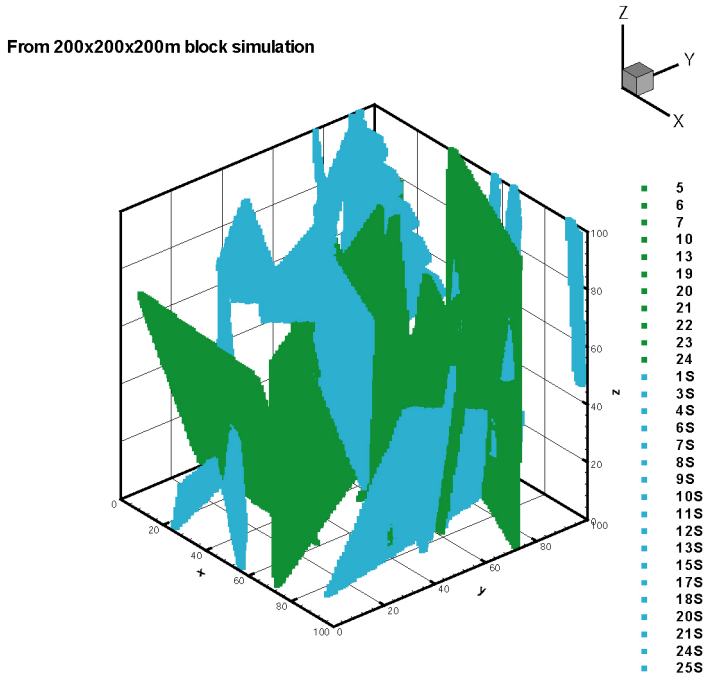

Figure 3-8. *Deterministic and synthetic structures in the Task 6C model.*

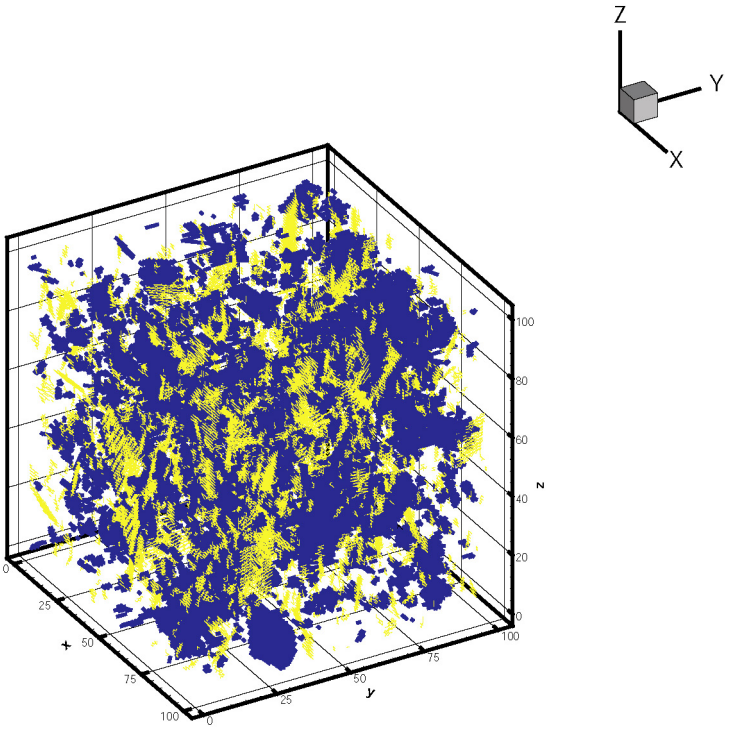

Figure 3-9. *Background fractures in the Task 6C model. The blue region represents fractures of the Shallow set. The yellow region is the NNW set of fractures.*

3.2.2 Pore space

Task 6C model

Two basic structure types have been defined in the Task 6C model: structure Type 1 which consists of five retention zones: fracture coating, fault gouge, cataclasite, altered zone and intact rock (Figure 3-10 from Dershowitz et al., 2003), and structure Type 2 which consists of the fracture coating, the altered rock and the intact rock (Figure 3-11 Dershowitz et al., 2003). A single structure may be a purely Type 1 structure, a purely Type 2 structure or a combination of them.

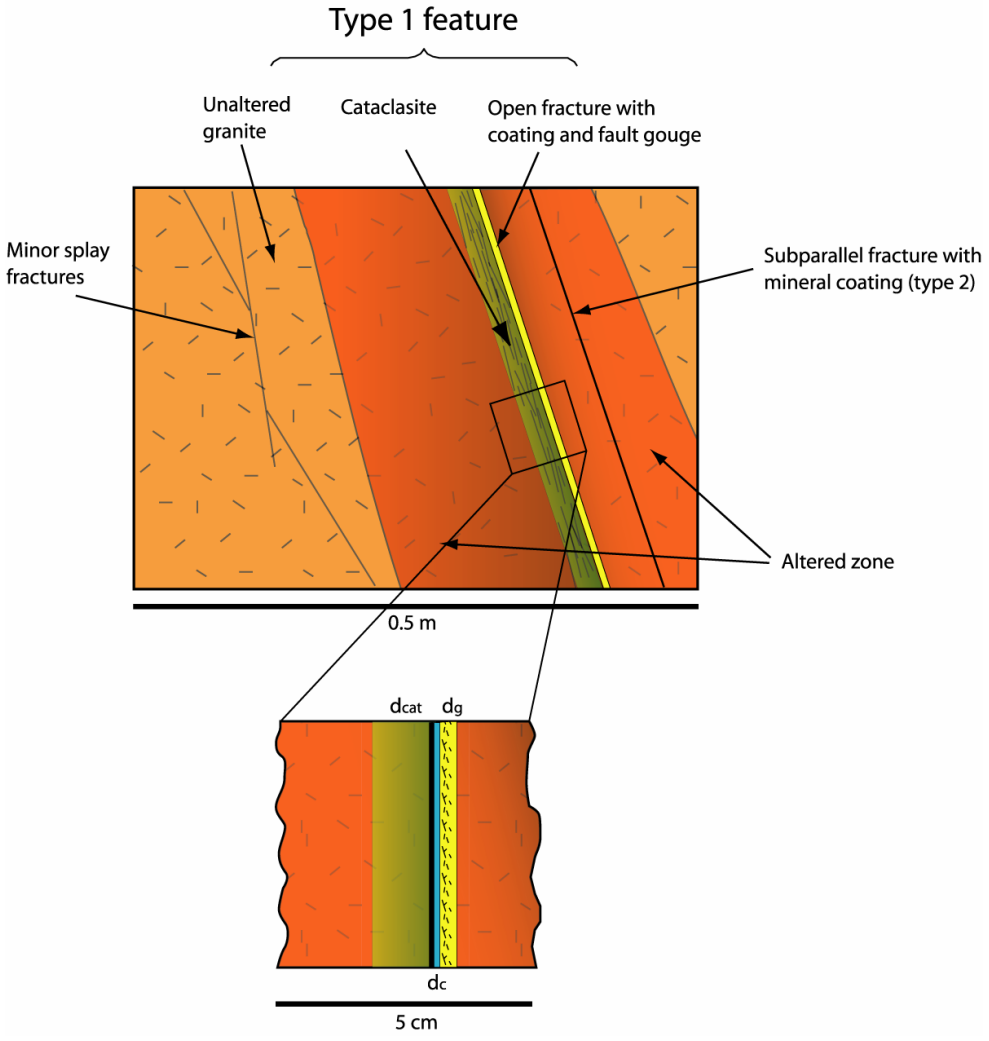

Figure 3-10. *Visualization of the geological structure Type 1 (fault) (reproduced from Dershowitz et al., 2003).*

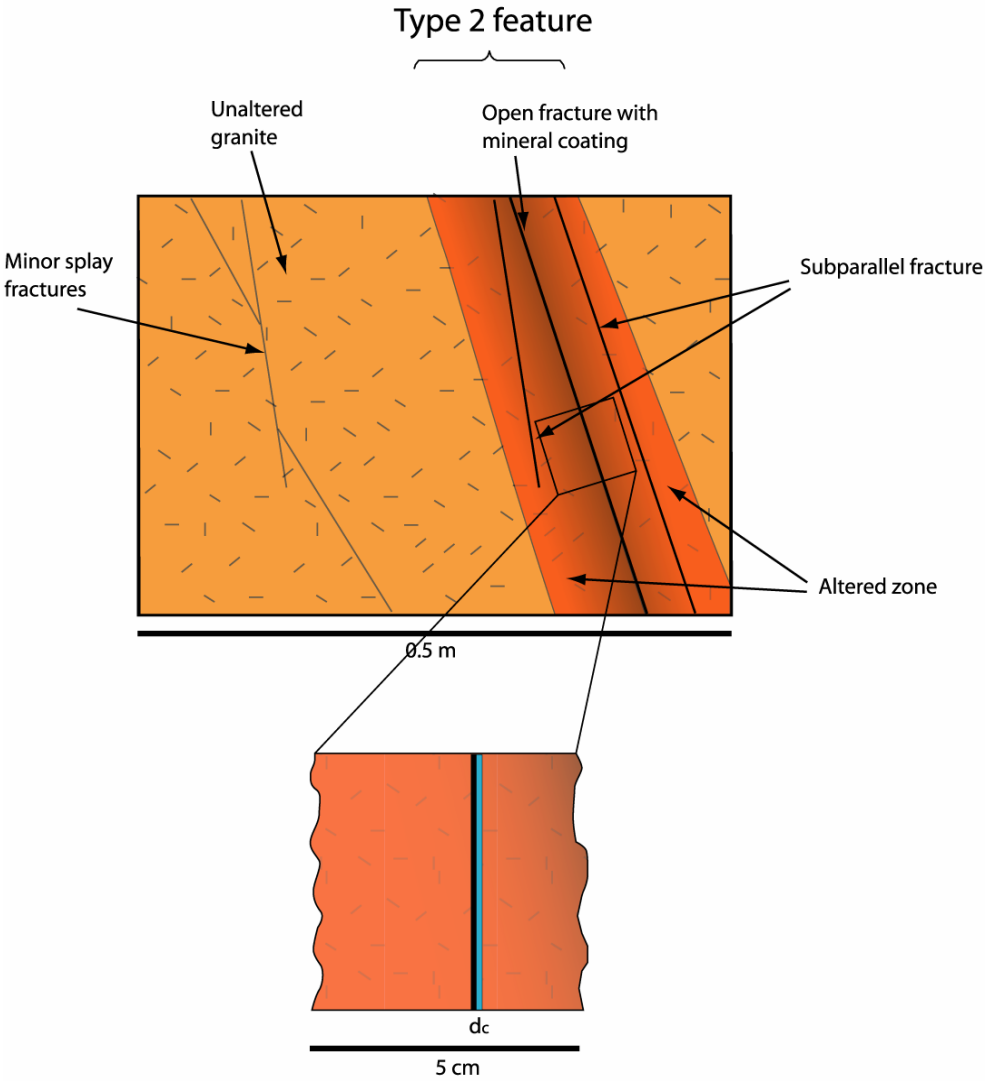

Figure 3-11. *Visualization of the geological structure Type 2 (non-fault) (reproduced from Dershowitz et al., 2003).*

The two types of the geological structures are quantified in terms of the thickness and porosity (as well as formation factor) of each geologically defined retention zone shown in Table 3-1 and Table 3-2 (Dershowitz et al., 2003).

Table 3-1. Properties of geological structure of Type 1.

Rock type	Extent (cm)	Porosity (%)	Formation factor (−)
Intact wall rock	−	0.3	7.3E-5
Altered zone	20	0.6	2.2E-4
Cataclasite d_{cat}	2	1	4.9E-4
Fault gouge d_g	0.5	20	5.6E-2
Fracture coating d_c	0.05	5	6.2E-3

Table 3-2. Properties of geological structure of Type 2.

Rock type	Extent (cm)	Porosity (%)	Formation factor (−)
Intact wall rock	−	0.3	7.2E-5
Altered zone	10	0.6	2.2E-4
Fracture coating d_c	0.05	5	6.2E-3

Task 6D, 6E and 6F

In the Task 6C model, the porosity θ and the distribution coefficient K_d did not vary longitudinally (in the x - y plane), but varied along the direction of the penetration depth of the tracers (in the z direction into rock matrix perpendicular to the fracture surface, see Table 3-1 and Table 3-2). In the present work, we also consider two fracture types following the Task 6C model: Type 1 includes features associated with faulting such as fault gouge, cataclasite and /or mineral coatings. Type 2 is not associated with faulting and consists of intact wall rock with some alteration.

In the Task 6C model, the sorption coefficient K_a for the fracture surface is calculated from the K_d values of the thin fracture coating zone. The fracture coating is therefore considered as the fracture surface in the present work. The fracture coating of 0.05cm thick is assumed to be evenly distributed on both sides of the open fracture, i.e., 0.025cm on each side. This assumption is applicable for both types of the fractures in our simulations for Task 6D, 6E and 6F.

For structure Type 2 there is a 10 cm altered zone behind the fracture coating. It is also assumed that the altered zone is evenly distributed on both sides of the rock matrix adjacent to the fracture coating, i.e., 5 cm on each side. Outside the altered zone is the intact rock matrix (Figure 3-12).

The simulations will be performed only on one side. For the reason of symmetry on the other side there will be the same results. Table 3-3 summarizes the porosity profile for structure Type 2 at different depths in the rock matrix for our model. The porosity is generally decreasing as the depth into the rock matrix increases.

Table 3-3. Porosity profile in depth for structure Type 2.

Rock type	Depth (mm)	Porosity (-)
Fracture coating	0 – 0.25	0.05
Altered zone	0.25 – 50.25	0.006
Unaltered	50.25 -	0.003

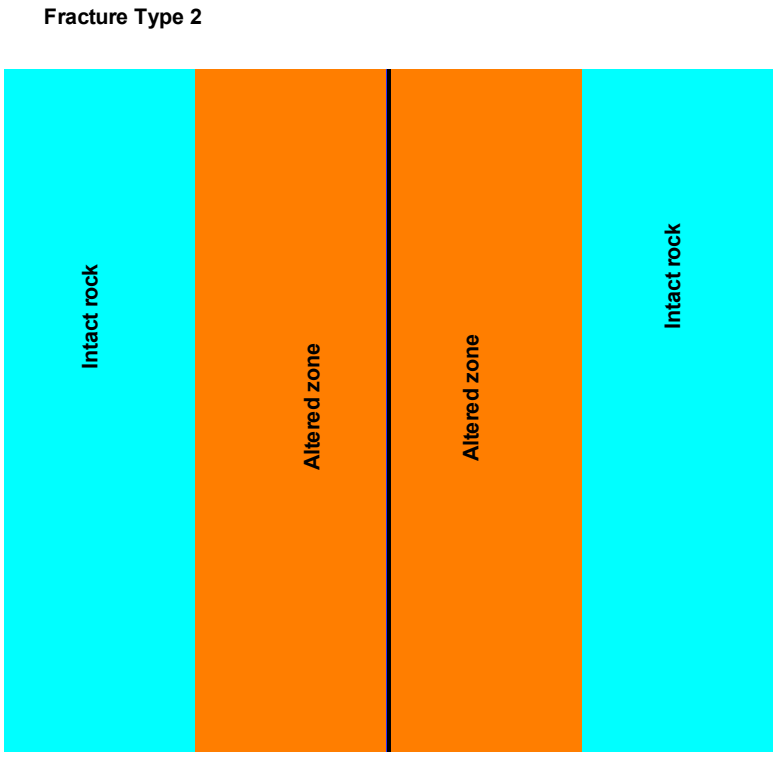

Figure 3-12. *Distribution of the retention zones in structure Type 2.*

For structure Type 1 the situation is more complicated. The thin fracture coating is still assumed to be evenly distributed on both sides of the fracture. Two other zones (the cataclasite and fault gouge zones) are behind the fracture coating. The structure shown in Figure 3-10 should be considered as to be somehow arbitrary since it is unlikely in reality that the cataclasite is always on one side of the rock matrix while the fault gouge in on other side. In reality it is more likely that at some points the cataclasite is on one side while at other points it is on the other side. The same is true for the fault gouge. They will be irregularly distributed on both sides of the fracture. In the lack of detailed information concerning their distribution we still assume that the cataclasite is distributed along 50% of the flow path and the fault gouge along the other 50%. However, in the present work they are not assumed to be monotonously distributed along respective sides of the fracture, but alternatively distributed on both sides as is shown in Figure 3-13. The altered zone (10 cm thick) is still evenly distributed on both sides of the rock matrix. The intact rock zone is behind the altered zone on both sides (not shown in Figure 3-13).

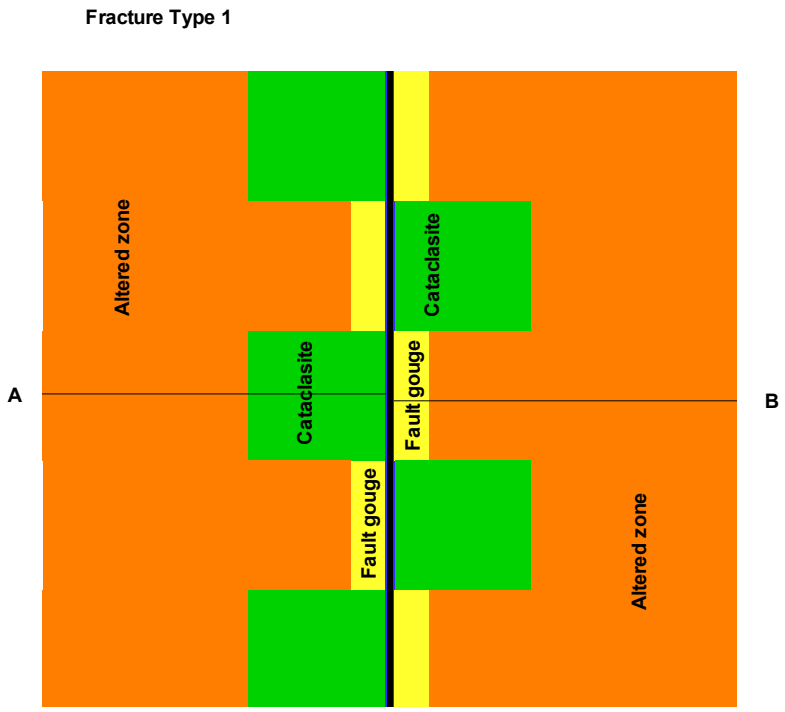

Figure 3-13. *Distribution of the retention zones in structure Type 1.*

As is shown in Figure 3-13, in the middle of structure Type 1 lies the open fracture with the fracture coatings. The fracture coating is treated as the fracture surface. The entire rock matrix of structure Type 1 can then be divided into two parts. Part A consists of the following retention zones: the cataclasite, the altered zone and the intact rock (Figure 3-13). Part B consists of the fault gouge, the altered zone and the intact rock (Figure 3-13). The sorption coefficient K_a for the fracture surface is what was suggested in Task 6C (Dershowitz et al., 2003). Based on the data in Table 3-1, the following porosity profile at different depths within the entire rock matrix is obtained as shown in Table 3-4 for Part A of the matrix and Table 3-5 for Part B of the matrix.

Table 3-4. Porosity depth profile in depth for Part A of the rock matrix of structure Type 1.

Rock type	Depth (mm)	Porosity
Fracture coatings	0 – 0.25	0.05
Cataclasite	0.25 – 20.25	0.01
Altered zone	20.25 – 120.25	0.006
Intact rock	120.25 -	0.003

Table 3-5. Porosity depth profile in depth for Part B of the rock matrix of structure Type 1.

Rock type	Depth (mm)	Porosity
Fracture coatings	0 – 0.25	0.05
Fault gouge	0.25 – 5.25	0.01
Altered zone	5.25 – 105.25	0.006
Intact rock	105.25 -	0.003

On the time scale for PA modelling, we need to determine an effective value for every retention parameter over the entire rock matrix.

The effective value of the retention parameters (θ and K_d) could be obtained by two approaches. The first one is by calibrating on the measured BTCs, if tracer tests have been performed. The second one is by using the micro-structural information (e.g., retention parameter heterogeneity into matrix in the direction orthogonal to fracture plane as in Table 3-3 to Table 3-5). The key issue for the second approach is the penetration depth for individual tracers. We shall employ both approaches in the modelling of Task 6D, and use the second approach for Task 6E and 6F.

3.3 Flow model

3.3.1 Processes considered

The LaSAR approach is applied in the Task 6D, 6E and 6F modelling with the following processes considered and the assumptions made for the flow:

- The flow is assumed to be in steady state,
- The tracers are transported by advection in the fracture,
- The flow in the pores of rock matrix is assumed to be negligible compared to the flow in the fractures,
- The tracers are fully mixed in the fracture in the z-direction (orthogonal to the fracture plane).

3.3.2 Mathematical description

The flow in the open fracture is governed by two partial differential equations: mass balance and Darcy's law

$$K\nabla^2 h = q \tag{3-2a}$$

$$v = -\frac{K}{\theta}\nabla h \tag{3-2b}$$

where h (L) is the hydraulic head; K(L/T) is the hydraulic conductivity. K is related to the transmissivity T by $T = K\Delta z$, where Δz is the element size in the z direction; q (1/T) is the source/sink term; v is the velocity; and θ is the so-called porosity defined by $\theta = e/\Delta z$, where e is the fracture aperture.

The density of the fluid is assumed to be constant. The boundary conditions are the specified heads at the boundaries. Eq. (3-2), together with the specified boundary conditions are the basic mathematical representation of the flow model. Eq. (3-2) is solved numerically.

3.3.3 Numerical implementation

Task 6D

Numerically the flow equations are solved in two steps. In the first step, the 200 m cubic block is discretized into 100×100×100 cubic elements with each element having a size of 2 m×2 m×2 m. The flow equations are solved in the first step to obtain the boundary head conditions for the following second step simulation. In the second step, a smaller inner domain within the 200 m block is defined (Figure 3-14). The transport takes place in the inner domain.

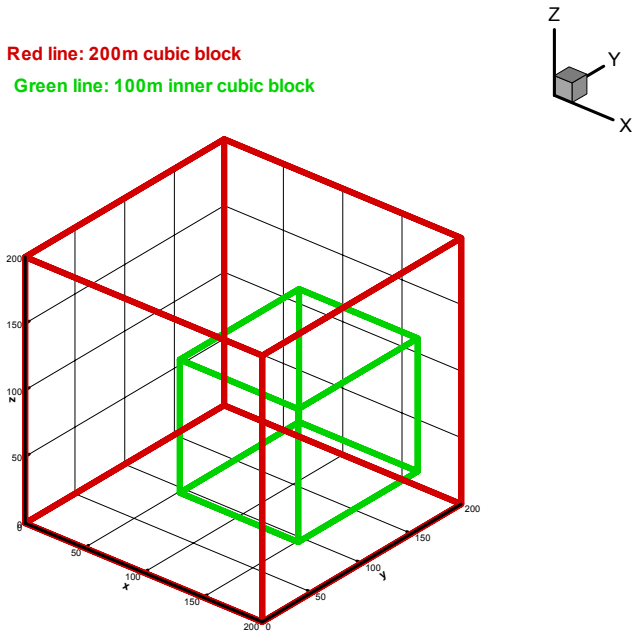

Figure 3-14. *Configuration of the inner domain in the second step flow simulation.*

Flow simulation in the 200 m block

All structures (deterministic, synthetic and background fractures) are accounted for in the flow simulation. Every structure is represented by staggered elements as shown in Figure 3-5. One constant transmissivity value obtained from the data delivery is assigned to each structure. All elements located in the specific fracture are assigned the same value of transmissivity as the structure. A fracture network (Figures 3-7 to 3-9) consisting of staggered elements is obtained after the assignment of transmissivity values for all structures. We should emphasise that for the elements where two or more structures intersect, i.e., in the fracture interaction zone (FIZ), the largest transmissivity value among the involved structures is taken to be the transmissivity values for the elements. The boundary condition is the specified head values from the data delivery. For those boundary elements with no head values given, head values obtained by interpolation will be assigned to them (Figure 3-15). All elements in the rock matrix are assumed to have no flow in them (inactive). The numerical simulation of the flow equation (3-2) is conducted by using the widely accepted and thoroughly tested finite difference code MODFLOW 2000 (Harbaugh et al., 2000). The head values for all elements are obtained in this step of simulation. It should be noted that the head values are calculated at the centers of the elements.

The velocity distribution is also simulated. For every element (except the boundary elements) the velocities through the six faces of the element are calculated by Eq. (3-2b) for use later in the particle tracking simulation.

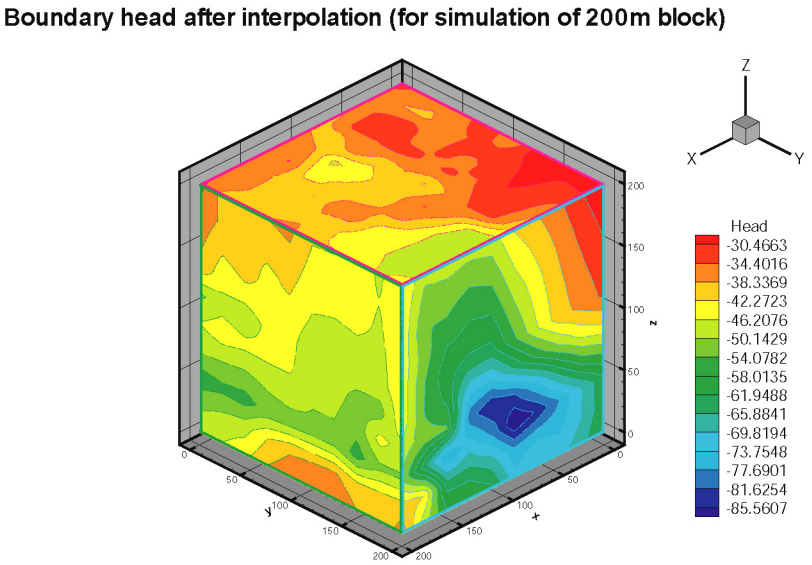

Figure 3-15. *Boundary conditions for the 200 m cubic block flow simulation.*

Flow simulation in the inner 100 m block

The inner 100 m cubic block within the 200 m block is located at x = 1880 – 1980, y = 7130 – 7230 and z = -524 – -424 (Figure 3-14). The inner domain is also discretized into 100×100×100 cubic elements while with each element having a size of 1 m × 1 m × 1 m. A fracture network is assumed to be located in the inner block by the same reasoning as for the 200 m block. It should be noted that now the elements have a smaller size. The boundary head values for the inner block are obtained from the first step simulation and interpolation. The flow equation (3-2a) is then solved by MODFLOW2000 to obtain the head distribution. The velocity field is subsequently solved by Eq. (3-2b). The velocity thus obtained will be used in the particle tracking simulation.

Task 6E

In Task 6D, the tracers were transported in an inner 100 m cubic domain. The flow simulations were then performed in two steps: first in the whole 200 m cubic block, then in the inner 100 m block. The transport took place only in the inner 100 m block. While for Task 6E, the tracers will be transported up to the west boundary of the 200 m cubic block. Numerically the flow simulations were performed in the 200 m cubic block directly (in one step). The 200 m block is discretized into 200×200×200 cubic elements with each element having a size of 1m × 1m × 1m. The flow equations are solved under the given boundary head conditions. The boundary conditions are the constant heads on the east and west boundaries, while no flow conditions are applied at the other boundaries. The heads are fixed at the east boundary as h=1m, and as h=0 m at the west boundary. The flow is then driven by a hydraulic gradient of 0.5% from east to west, while the corresponding hydraulic gradient in Task 6D is about 1000% over the Euclidean distance.

All structures (the deterministic, the synthetic and the background fractures) are accounted for in the flow simulation. The Task 6C DFN model is implemented in the same way as for Task 6D.

3.3.4 Parameters

The parameters controlling the flow are the transmissivities of the fractures and the boundary conditions. We use a constant transmissivity value obtained from the data delivery for a given fracture. The transmissivity values for different fractures vary in accordance with the data delivery.

3.4 Transport model

3.4.1 Processes considered

We consider the following mass transfer processes in our modelling:

- Dispersion of tracers in the fracture due to velocity variation (characterised by τ and β distribution);
- Unlimited diffusion (*D)* into the rock matrix and linear equilibrium sorption *(K_d)* inside the rock matrix *(κ)*.
- The fracture coating in the Task 6C model is considered to be on the fracture surface, and sorption on the fracture surface is assumed to be at equilibrium (K_a).

3.4.2 Mathematical description

The transport of the tracer can be described by two coupled, one-dimensional equations: one for the tracer concentration in the fracture (mobile), and one for the tracer concentration in the rock matrix (immobile) (e.g., Selroos and Cvetkovic, 1996):

$$\frac{\partial C}{\partial t} + \frac{\partial C}{\partial \tau} = S_f \tag{3-3}$$

$$\frac{\partial N}{\partial t} - D\frac{\partial^2 N}{\partial z^2} = S_m \tag{3-4}$$

where C is the tracer concentration in the fracture (M L^{-3}); N is the tracer concentration in the matrix (M L^{-3}); S_f is the source/sink terms for the concentration in the fracture [M L^{-3} T^{-1}]; and S_m is the source/sink terms for the concentration in the matrix [M L^{-3} T^{-1}]. The source term S_f consists of two parts, diffusion/sorption in the rock matrix and sorption on the fracture surface and is expressed as $S_f = \frac{D\theta}{b(\tau)}\frac{\partial N}{\partial z} - \frac{K_a}{b(\tau)}\frac{\partial C}{\partial t}$, and the source term S_m is expressed as $S_m = -K_d \frac{\partial N}{\partial t}$ where D [L^2 T^{-1}] is the diffusion coefficient in the rock matrix; θ [-] is the porosity; $b(\tau)$ [L] is the Lagrangian half-aperture; K_a [L] is the partition/distribution coefficient for sorption on the fracture surface; and K_d is the distribution coefficient in the matrix.

Eq. (3-3) and Eq. (3-4) could also be written as

$$\frac{\partial q}{\partial t}+\frac{\partial q}{\partial \tau}=\frac{D\theta}{b(\tau)}\frac{\partial N^*}{\partial z}-\frac{K_a}{b(\tau)}\frac{\partial q}{\partial t} \tag{3-5}$$

$$\frac{\partial N^*}{\partial t}-D\frac{\partial^2 N^*}{\partial z^2}=-K_d\frac{\partial N^*}{\partial t} \tag{3-6}$$

where $q = C\,V$ [M L^{-2} T^{-1}] is the tracer breakthrough in the fracture and $N^* = N\,V$ [M L^{-2} T^{-1}].

Solution for a single trajectory

A pulse injection is considered at the boundary $x = 0$:

$$q(0,t)=\rho_0\delta(t) \tag{3-7}$$

Initially the fracture and the matrix are free of the injected tracer, hence

$$q(x,0)=N^*(x,0)=0 \tag{3-8}$$

At the fracture surface ($z = b$), the concentration is continuous, i.e.,

$$q = N^* \text{ at } z=b \tag{3-9}$$

The solution for Eq. (3-5) and Eq. (3-6) can be obtained for a single trajectory using Laplace transform (e.g., Selroors and Cvetkovic, 1996),

$$q(x,t;\tau)=\rho_0\gamma(t,\tau;\beta) \tag{3-10}$$

and

$$\gamma(t,\tau;\beta)=\frac{H(t-\tau)B}{2\sqrt{\pi}(t-\tau-A)^{3/2}}\exp\left[-\frac{B^2}{(t-\tau-\beta A)}\right] \tag{3-11}$$

where

$$B=\sum_{j=1}^{M}\beta_j\kappa_j\,;\qquad \beta_j=\frac{l_j}{V_j b_j}\,;\qquad \tau_j=\frac{l_j}{V_j} \tag{3-12}$$

$$A=\sum_{j=1}^{M}K_a^j\beta_j\,;\qquad \kappa_j\equiv\theta_j\left[D_j(1+\frac{\rho_b K_d^j}{\theta_j})\right]^{1/2} \tag{3-13}$$

and γ [1/T] is the probability density function of the residence time for a single tracer particle travelling from the injection to the pumping boreholes coupled with the processes of advection, diffusion and sorption. γ is conditioned on the parameter A and B; and H is Heaviside step function.

The index "j" designates either the jth fracture (if the particle is transported through a series of fractures), and/or the jth discretization segment in a single heterogeneous fracture; M is the total number of segments, which could also extend through a series of heterogeneous fractures; and ρ_b is the density of the rock matrix. All of the parameters are in general segment-dependent, they all therefore have the index "j".

Note that Eqs. (3-11) to (3-13) are applicable to a single trajectory (e.g., the *i*th trajectory). We have a number of trajectories (*N* trajectories in this simulation).

In Eq. (3-11) two grouped quantities *B* and *A* govern the value of γ. The grouped quantity *B* is further determined by β and κ if the retention parameters are uniform (θ and K_d in the present work, Cvetkovic, 1999). Here β is purely a flow dependent quantity. Since $\kappa = \theta\sqrt{D(1+\frac{\rho K_d}{\theta})}$ by definition and is a parameter describing the diffusion and sorption in the rock matrix, the effect of aperture variation on matrix diffusion/sorption is accounted for by the product $\beta\kappa$. On the other hand, the effect of aperture variation on surface sorption is described by the parameter *A* that is determined by the product βK_a in Eq. (3-11).

Dispersive effects

Dispersion in a fracture network arises when there is a random variation of the advection velocity. The solute particles in the fluid are advected along different streamlines due to the random variation of the fluid velocity. When the particles move randomly in the fracture network, τ and β become random variables. The solution γ in Eq. (3-11) applicable to a single trajectory will depend on (or is conditioned to) the random values of τ and β.

Let $g(\tau, \beta)$ denotes the joint probability density function (PDF) of τ and β at a pumping section or a control plane (CP). This PDF can in principle be computed using particle tracking (Monte Carlo) simulations (e.g., Cvetkovic et al., 1999). If $g(\tau, \beta)$ is known, and γ is available in a closed form, the solute discharge, *Q*, (or the breakthrough curve, BTC), at the pumping section (or CP) can be evaluated as:

$$Q(t) = \int_0^t \phi(t-t')dt' \int_0^\infty d\beta \int_0^\infty \gamma(t', \tau; \beta) g(\tau, \beta) d\tau \tag{3-14}$$

where $\phi(t)$ is the injection function. There is, however, a strong correlation between τ and β as shown by numerical simulations in a generic configuration (e.g., Cvetkovic et al., 1999, Cheng, et al., 2003; Cvetkovic et al., 2004; Cheng, 2005). We can, therefore, assume a deterministic relation between τ and β, and ascribe the variation of β to PDF of the residence time for pure advection, $g(\tau)$. The remaining problem is then to determine $g(\tau)$. If $g(\tau)$ is known, the solute discharge *Q* is evaluated as:

$$Q(t) = \int_0^t \phi(t-t')dt' \int_0^\infty \gamma[t', \tau; \beta(\tau)] g(\tau) d\tau \tag{3-15}$$

where $\beta(\tau)$ is a deterministic functional relation between τ and β. For the present work, a linear β and τ relation is assumed and obtained by fitting the simulated β and τ values.

3.4.3 Numerical implementation

Task 6D

The solution for the BTCs by Eq. (3-11) cannot be solved analytically with close form solution. It is instead integrated numerically once the retention parameters are obtained. The parameters include the slope k in the linear β and τ relationship $\beta=k\tau$ and diffusion/sorption parameters (κ). In this section we mainly discuss the particle tracking simulation to obtain β and τ distribution and their linear relationship.

Particle tracking in the 200 m block

The particles are injected from the injection borehole section (structure #23) and then tracked using a particle tracking technique where the transit time of the particle in each element is calculated after the entrance and exit points on the element surfaces have been established (Mose et al., 1994). β and τ are calculated following each particle at the pumping borehole section (structure #21). The Euclidean distance between the injection section and the pumping section is 17.6 m. The actual length of a trajectory is usually longer.

If N particles are to be released from the element of the injection section, N particles are placed evenly over the element. Each particle i (i = 1,2,…,N) will be advected along its (the ith) trajectory. The values of τ and β for the ith particle at the element of the pumping section are computed by:

$$\tau_i(L) = \sum_{j=1}^{M} \frac{l_{ij}}{V_{ij}} \tag{3-16}$$

$$\beta_i(L) = \sum_{j=1}^{M} \frac{l_{ij}}{V_{ij} b_{ij}} \tag{3-17}$$

where l_{ij} is the length of jth segment along the ith trajectory; V_{ij} is the velocity of the jth segment along the ith trajectory; b_{ij} is the half-aperture of the segment. We shall discuss more of the discretization segments in a later section.

Based on the computed travel time of each particle, the ensemble means $\langle\tau\rangle$ and $\langle\beta\rangle$ are calculated as:

$$\langle\tau\rangle = \frac{1}{N}\sum_{i=1}^{N}\tau_i \tag{3-18}$$

$$\langle\beta\rangle = \frac{1}{N}\sum_{i=1}^{N}\beta_i \tag{3-19}$$

Particle tracking in 100 m block

A similar particle tracking simulation as for the 200 m block is performed for the inner 100 m block. The τ and β values are computed at the pumping section for all injected particles. The ensemble mean and the variance of τ over all particles are also computed for defining $g(\tau)$ in the calculation of breakthrough curves (BTCs).

Task 6E

The aim of particle tracking simulation is to obtain particle trajectories and the corresponding β and τ distribution. The particles are released from the source section located at structure #23, the same location as the injection point in Task 6D. The source section is located near the center of the 200 m block. The structure #23 has a size and transmissivity similar to that of Feature A in TRUE-1 (Winberg et al., 2000). The source section is assumed to be an intersecting fracture with a linear extension of 3 m. The source section is modelled as several point sources on a line. The actual location of the source section is presented in Table 3-6.

Table 3-6. Data for source section used in Task 6E. Coordinates are given in the ÄSPÖ96 system.

Parameter	Source section		
	Endpoint 1	Center	Endpoint 2
Easting	1930.758	1929.741	1928.724
Northing	7193.742	7194.840	7195.938
Elevation	-476.100	-476.100	-476.100

We inject 1498 particles from the source section, and the particles are placed evenly over the 3m long source section. The particles are tracked. β and τ are calculated following each particle (along each trajectory) at the following three control planes (CPs):

- At the intersection with a vertical plane defined by Easting = 1920 m, i.e. at a Cartesian distance about 10 m from the release point.
- At the intersection with a vertical plane defined by elevation = 1880 m, i.e. at a Cartesian distance about 50 m from the release point.
- At the western boundary of the 200 m block

3.4.4 β and τ relationship

Task 6D

Two key parameters τ and β are solely determined by the hydraulic condition (transmissivity distribution and boundary condition) in the flow simulation. The parameter β is the key parameter that relates the flow with the retention. (e.g., Cvetkovic et al., 1999; 2000).

The scattergram of β and τ obtained from the inner 100 m block simulation is shown in Figure 3-16.

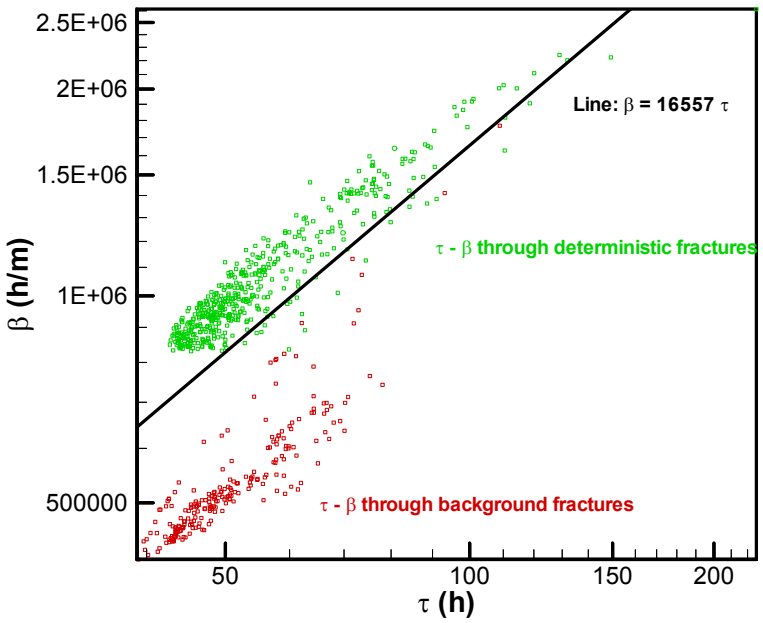

Figure 3-16. *Scattergram of the simulated τ and β data in the inner 100 m block including all structures for Task 6D.*

In the simulations both the deterministic and the background fractures have been accounted for. Computation of β and τ is based on the particle tracking with $N = 729$ injected particles. The τ - β values are recorded at the pumping section.

The particles have two groups of trajectories (Figure 3-16). The first group of trajectories go through the deterministic structures, while the second go through the background fractures. There are consequently two separate groups of points in the τ - β scattergram. In Figure 3-16 the green symbols are the simulated τ - β values for the particles travelling in the deterministic fractures and the red symbols are the simulated τ - β values for the particles travelling the background fractures. It can be seen clearly that the τ - β values for particles travelling through the background fractures tend to be lower than those for particles travelling through the deterministic structures. On the other hand it is also obvious that for both groups of the τ - β values, an approximately linear relationship between τ and β exists. A linear regression is made for all τ - β values and a linear relationship of $\beta = 16557\,\tau$ is obtained (the black line). The mean travel time is 56 h. The variance of the travel time is 233 h^2. This gives a coefficient of variation to be 0.3. These values are consistent with the temporal moments evaluated for the TRUE Block Scale experiments (Cvetkovic and Cheng, 2002).

Table 3-7 shows the temporal moments including the moments for the particle trajectories through the deterministic structures, through the background structures and through all of the structures. The trajectories through the background structures have a shorter mean residence time and a smaller variance which is in consistent with what is shown by the scattergram in Figure 3-16.

Table 3-7. Moments of water residence time for Task 6D.

Structure	Deterministic	Background	All
$<\tau>$ (h)	57.5	51.4	55.6
σ_τ^2 (h^2)	291.8	78.1	232.6
Number of trajectories	500	229	729

Task 6E

In the simulations both the deterministic and the background fractures have been accounted for. Computation of β and τ is based on the particle tracking with $N = 1498$ injected particles. The τ - β values are recorded at the three CPs.

At x = 1920 m

This CP has the shortest distance from the source section among the three CPs. The scattergram of the simulated τ and β results is presented in Figure 3-17. An approximately linear relation between τ and β exists. A linear regression is made for all τ - β values and a linear relation of $\beta = 12380\tau$ is obtained (the black line). The mean travel time is 1.44 y. The standard deviation of the travel time is 0.42 y. This gives a coefficient of variation to be 0.3.

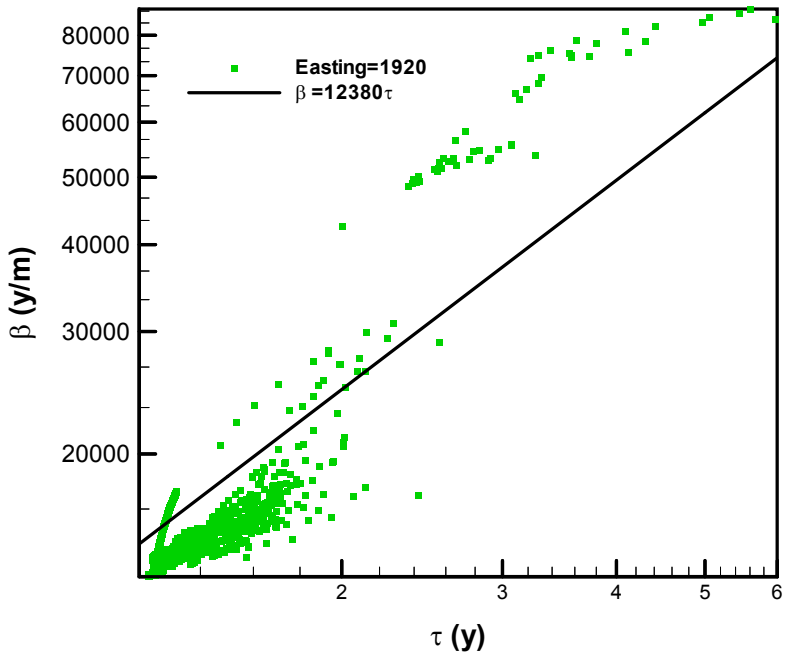

Figure 3-17. *Scattergram of simulated τ and β at x = 1920 m.*

At x = 1880 m

This CP has a Cartesian distance about 50 meters from the release point. Figure 3-18 presents the scattergram of the simulated τ and β at x = 1880 m. An approximately linear relation between τ and β also exists. A linear relation of $\beta = 9897\tau$ is obtained (the black line). The mean travel time is 3.65 y. The standard deviation of the travel time is 0.79 y. This gives a coefficient of variation to be 0.2.

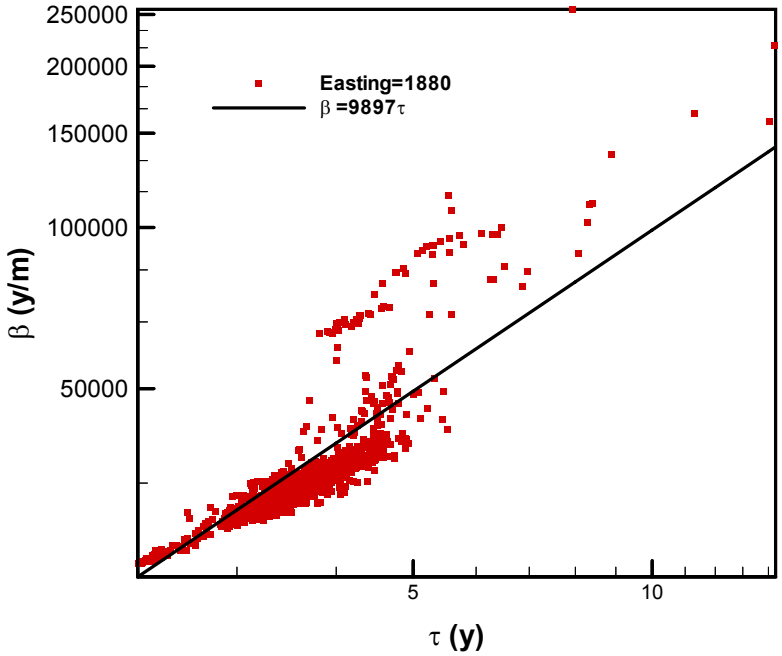

Figure 3-18. *Scattergram of simulated τ and β at x = 1880 m.*

At the western boundary (x = 1800 m)

This CP has the longest distance from the release point. Figure 3-19 presents the scattergram of the simulated τ and β at the western boundary. An approximately linear relation between τ and β still exists. A linear relation of $\beta = 9420\tau$ is obtained (the black line). The mean travel time is 6 y. The standard deviation of the travel time is 4.33 y. This gives a coefficient of variation to be 0.7.

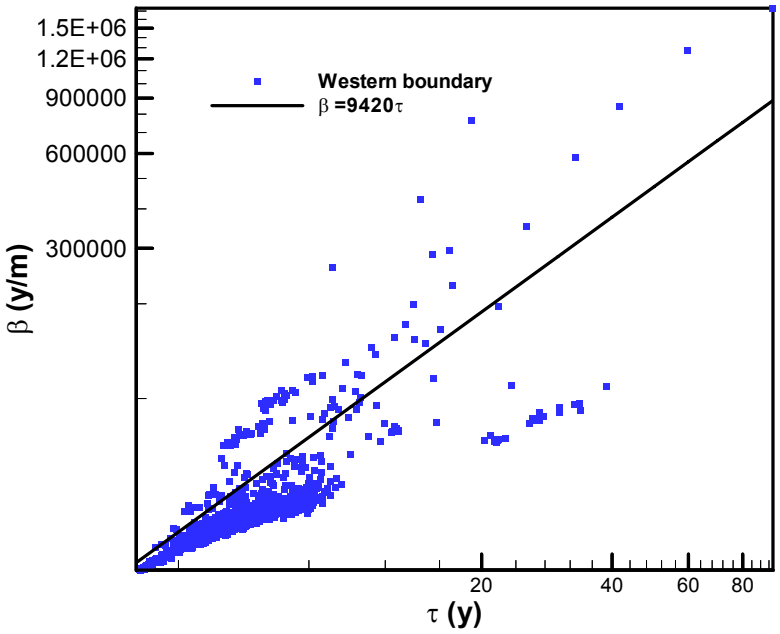

Figure 3-19. *Scattergram of simulated τ and β at western boundary.*

Summary of the simulated τ - β results

The simulation results of τ and β and their relations for three CPs are compared in Figure 3-20. The moments of τ and β are summarized in Table 3-8.

Table 3-8. Summary of simulated τ and β moments for Task 6E.

CP	<τ> (year)	σ_τ (year)	<β> (y/m)	σ_β (y/m)	k (m^{-1})
X=1920 m	1.44	0.4168	16766	9397	12380
X=1880 m	3.65	0.788	35282	14008	9897
X=1800 m	6.01	4.33	48876	66778	9420

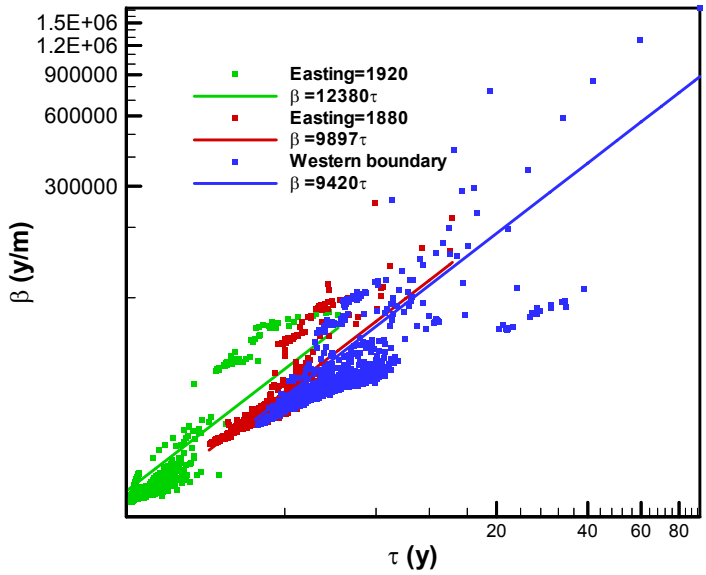

Figure 3-20. *Comparison of τ and β scattergrams at three CPs.*

3.4.5 Parameters

To calculate the BTCs the following parameters are needed: the distribution of water residence time τ and its moments, the parameter group κ and the parameter K_a.

The distribution of the water residence time is assumed to be inverse-Gaussian.

For Task 6D, the mean and the variance of τ is obtained from the simulated τ - β values using 729 injected particles, i.e., 56 h and 233 h^2. The τ and β are assumed to be linearly correlated with $\beta = k\tau$. The slope k is 16557 (m^{-1})

For Task 6E, the mean and the variance of τ are obtained from the simulated τ - β values using 1498 injected particles as shown in Table 3-8. The τ and β are assumed to be linearly correlated with $\beta = k\tau$. The values of the slope k are given in Table 3-8.

In order to obtain the effective parameters (K_a and κ) for the entire matrix, a brief summary of the properties of the two geological structure types will be presented.

Porosity and formation factor

Table 3-9 presents the porosity and the formation factor data for the different rock materials (from Dershowitz et al., 2003). The porosity should be considered as the maximum values. The formation factors are calculated by Archie's law, $F = 0.71 \cdot \theta^{1.58}$.

Diffusivity

Given the formation factor F, the effective diffusivity is calculated by $D_e = D_w \cdot F$ where D_w is the diffusivity of the tracer in bulk water. The calculated D_e values for different tracers in contact with different rock materials are summarized in Table 3-9.

Table 3-9. Effective diffusivities for individual tracers in contact with different rock materials. The diffusivities have been calculated using the formation factor, *F*, and the tabulated water diffusivities, D_w.

Tracer		Fracture Coating	Fault gouge	Cataclasite	Altered Zone	Unaltered wall rock
	Porosity (%)	5	20	1	0.6	0.3
	Formation factor, F	6.2E-03	5.6E-02	4.9E-04	2.2E-04	7.3E-05
	D_w (m^2/s)	D_e (m^2/s)	D_e (m^2/s)	D_e (m^2/s)	D_e (m^2/s)	D_e (m^2/s)
I-129	2.00E-09	1.2E-11	1.1E-10	9.8E-13	4.4E-13	1.5E-13
Ca-47	7.93E-10	5.0E-12	4.4E-11	3.9E-13	1.7E-13	5.8E-14
Cs-137	2.07E-09	1.3E-11	1.2E-10	1.0E-12	4.5E-13	1.5E-13
Ra-226	8.89E-10	5.6E-12	5.0E-11	4.4E-13	1.9E-13	6.5E-14
Am-241	5.95E-10	3.7E-12	3.3E-11	2.9E-13	1.3E-13	4.4E-14
Tc-99	5.00E-10	3.1E-12	2.8E-11	2.5E-13	1.1E-13	3.7E-14

The sorption coefficient in matrix K_d

The sorption coefficient in matrix (K_d) is obtained from Dershowitz et al. (2003). For tracers that sorb through cation-exchange, the values of K_d for different rock materials are calculated using the available data for cation-exchange capacities (CEC) for the individual minerals based on mineralogical analysis, the selectivity coefficients and the available/inferred information on groundwater chemistry. For detailed information the reader is referred to Dershowitz et al. (2003). The calculated results of the K_d values are presented in Table 3-10.

For the other radionuclides that will be used in the PA calculations of the Task 6 project (i.e., I^-, Ra^{2+}, Tc(IV) and Am(III)), no data are available regarding their specific sorption properties on the rock types at Äspö within the TRUE project. Their K_d-values have therefore been estimated according to the following procedures:

- is considered as a conservative tracer and its K_d value is set to be 0.
- Sorption characteristics of Ra^{2+} in saline groundwater have been addressed by Kulmala and Hakanen (1995). They investigated and compared the sorption of Sr^{2+}, Ba^{2+} and Ra^{2+} on Finnish rocks. In the TRUE Block Scale experiments the K_d-value for Ra^{2+} is obtained by multiplying the corresponding value of Ba^{2+} with a factor of 10.
- For Tc(IV) and Am(III) hydrolysis combined with surface complexation is considered to be the major sorption mechanism. The influence of different mineral types and different water compositions are considered to be minor. Therefore, the K_d-values based on the recommendations by Selroos and Elert (2001) are used for all combinations of rock materials and water compositions, i.e., $K_d = 0.2$ m^3 kg^{-1} for Tc(IV) and $K_d = 0.5$ m^3 kg^{-1} for Am(III).

Table 3-10. Summary of K_d values for different rock materials in contact with the TRUE Block Scale groundwater.

Tracer	Fracture coating	Gouge	Cataclasite	Altered zone	Intact rock
	θ =0.05 K_d (m^3/kg)	θ =0.2 K_d (m^3/kg)	θ =0.01 K_d (m^3/kg)	θ =0.006 K_d (m^3/kg)	θ =0.003 K_d (m^3/kg)
I-129	0	0	0	0	0
Ca-47	2.3E-4	7.1E-4	6.7E-5	8.8E-5	4.4E-5
Ra-226	4.6E-2	1.4E-1	1.2E-2	1.8E-2	8.8E-3
Cs-137	5.2E-2	1.6E-1	1.5E-2	2.0E-2	1.0E-2
Tc-99	0.2	0.2	0.2	0.2	0.2
Am-241	0.5	0.5	0.5	0.5	0.5

The density is assumed to be $\rho = 2700 kg/m^3$ for all zones.

Surface sorption coefficient K_a

In the following we will discuss the parameters K_a and κ. K_a is the sorption coefficient on fracture surface. The value of K_a will be obtained from the K_d values specified for the fracture coatings (Dershowitz et al., 2003) since the fracture coating is assumed to be in direct contact with the groundwater and it has a total thickness pf 0.5 mm which is distributed on both sides of the fractures. As has been shown in Dershowitz et al. (2003),

$$K_a = (K_d \rho + \theta) d \qquad (3\text{-}20)$$

where d is the thickness of the fracture coating (5×10^{-4} m), θ is the porosity of the fracture coating (0.05) and ρ is the density of the fracture coating (~2600 kg m^{-3}).

The calculated K_a values are presented in Table 3-11.

Table 3-11. Summary of surface sorption coefficient K_a.

Tracer	I-129	Ca-47	Cs-137	Ra-226	Tc-99	Am-241
K_d (m^3/kg) *	0	2.3e-4	5.2e-2	4.6e-2	0.2	0.5
K_a (m)	0	3.2e-4	6.8e-2	6.0e-2	0.26	0.65

*Values for the fracture coating material in contact with the TRUE Block Scale groundwater.

The κ parameter

κ is a parameter that describes the diffusion and sorption in the rock matrix. The influence of the variation of the fracture aperture on matrix diffusion/sorption is described by the product $\beta\kappa$. Once the parameters θ, D, K_d and ρ are known, the parameter κ can be readily calculated.

In Task 6D, complexity factors are not accounted for. In Task 6E we account for the complexity factors in Task 6E. This will be discussed later in this report.

4 Task 6D

4.1 Modelling strategy

The flow model used here is a 3-Dimensional model, and the flow equations are solved using the finite difference code MODFLOW 2000 (Harbaugh et al., 2000). The deterministic and the synthetic structures, as well as the background structures are all accounted for in the model. It is assumed that there is no water flow in the rock matrix.

The modelling started with a preliminary simulation on a 200 m × 200 m × 200 m block with 1 million cells (2 m × 2 m × 2 m for each cell) to obtain boundary conditions for second step simulation. Then the model focuses on an inner 100 m × 100 m × 100 m block of rock where the transport takes place. The flow and particle tracking simulations in the inner domain were carried out with a discretization of 1 m × 1 m × 1 m.

The particles (totally 729 of them) are injected from the injection section (structure #23). Their trajectories are tracked to obtain τ and β values for all particles at the pumping section (structure #21).

The τ - β relation (linear) is then established by linear fitting of the simulated values to obtain the slope k in $\beta = k\tau$ and to obtain the temporal moments of τ. The distribution of τ is assumed to be inverse-Gaussian.

4.2 Model calibration

We calibrate on the measured BTC data (C2 test) to obtain the effective retention parameters (κ and K_a). In the calibration an effective value of θ and an effective value of K_d are assumed for each tracer. However we account for the in-depth heterogeneity in the sensitivity study (see section 4.4.3). The calibration procedure for determining θ and K_d are described below.

The value of θ was obtained from fitting the BTC data for I-129 in the C-2 test. The travel time moments and the slope k were obtained as discussed in the previous chapter. The values are: κ = 1.8E-6 m $h^{-1/2}$, therefore θ = 2.4% since K_d = 0.

By using θ = 2.4%, the K_d for Ca-47 was obtained by fitting the BTC data of Ca-47 in the C-2 test. The values were: κ = 3.0E-5 m $h^{-1/2}$, θ = 2.4%, K_d = 5.1E-5 m^3 kg^{-1}.

By using θ = 2.4% the K_d for Cs-137 was obtained by fitting the BTC data of Cs-137 in the C-2 test. Although the data for Cs-137 were few, meaningful fittings could still be achieved. The values were: κ = 7.0E-4 m $h^{-1/2}$, θ = 2.4%, K_d = 1.2E-2 m^3 kg^{-1}.

The K_d value for Ra was obtained in the following way. By comparing the K_d value of Ra-226 with that of Cs-137 for all retention zones it could be concluded that the K_d value of Ra-226 was about 90% of the K_d value of Cs-226. From K_d = 1.2E-2 m^3 kg^{-1} for Cs-137, we obtained K_d = 1.1E-2 m^3 kg^{-1} for Ra-226.

The values of $K_d = 0.2$ m^3 kg^{-1} for Tc-99 and $K_d = 0.5$ m^3 kg^{-1} for Am-241 were used according to the Task 6D specification.

Table 4-1 summaries the calculated parameters from the calibration procedure on the measured BTC data.

Table 4-1. Parameters used for calculating the BTCs from the calibration procedure.

Tracer	θ (-)	F (-)	D_w (m^2/h)	K_d(m^3/kg)	κ (m h$^{-1/2}$)	K_a (m)
I-129	0.024	2.0E-3	7.20E-6	0	1.8E-5	0
Ca-47	0.024	2.0E-3	2.85E-6	5.1E-5	3.0E-5	3.2E-4
Cs-137	0.024	2.0E-3	7.45E-6	1.2E-2	6.9E-4	6.8E-2
Ra-226	0.024	2.0E-3	3.20E-6	1.1E-2	4.3E-4	6.0E-2
Tc-99	0.024	2.0E-3	1.8E-6	0.2	1.4E-3	0.26
Am-241	0.024	2.0E-3	2.14E-6	0.5	2.4E-3	0.65

4.3 Results

4.3.1 Flow

Description of flow paths

We inject 729 particles from the injection section. The particle trajectories follow two main flow paths (Figure 4-1). The first path ran through a network of four deterministic structures, i.e., structures 23D → 22D → 20D → 21D (the green lines). There are 500 particle trajectories or 69% of the total trajectories within this path according to the simulations. The second path consists of mainly background structures (the red lines). There were 229 particle trajectories or 31% of them in this path.

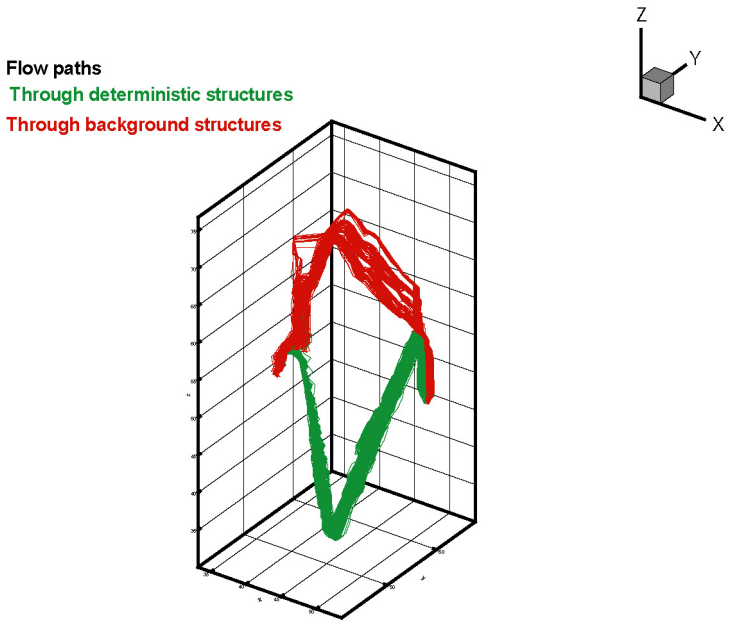

Figure 4-1. *Visualization of two flow paths for Task 6D.*

Drawdown in injection and pumping borehole

Table 4-2 shows the simulated head values at the injection and pumping sections from the simulation results.

Table 4-2. Drawdown at injection and pumping borehole for Task 6D.

Borehole	Drawdown (m)
Injection	-71.7
Pumping	-476.5

Water residence time distribution

The PDF of the water residence time from the simulated data of τ at the pumping section is presented in Figure 4-2. The red line is the inverse-Gaussian distribution fitting with the mean and variance from the corresponding simulation values. The simulated PDF has approximately a shape of inverse-Gaussian, although the peak is higher than the fitted inverse-Gaussian distribution. From the scattergram shown in Figure 3-16 it is clear that the trajectories are divided into two groups. The distributions of the two groups have not been presented separately here. Table 4-3 shows the ensemble mean and the variance of τ obtained from the particle tracking simulations of 729 trajectories.

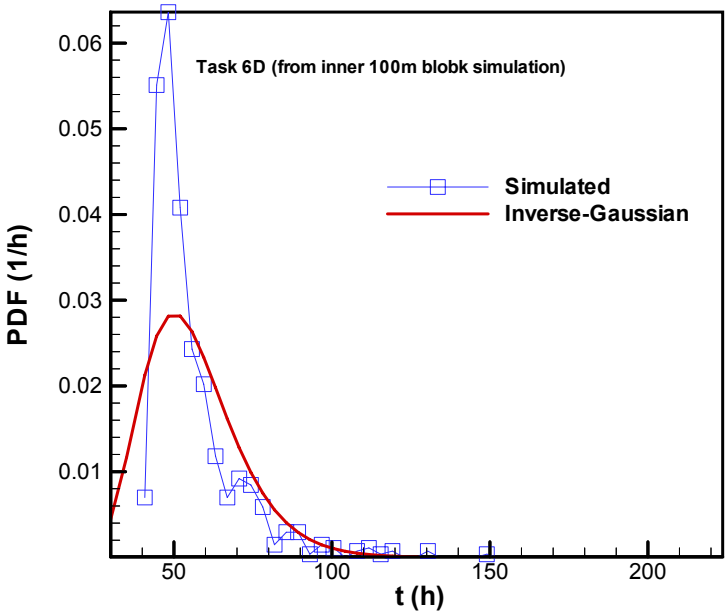

Figure 4-2. *Water residence time distribution for Task 6D. The red line is the inverse-Gaussian distribution fitting with the moments from the corresponding simulation values.*

Table 4-3. Moments of water residence time for Task 6D.

$<\tau>$ (h)	σ_τ (h)
55.6	15.3

4.3.2 Transport

β-parameter

The cumulative distribution function (CDF) of the β parameter is presented in Figure 4-3. The distribution of β does not have a definite trend. This distribution is not used directly in the calculation of the BTCs. We have assumed that β has a linear relationship with τ. Table 4-4 shows the mean and variance of the parameter β.

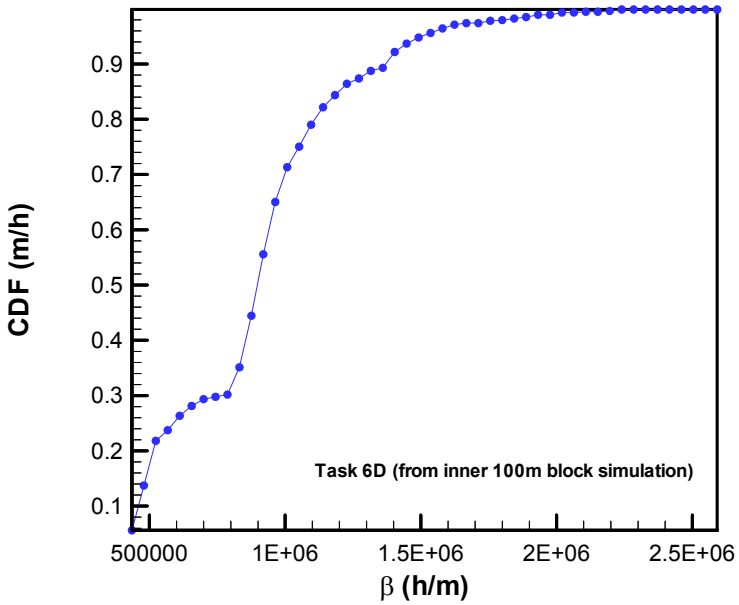

Figure 4-3. *Cumulative distribution function of β parameter for Task 6D.*

Table 4-4. Moments of parameter β for Task 6D.

<β> (h/m)	σ_β (h/m)
544927	522926

Breakthrough time history for the tracers

Breakthrough curves for measured injection curves

We will now present the results of the calculated BTCs using the parameters given in Table 4-1 and Table 4-3. The calculated BTCs are compared with the measured data in Figure 4-4. The symbols are the measured data: the red squares are for I-129, the green squares for Ca-47 and the blue squares for Cs-137. The lines are the simulated BTCs. The red line is for I-129, the green line for Ca-47, the blue for Cs-137, the cyan for Ra-226, the orange for Tc-99 and the purple for Am-241. This symbol and line convention will be used in all the BTC figures through this report.

For I-129 the comparison between the simulated BTCs and the measured data shows that the simulated BTC closely represents the measured BTCs up to 160 hours. Then there is a jump of the BTC data. The simulations then underestimate the measured BTCs slightly.

For Ca-47 the simulated BTC is shifted to the right. This may be mainly due to the fact that the K_a value was obtained from the fracture coatings and thus the retention of Ca-47 was overestimated.

For Cs-137 the measured data are too few to show a definite trend and pattern. It can be clearly seen, however, that the simulated BTC deviates from the measured data points. This is probably also due to an overestimate of the K_a parameter.

For Ra-226, Tc-99 and Am-241 there are no data of the measured BTCs available and therefore no comparisons can be made.

Ra-226 is generally less sorptive than Cs-137. So the simulated BTC for Ra-226 is higher and shifted to the left compared with that of Cs-137. Ra-226 thus has weaker retention than Cs-137.

Tc-99 and Am-241 are the strongest sorbing tracers. Therefore they have the strongest retention as shown in Figure 4-4.

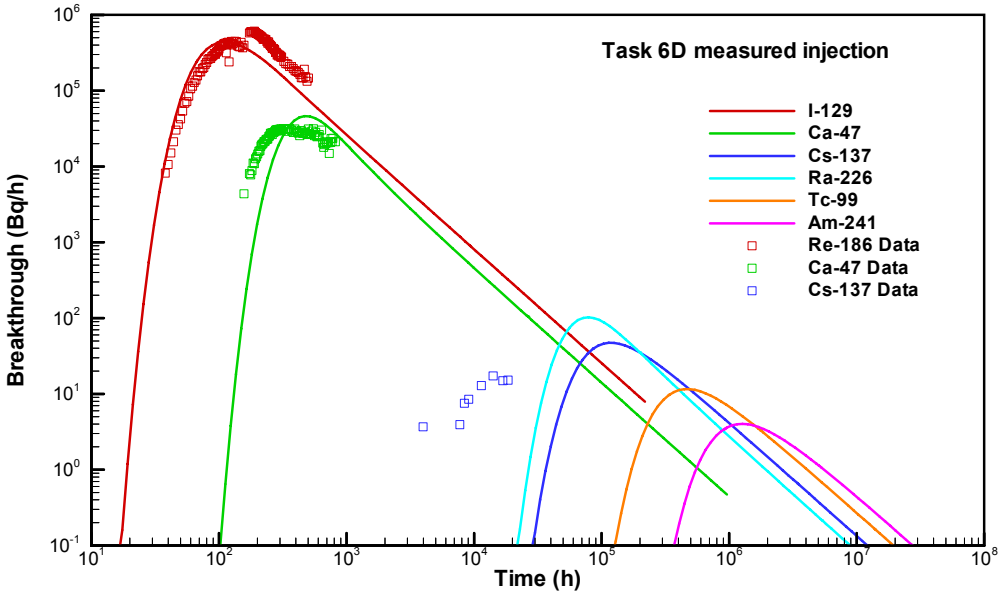

Figure 4-4. *Calculated BTCs for measured injection for Task 6D. Lines are the simulated BTCs. Symbols are the measured BTCs.*

In Table 4-5 the times for 5%, 50% and 95% mass recovery for the measured injection are presented.

Table 4-5. Times of 5%, 50% and 95% mass recovery for the measured injection for Task 6D.

Tracer	T_5 (h)	T_{50} (h)	T_{95} (h)
I-129	78.9	325.0	927.0
Ca-47	341.7	1067	26470
Cs-137	8.61E+4	4.32E+5	1.38E+7
Ra-226	5.59+4	1.99E+5	5.40E+6
Tc-99	3.40E+5	1.76E+6	5.69E+7
Am-241	9.19E+5	5.08E+6	1.67E+8

Breakthrough curves for Dirac pulse injection

The simulated BTCs for the Dirac pulse injection are shown in Figure 4-5. The curves clearly have the similar shape and trend as the simulated BTCs for measured injection (compare with Figure 4-4).

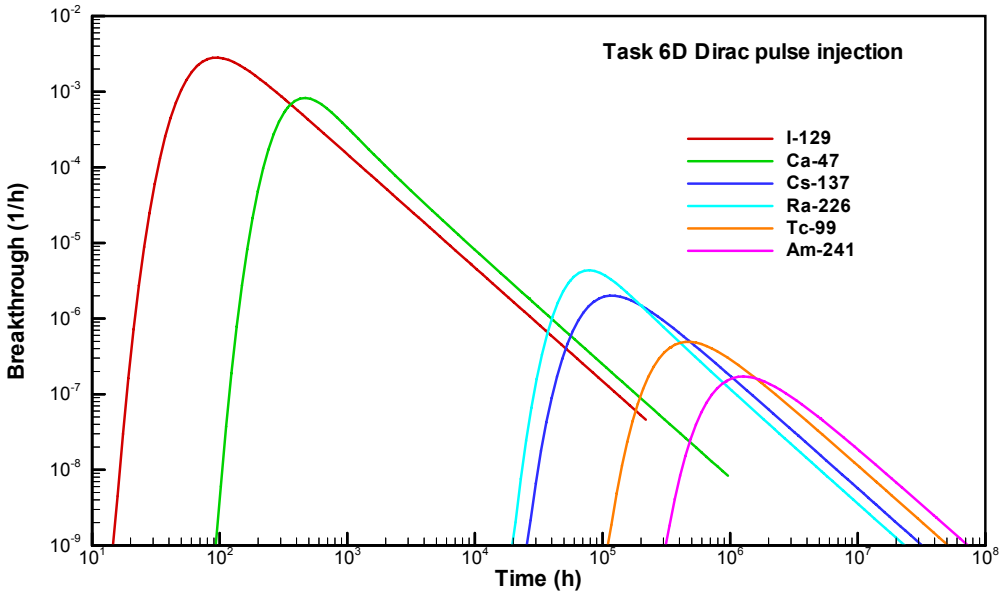

Figure 4-5. *Calculated BTCs for Dirac pulse injection for Task 6D.*

In Table 4-6 the times of 5%, 50% and 95% mass recovery for Dirac pulse injection are summarized. These times are quite close to the times for measured injection given in Table 4-5.

Table 4-6. Breakthrough times of recovery of 5, 50 and 95% for Dirac pulse injection for Task 6D.

Tracer	T_5 (h)	T_{50} (h)	T_{95} (h)
I-129	68.0	307.3	9457
Ca-47	328.8	1053	26510
Cs-137	8.59E+4	4.32E+5	1.39E+7
Ra-226	5.58E+4	1.99E+5	5.43E+6
Tc-99	3.40E+5	1.76E+6	5.71E+7
Am-241	9.19E+5	5.08E+6	1.68E+8

Maximum release rate

The maximum release rates of all tracers are presented in Table 4-7 for measured injection and in Table 4-8 for Dirac pulse injection.

Table 4-7. Maximum release rate for measured injection for Task 6D.

Tracer	I-129	Ca-47	Cs-137	Ra-226	Tc-99	Am-241
Max rate (Bq/h)	4.4E+5	4.6E+4	47.1	102.5	11.6	4.0

Table 4-8. Maximum release rate for Dirac pulse injection for Task 6D.

Tracer	I-129	Ca-47	Cs-137	Ra-226	Tc-99	Am-241
Max rate (1/h)	2.8E-3	8.3E-4	2-0E-6	4.4E-6	4.9E-7	1.7E-7

4.4 Sensitivity analysis

4.4.1 Effect of discretization on β and τ parameters

As described above in this report the flow and particle tracking simulations are performed in two steps. The first step simulation is performed on the 200 m × 200 m × 200 m cubic block of rock with a size of 2 m × 2 m × 2 m for each element. The second step simulation is performed in the selected inner 100 m × 100 m × 100 m cubic volume with a size of 1 m × 1 m × 1 m for each element. The boundary condition (the head values) for the second step simulation is obtained from the first step simulation. The particle tracking simulations are performed in both steps of simulations. The second step simulation in a smaller block of rock using finer discretization is also the basic case where the BTC results are obtained in this report. The results of the first step simulation in a larger block of rock volume with a coarser discretization can be compared with the basic case. As the particle tracking simulations are performed between the same injection and pumping sections for both steps of simulations, the results of the two steps of simulations are thus comparable. The injected particles are traced, β and τ values are recorded at the pumping section in both steps of simulations. Figure 4-6 shows the simulated β - τ scattergrams from the two steps of simulations. The red symbols are the β - τ values from the finer grid simulation (the second step simulation), while the green symbols are those from the simulations with coarser discretization (the first step simulation). The τ - β values from the coarser grid simulation span a larger range compared with the τ - β values from the finer grid simulation.

Table 4-9 shows the comparison of the moments from the two simulations. The coarser discretization has a lower mean water residence time and higher variance. There may be two reasons for the deviation of the moments. The first reason may be due to the discretization itself. The other reason may be due to the using of boundary conditions obtained from the simulation of first step.

The values of the slope k from both discretizations are generally matched, the values are also consistent with the apertures of the structures.

Table 4-9. Moments of τ and β from the simulations with finer and coarser discretizations.

Size of elements (m)	<τ> (h)	σ_τ (h)	<β> (h/m)	σ_β (h/m)	Slope k (m^{-1})
1×1×1	55.6	15.3	544927	522926	16557
2×2×2	44.0	26.4	742546	389524	15755

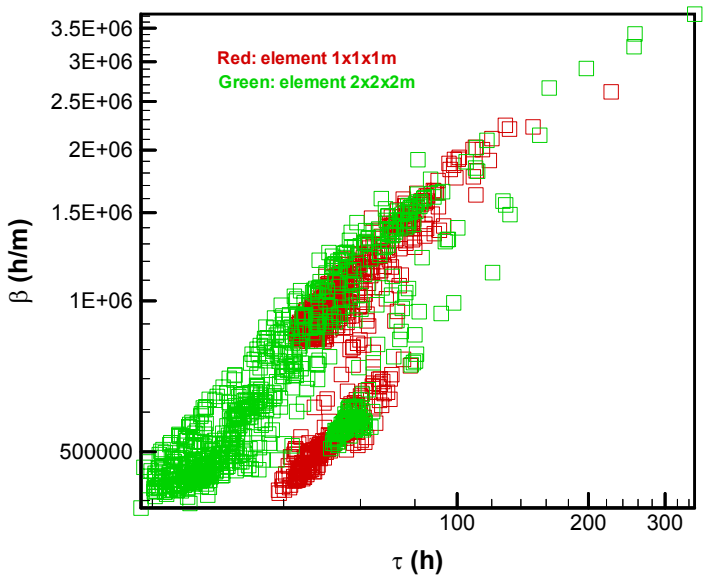

Figure 4-6. *Effects of discretization on β and τ simulation results. The red symbols are β and τ results from finer discretization. The green symbols are those for coarser discretization.*

In Figure 4-7 the simulated BTCs from the temporal moments of two discretizations (Table 4-9) are compared, the retention parameters (κ and K_a) are the same. The solid lines are the modelled BTCs based on the temporal moments from the finer discretization. The dashed lines are the modelled BTCs from the coarser discretization. The symbols are the measured data.

As the mean of τ is lower and the variance of τ is higher for the coarser discretization, all the simulated BTCs from the coarser discretization arrive earlier at the pumping borehole compared to the BTCs of the finer discretization. The initial parts of the modelled BTCs are shifted to the left and the peaks are higher in the case of coarser discretization. The deviations diminish in the tail parts.

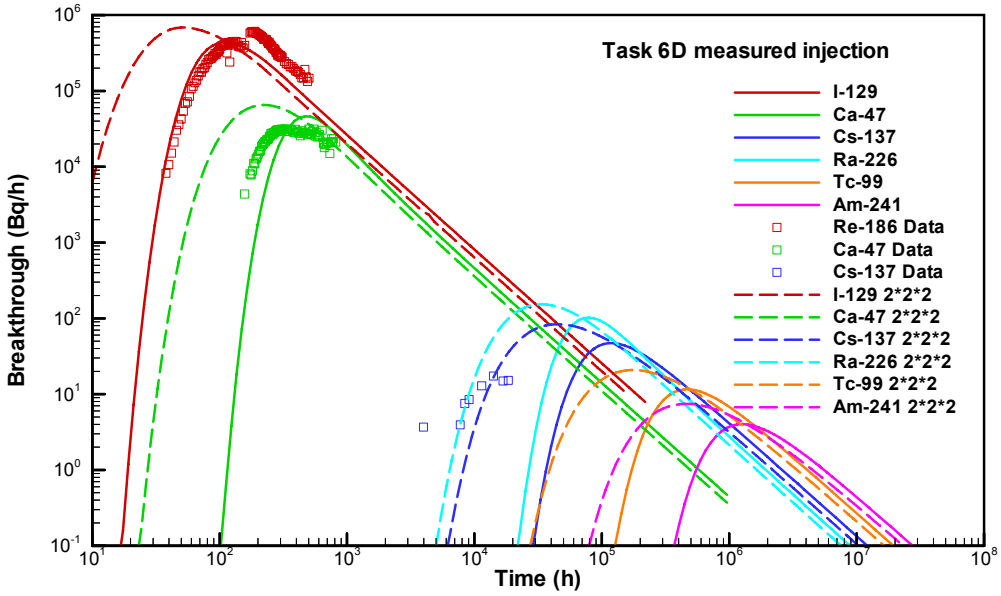

Figure 4-7. *BTCs for coarser and finer discretizations. The solid lines are the modeled BTCs from the finer discretization. The dashed lines are the modelled BTCs from the coarser discretization. The symbols are the measured data.*

4.4.2 Effects of the background structures

To study the effects of the background structures on tracer transport and retention properties we also performed two cases of simulations. The basic case is the same as that in the previous section in the inner 100 m cubic block of rock with 1×1×1m discretization. All structures are included in the model in the basic case. In the comparing case, the background structures are excluded while only the deterministic structures remain. We compare first the simulation results of τ - β relations for the two cases.

The τ - β scattergrams with background structures and without background structures are compared in Figure 4-8. The green symbols represent the τ - β scattergram with only the deterministic structures and without the background structures. The red symbols designate the τ - β scattergram with all structures, including the background structures. In both cases we inject 729 particles and track them between the same injection and pumping sections. The scattergram of the red symbols is the same as that shown previously in Figure 3-16. As discussed earlier, the scattergram of the red symbols is clearly divided into two groups, one for the deterministic structures and the other for the background fractures. If we have only deterministic structures, the scattergram clusters more closely together to form one group. Interestingly the scattergram is located between the two groups formed when all structures are accounted for.

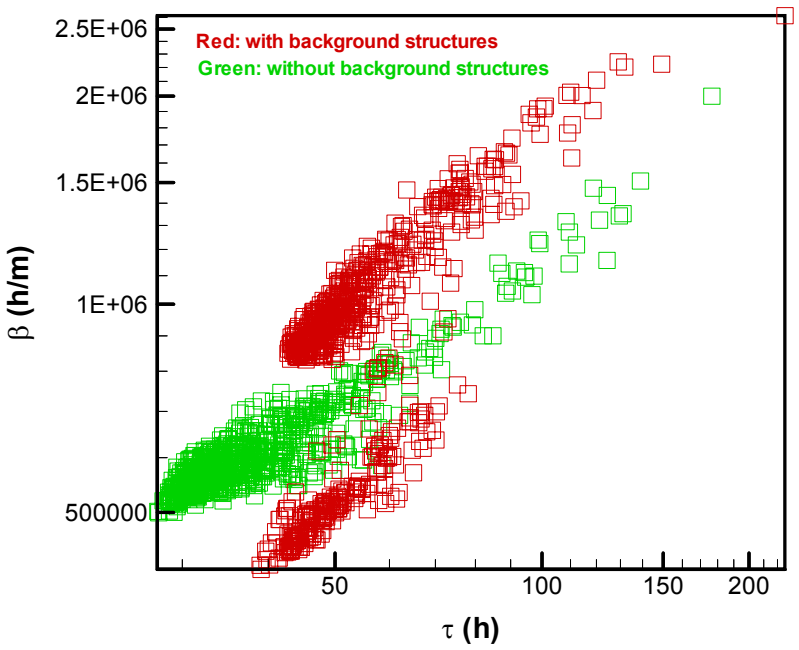

Figure 4-8. *Comparison of τ and β scattergrams with and without background structures. The green symbols represent τ and β scattergram with only the deterministic structures. The red symbols designate τ and β scattergram with all structures.*

The moments of τ and β for two cases are shown in Table 4-10. The case with only the deterministic structures has lower mean water residence time and about the same level of variance as for the case with all structures.

Table 4-10. Moments of τ and β with and without background structures.

Background structures inclusion	<τ> (h)	σ_τ (h)	<β> (h/m)	σ_β (h/m)	Slope k (m^{-1})
No	41.1	16.2	632260	145007	14472
Yes	55.6	15.3	544927	522926	16557

The BTCs for the two cases (with and without the background structures) are compared in Figure 4-9. The solid lines are the modelled BTCs with all structures. The dashed lines are the modeled BTCs with only deterministic structures. The symbols designate the measured data. The lower value of τ in the case in which the background structures are not included tends to produce modeled BTCs that are shifted to the left and are higher in the initial parts for all tracers. Again the tail parts of the BTCs are closer for both cases. If we compare these two cases including or excluding the background structures with the two cases in the previous section of coarser and finer discretizations, it shows that all the cases have about the same mean water residence time. However, in the previous section we have a larger difference of variances for the two cases with different grids of discretizations than for the two cases of different structures (see Table 4-8 and 4-9). It is observable in Figures 4-8 and 4-9 that a larger difference of variances yields modelled BTCs that are shifted even further to left and even higher (Figure 4-8).

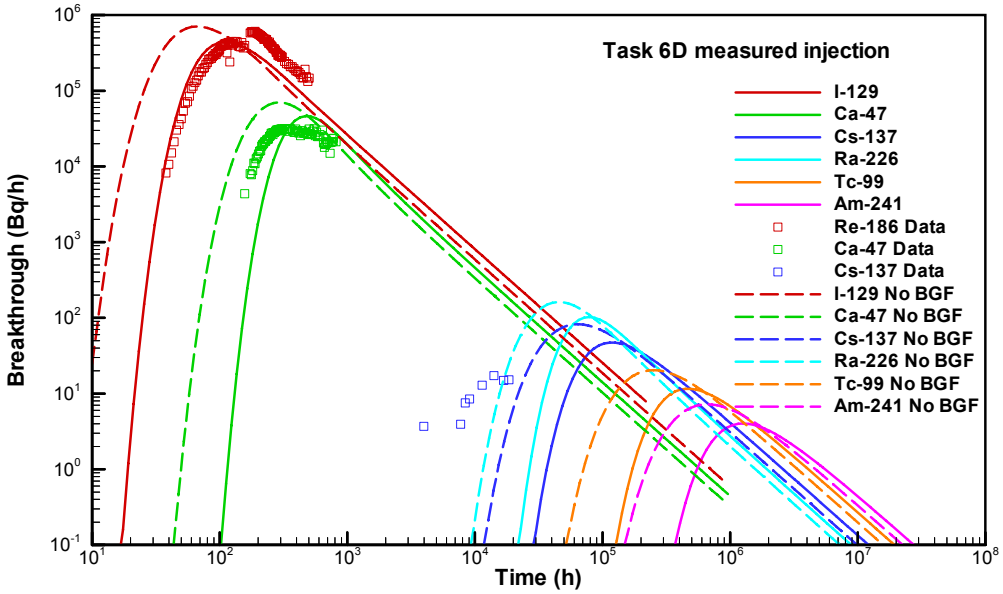

Figure 4-9. *BTCs with and without background fractures. The solid lines are the modelled BTCs with all structures. The dashed lines are the modelled BTCs with only deterministic structures. The symbols are the measured data.*

4.4.3 Depth-dependence of the porosity θ, the diffusivity D and sorption coefficient K_d

Porosity profile

Table 3-3 summarized the porosity profile for structure Type 2 at different depths in the rock matrix. The porosity is generally decreasing as the depth into the rock matrix increases.

Table 3-4 and Table 3-5 summarized the porosity profile at different depths for Part A and Part B of the rock matrix for structure Type 1 (Figure 3-13).

Depth-dependent variability

We neglect the advection in the rock matrix, and assume that the concentration in the rock matrix is governed by the Fick's second law:

$$\frac{\partial C}{\partial t} = \frac{\partial}{\partial z}\left[\frac{D}{R}\left(\frac{\partial C}{\partial z}\right)\right] \tag{4-1}$$

where $R = 1 + \frac{K_d \rho}{\theta}$ is the retardation factor. The boundary condition is specified as $C(0, t)$ which is the tracer concentration in the open fracture. Two parameters, D and R control the concentration according to Eq. (4-1).

According to Archie's law, the formation factor is related to the porosity θ as

$$F = 0.71\theta^{1.58} \tag{4-2}$$

which is applicable to all individual retention zones in the rock matrix. From the relation $D_e = D\theta$, the pore diffusivity D can be expressed as:

$$D = 0.71\theta^{0.58} D_w \tag{4-3}$$

D and R are then depth-dependent.

For a given retention zone *j*, Eq. (4-1) has the solution (D and R assumed constant):

$$C(z,t)/C_0 = C^{'}(z,t) = \left(1 - erf\,\frac{z}{\sqrt{4D_j t / R_j}}\right) \qquad (4\text{-}4)$$

where *j* represents *j*th retention zone (e.g., altered zone, cataclasite or fault gouge zone).

Our objective is to determine the effective retention parameters for the entire immobile zone (rock matrix). The immobile zone for both types of structures consists of several parallel retention zones (Figure 3-12, 3-13). Equation (4-4) is applicable for individual zones, while different zones may have different retention parameters. We have to calculate the concentration *C*(*z, t*) zone by zone. The concentration obtained at the end boundary of a previous zone will serve as the initial concentration for the subsequent zone, and so on.

The penetration profile *C*(*t*, *z*) (Eq. 4-4) could be estimated as a function of depth *z* at a specified time *t*. The time should be that when most of the mass has been recovered, and after which the penetration slows down significantly. For the purpose of Task 6D, we choose the time at which 85% mass is recovered from the BTCs in the previous section (Figure 4-9) for estimating penetration depths. We also need to specify a relative concentration C/C_0 to define an "effective" depth *z*. As a cut-off for defining the penetration depth we choose the relative concentration $C/C_0 = 0.15$; at approximately this value the first derivative with respect to z is significantly reduced whereby the profile curves start a relatively slow convergence to zero. Thus for $C/C_0 > 0.15$ we capture the bulk of the penetrated mass and consider this appropriate for obtaining an effective porosity.

Eq. (4-4) is strictly valid only for constant parameters D, R and constant C_0 in open fractures. We have concentrations (or BTCs) varying with time in the fracture. Cvetkovic and Cheng (2002) have compared the concentration profiles obtained numerically with time-varying boundary conditions (proportional to the breakthrough curve), with profiles obtained from Eq. (4-4); it was found that Eq. (4-4) provides a reasonable approximation. Given all uncertainties in the system, we consider Eq. (4-4) as a reasonable approximation for estimating the penetration profiles which are used for averaging/inferring an "effective" porosity and K_d.

Table 4-11 summarizes the times of 85% mass recovery based on the modelled BTCs for the measured injection from the calibration procedure (Figure 4-9).

Table 4-11. Initial retention parameters from the altered zone and times of 85% mass recovery from the BTCs in Figure 4-9.

Tracer	T (h)
I-129	2344
Ca-47	6731
Cs-137	3.4e+6
Ra-226	1.4e+6
Tc-99	1.4e+7
Am-241	4.1e+7

In structure Type 2 (non-fault) it is expected that the matrix diffusion takes place only in the altered zone as the fracture coatings are considered to be the fracture surface and the tracers are not expected to have long enough time to reach the intact rock during the period of tracer test.

We let the time t in Eq. (4-4) to be the 85% recovery, and then calculate the normalized concentration as a function of the penetration depth z by Eq. (4-4). Figure 4-10 plots the penetration profiles for the altered zone in structure Type 2 for all tracers. It is observed that at a depth of 50 mm the relative concentrations are already low (less than 15%) for all modelled tracers. It can then be concluded that the retention in structure Type 2 is primarily in the altered zone.

If $C/C_0 = 15\%$ is chosen as a limit, we get the penetration depths for all tracers in structure Type 2 that are summarized in Table 4-12. The effective values of θ and K_d are obtained from the penetration depths as shown in Table 4-12. For structure Type 2, the effective values of θ and K_d are the same as the values of the altered zone.

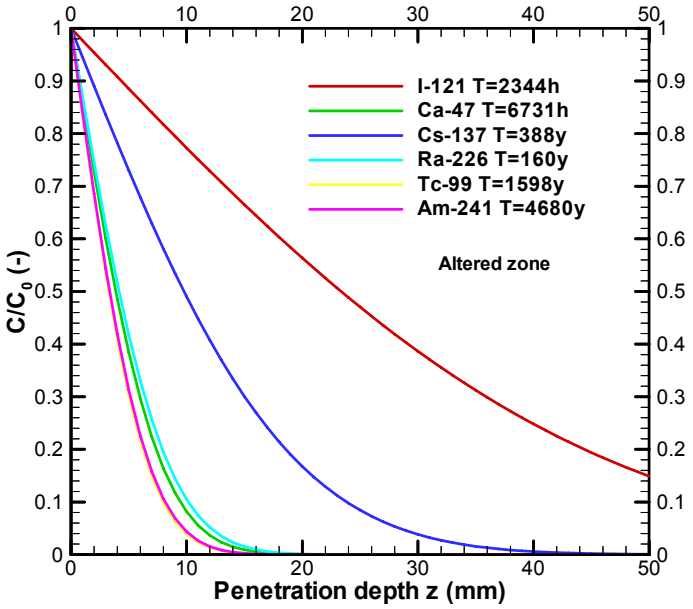

Figure 4-10. *Penetration profiles for all tracers in the altered zone in structure Type 2.*

Table 4-12. Penetration depths at 15% relative concentration of different tracers in structure Type 2.

Tracer	Altered zone (mm)	θ (%)	K_d (m^3/kg)
I-129	50	0.6	0
Ca-47	8	0.6	8.8E-5
Cs-137	21	0.6	2.0E-2
Ra-226	9	0.6	1.8E-2
Tc-99	7	0.6	0.2
Am-241	7	0.6	0.5

For structure Type 1 calculations of the penetration profiles should be performed separately for the two parts of the matrix. In Part A of the matrix, the tracers diffuse into the cataclasite zone and probably also into the altered zone. In Part B, the tracers first diffuse into the fault gouge zone and then into the altered zone.

Figure 4-11 shows the penetration profiles for Part A of the matrix, Figure 4-12 for Part B.

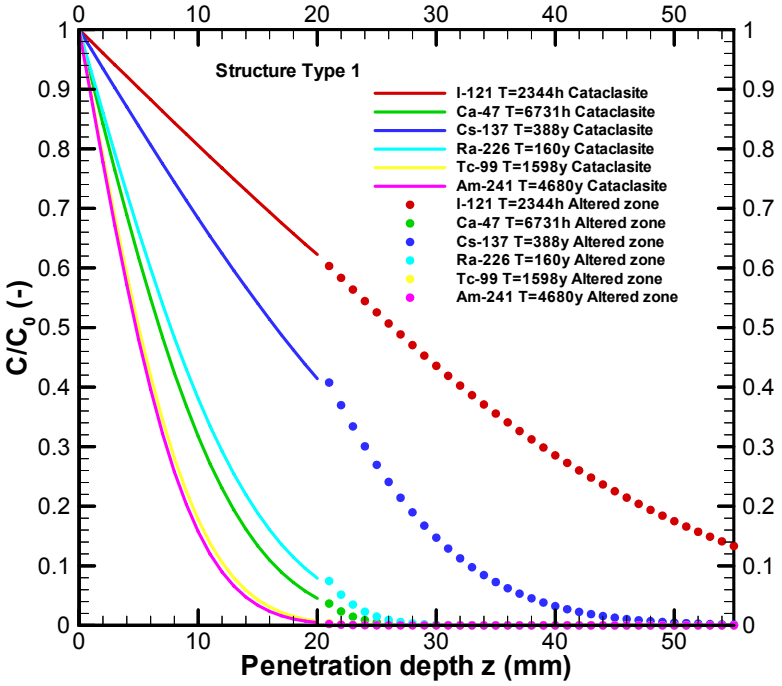

Figure 4-11. *Penetration profiles Part A of the matrix in structure Type 1.*

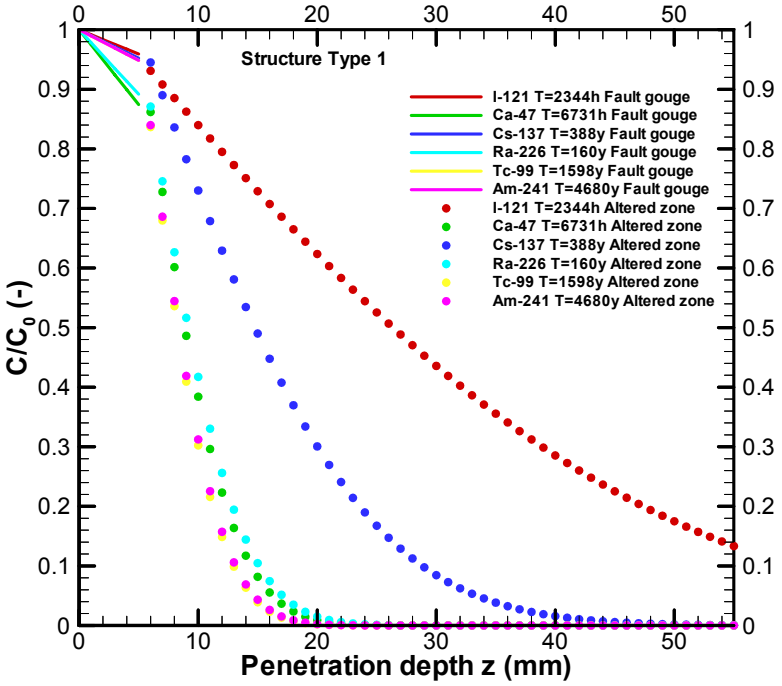

Figure 4-12. *Penetration profiles for Part B of the matrix in structure Type 1.*

At the limit of C/C_0 = 15% we obtain the penetration depths for all tracers for both parts of the matrix in structure Type 1. The results are presented in Table 4-13.

Table 4-13. Penetration depths, effective porosities and effective K_d values in structure Type 1.

Tracer	Penetration depth in Part A (mm)	Penetration depth in Part B (mm)	Effective θ (%)	Effective K_d (m^3/kg)
I-129	53	53	1.6	0
Ca-47	14	13	4.4	1.9E-4
Cs-137	30	26	2.5	3.1E-2
Ra-226	16	14	4.0	3.6E-2
Tc-99	10	12	5.0	0.2
Am-241	11	12	5.2	0.5

From Table 4-13 we find that the penetration depths of the tracers vary. In Part A of the matrix, some tracers diffuse only into the cataclasite (Ca-47, Ra-226, Tc-99 and Am-241) while others (I-129 and Cs-137) diffuse into the altered zone. In Part B of the matrix, all tracers have passed through the fault gouge zone and diffuse further into the altered zone.

The effective value for θ and K_d, for the entire matrix is needed in order to calculate the BTCs. A simple depth-weighted average method will be used to obtain the effective values of θ and K_d. Take I-129 in structure type 1 as an example. I-129 penetrates 53 mm into the rock matrix on each side of the fracture zone. On the left side, the first 20 mm is the cataclasite and the next 33 mm is the altered zone. On the right side the first 5mm is the fault gouge and the next 48 mm is altered zone. So we have 20 mm of the cataclasite zone, 5 mm of the fault gouge zone and 81 mm of the altered zone out of a total 106 mm thick of the penetration zone. An effective θ is then calculated as:

$$\theta_{eff} = \frac{20}{106} \times 1 + \frac{5}{106} \times 20 + \frac{81}{106} \times 0.6 = 1.6$$

We thus have an effective porosity of 1.6% for I-129. Effective porosities for other tracers are calculated in a similar way. The sorption distribution coefficient K_d is also calculated by the same weighing method. The calculated results are presented in the last two columns in Table 4-15.

The strongly sorbing tracers (e.g., Tc-99 and Am-241) penetrate only into the zone near the fracture surface that has the highest porosity, while the conservative tracers diffuse through zones of high porosities and into a zone of low porosity.

Now the values of porosity and sorption distribution coefficients for both structure types for every tracer have been obtained. In Figure 4-1 it indicates that there are two main flow paths for the tracer particles: one runs only through the four deterministic structures (structures 23→22→20→21), and the other runs through the background fractures. Consider the flow path that lies in the four deterministic structures. The four structures have the types: 23 (Type 2), 22 (Type 2), 20 (Type 1) and 21 (Type 2). Table 4-14 shows the travel time and the transport distance of one particle trajectory.

Table 4-14. Travel time and transport distance (example from one particle).

Structure	Structure Type	Transport distance (m)	τ (h)
23D	2	6.6	16.0
22D	2	25.9	57.6
20D	1	22.8	7.2
21D	2	3.3	< 0.1
Total		58.6	80.8

From Table 4-14, it can be observed that the structures 22 and 20 contain a large fraction of the total transport distance and therefore the main part of the flow paths. Based on this fact further simplification can be made for the retention parameters (θ and K_d) to be used in the model. As the structures 22 and 20 make up the main part of the flow paths, it suffices to derive the retention parameters only from the parameters for the structures 22 and 20. The structure 20 is of Type 1 while the structure 22 is of Type 2. As is shown in Table 4-14 the transport distances are about the same in both structures 20 and 22. For computing simplicity we therefore assume that all particles travel through the deterministic structures and the flow paths contain 50% of Type 2 structure and 50% of Type 1 structure, respectively. The values of θ and K_d are obtained as averages of the values in the two structure types. Table 4-15 lists the values of θ and K_d thus obtained. For particles travelling through the background structures, they will travel through many structures. These structures contain both structure Type 1 and structure Type 2. Instead of making detailed calculations for every particle in every structure, we assume that the two structure types (Types 1 and 2) are evenly distributed, i.e. 50% of Type 1 and 50% of Type 2. The values of θ and K_d are obtained as averages of the values from the two structure types for the background structures as well.

Table 4-15. Values of θ and K_d obtained by simplification of the deterministic and background structures.

Tracer	θ (%)	K_d (m^3/kg)	D_w (m^2/h)[A)]	κ (m $h^{-1/2}$)
I-129	1.1	0	7.20E-6	6.7e-6
Ca-47	2.5	1.4E-4	2.85E-6	4.9e-5
Cs-137	1.6	2.6E-2	7.45E-6	7.3e-4
Ra-226	2.3	2.7E-2	3.20E-6	6.5e-4
Tc-99	2.8	0.2	1.80E-6[B)]	1.6e-3
Am-241	2.9	0.5	2.14E-6[C)]	2.8e-3

The BTCs calculated from the parameters in Table 4-15 are compared with the BTCs based on the parameters from the calibration procedure (Table 4-1) and the comparison is presented in Figure 4-13. The deviations between the two cases are larger for the less sorptive tracers than those for the more sorptive tracers. The BTCs of the conservative tracer have the largest deviation.

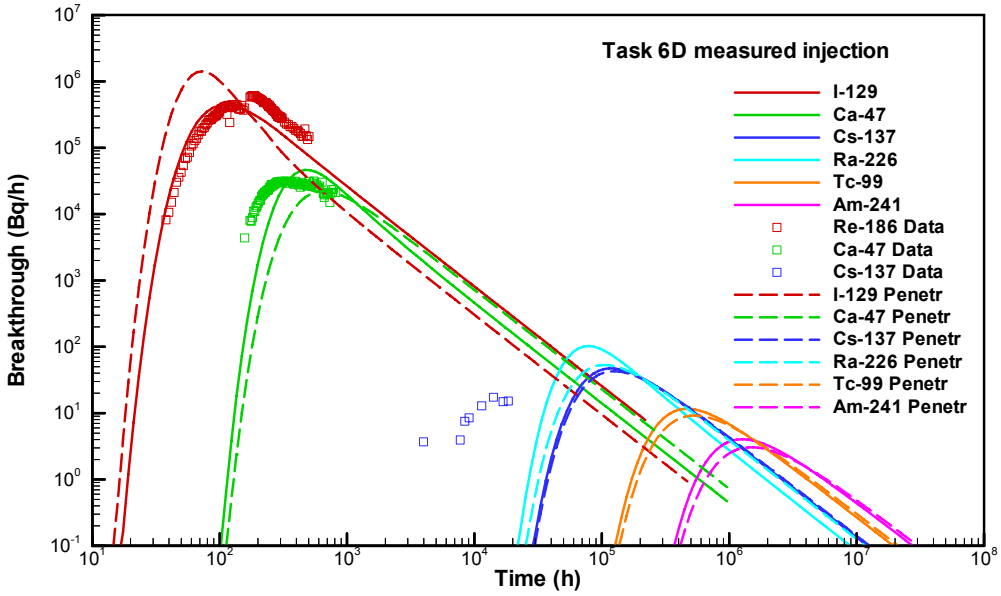

Figure 4-13. *Comparison of modelled BTCs based on the parameters from the calibration (solid lines with the parameters from Table 4-1), and the BTCs based on the parameters from the penetration analysis (dashed lines with the parameters from Table 4-15).*

5 Task 6E

5.1 Modelling strategy

Similar to the modelling for Task 6D, a 3-dimensional configuration constructed from Task 6C model is used in this report. The flow field has been solved using MODFLOW 2000 (Harbaugh et al., 2000). All structures (deterministic, synthetic and background) have been accounted for. A constant transmissivity is assumed for a given structure (from the data delivery) and different values are used for different structures. The rock matrix is treated as a no-flow (inactive in MODFLOW2000) region.

In Task 6D the simulation was performed in two steps, and was focused on a smaller inner block where the transport took place. In Task 6E, the flow calculations are performed directly on the 200 m cubic block with a discretization of 8 million cells where each cell has a dimension of 1×1×1m.

5.2 Model calibration

In Task 6D, the effective retention parameters θ and K_d are obtained by calibration on the measured BTC data for the C2 tests. The porosity θ is assumed to be a constant for all tracers, while K_d is tracer-dependent. In the sensitivity studies for Task 6D, we account for the depth-dependence of the retention parameters, where the effective retention parameters are both tracer-dependent and depth-dependent. The complexity factor is not explicitly accounted for in Task 6D modelling.

In the Task 6E modelling, we extend the methodology used in the Task 6D sensitivity studies. We account for both the geological types and the complexity factors for each tracer along its flow path.

5.3 Depth-dependence of the retention parameters

5.3.1 Complexity factor

The hydrodynamic characterization at the Äspö site shows that many structures are made up of several conductive features and the number of sub-parallel features/fractures may vary over the extent of the structure. Thus, a structure may at one location consist of a single fracture of Geological Structure Type 1, while at another location it may consist of two fractures of Geological Structure Type 1 and 2, respectively. Larger scale structures may consist of tens or more of sub-parallel hydraulically conductive fractures. As the possible combination of fractures/features within a structure is immense, a simplified classification scheme is introduced. A complexity factor ranging from 1 to 5 will be assigned to different Geological Structure Types. A Complexity Factor of 1 represents structures consisting of a single feature while a Complexity Factor of 5 represents structures consisting of more than 10 features.

The procedures of assignment are as follows. First, every conductive structure is classified to a primary Geological Structure Type: either Geological Structure Type 1 (Fault) or Geological Structure Type 2 (Non-fault). Secondly, each structure is assigned a complexity factor ranging from 1 to 5. Table 5-1 shows the assignment of the Complexity Factors in Task 6C modelling.

Table 5-1. Complexity factors assigned to the synthetic structures in Task 6C.

Complexity Factor	Number of (sub-parallel) conductive features/fractures per structure	Percent of primary geological structure type or combination of geological structure types (by area)
1	1	90-100%
2	1 to 2	70 to 100%
3	1 to 3	50 to 90%
4	3 to 10	50 to 90%
5	10+	50 to 90%

For the modelling of Task 6E, we have to specify the exact percentage of the primary geological structure type for each value of the complexity factor. In consistence with Table 5-1, we assign values of the complexity factors to the different geological structures used in the Task 6E modellings as shown in Table 5-2.

Table 5-2. Assigned values of the complexity factor used in Task 6E.

Complexity Factor	Number of (sub-parallel) conductive features/fractures per structure	Percent of primary geological structure type or combination of geological structure types (by area)
1	1	100%
2	1 to 2	90%
3	1 to 3	70%
4	3 to 10	70%
5	10+	70%

A flow path is defined as a path from the tracer release point to the tracer arrival point at the corresponding CP. A flow path usually consists of several conductive structures. These structures often have different values of complexity factor and different geological structure types. During a particle tracking simulation, we need to follow the particles and find the percentage of each geological structure type in the whole path.

A simply weighted average method based on the length of the structures is introduced to calculate the percentage of each geological structure type in a flow path. Figure 5-1 shows an example of a flow path. This flow path is made up of four structures: S_1, S_2, S_3 and S_4. The values of the complexity factor and the types of geological structures of them are assumed in Table 5-3.

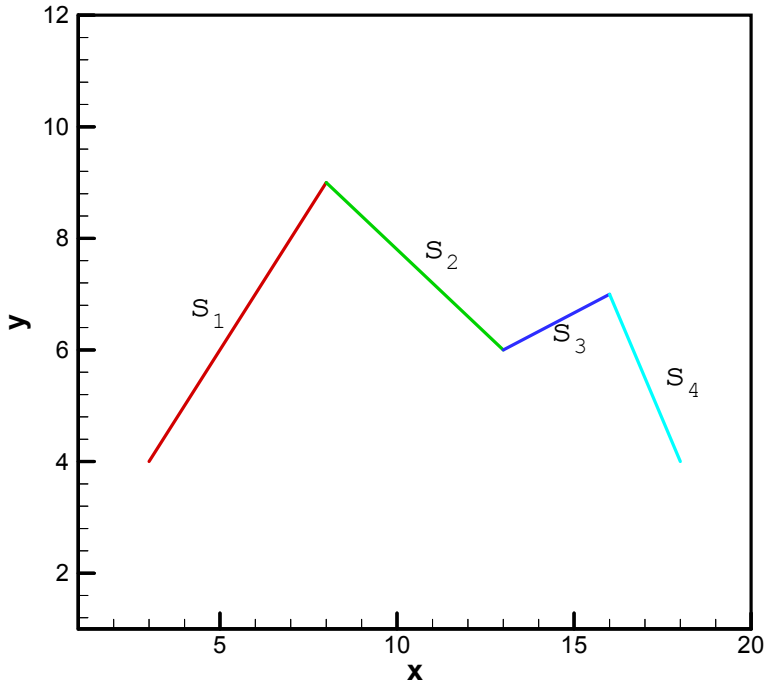

Figure 5-1. *An example of a flow path illustrating the calculation of the percentage of each geological structure type in the flow path.*

Table 5-3. Complexity factors and the geological structure types for the example flow path shown in Figure 3-18.

Structure	Geological structure type	Complexity Factor	Type 1 (%)	Type 2 (%)
S_1	2	1	0	100
S_2	1	2	90	10
S_3	2	2	10	90
S_4	1	3	70	30

For the flow path shown above, the percentage of geological structure type 1 is calculated as $(0\times l1 + 0.9\times l2 + 0.1\times l3 + 0.7\times l4\ )/l$ where l is the total length of the flow path and l_i is the length of the structure i. Similarly the percentage of geological structure type 2 is calculated as $(1.0\times l_1 + 0.1\times l_2 + 0.9\times l_3 + 0.3\times l_4\ )/l$. With the same averaging procedure we can obtain the effective values of the geological structure type and of the complexity factor for a flow path. As many particles will be injected, these particles may transport through different flow paths. Ensemble mean values could be obtained by averaging over all particles for the percentage of each type, for the complexity factors and for the geological types. Table 5-4 summarizes the average geological type and the complexity factor for three CPs in Task 6E.

Table 5-4. Summary of the average geological type, the complexity factors, and the percentage of each structure type at three CPs.

CP	<Geological type>	<Complexity factor>	Type 1 (%)	Type 2 (%)
X=1920 m	1.88	2.12	17.2	82.8
X=1880 m	1.29	2.36	59.6	39.4
X=1800 m	1.18	2.22	70.4	29.6

5.3.2 Effective retention parameters

We consider the in-depth heterogeneity in the same way as for Task 6D. For both fracture types, the fracture coatings are considered as the fracture surface and they are assumed to be evenly distributed within a thickness of 0.25 mm on both sides of the open fracture. The K_a values are calculated from the respective K_d values of the coatings given in the Task 6C model (Table 3-11).

For structure Type 2, the structures are assumed to be symmetric along the z-direction about the open fracture (Figure 3-12). Table 3-3 summarizes the porosity profile for structure Type 2 at different depths in the rock matrix.

As is shown in Figure 3-13, structure Type 1 has two parts. The porosity profiles at different depths within the rock matrix for structure Type 1 are shown in Table 3-4 and Table 3-5.

The concentration profile over depth is given by Eq. (4-4), which depend on the tracer and depth. In the following we calculate the effective retention parameters for the calculation of the BTCs at three CPs.

At x = 1920 m

We need to find out the effective values of the retention parameters (θ and K_d) for each tracer for the entire rock matrix. The following are the calculation procedures:

1. Obtain the initial values of parameters from the Altered zone;
2. Calculate BTC for the extended pulse injection, and obtaining times for 85% recovery for every tracer;
3. Use the obtained times to calculate penetration depth for the tracers into different structure types;
4. Find the depths where $C(z, t)/C_0 = 0.15$;
5. Use the depths to calculate the effective θ and K_d;
6. Average over the structure types.

We use the parameters for the altered zone as the initial retention parameters to calculate the BTCs for all tracers at the CP of x = 1920 m. The temporal moments are obtained from Table 3-8 for x = 1920 m. The initial values of the parameters and the times of 85% mass recovery from the BTCs calculated from the initial values are presented in Table 5-5.

Table 5-5. Initial values of sorption and diffusion parameters used in Task 6E at *x* = 1920 m (Altered zone) and the times for 85% mass recovery.

Tracer	D_w (m^2/h)	K_d (m^3/kg)	κ (m $y^{-1/2}$)	K_a (m)	T (y) (85%)
I-129	7.20E-6	0	2.88e-4	0	935.6
Ca-47	2.85E-6	8.8E-5	1.15e-3	3.2E-4	3969
Ra-226	3.20E-6	1.8E-2	1.73e-2	6.0E-2	7.82E+5
Cs-137	7.45E-6	2.0E-2	2.78e-2	6.8E-2	2.052E+6
Tc-99	1.8E-6	0.2	4.32e-2	0.26	4.882E+6
Am-241	2.14E-6	0.5	7.45e-2	0.65	1.452E+7

To proceed, we let the time *t* in Eq. (4-4) to be the 85% recovery time in Table 5-5 and use the retention parameters as shown in Table 5-5 to calculate the normalized concentration using Eq. (4-4) as a function of the penetration depth *z*. Figure 5-2 shows the penetration profiles for structure Type 2 for all tracers. It is observed that at a depth of 50 mm the relative concentrations decrease more rapidly due to the transition from the altered zone to the intact rock. For different tracers the rates of the concentration decrease are different as the tracers penetrate deeper into the rock matrix. The concentrations of the two strongly sorbing tracers (Tc-99 and Am-241) decrease most rapidly while the conservative tracer (I-129) has the lowest decreasing rate.

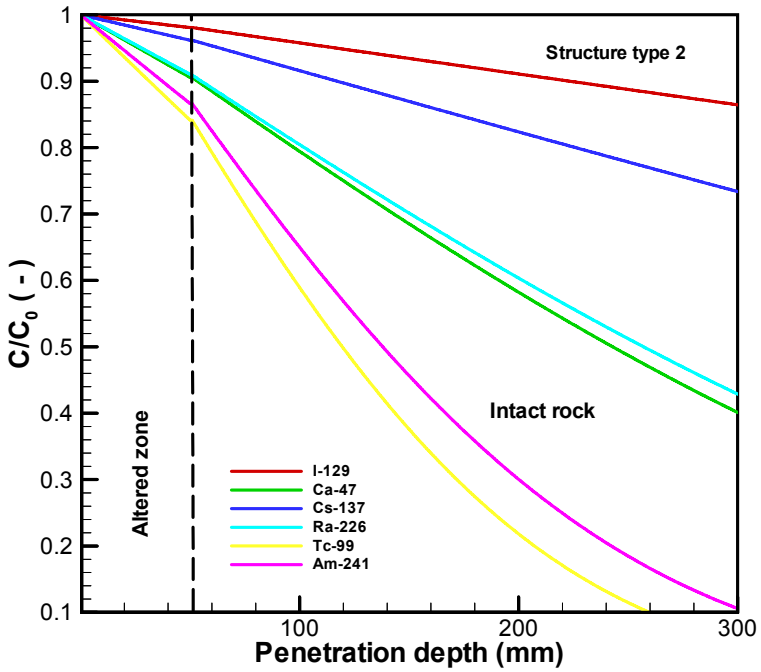

Figure 5-2. *Penetration profiles for all of the tracers in the altered zone in structure Type 2. The profiles are calculated at the times of 85% mass recovery shown in Table 5-5. The times are 936y for I-129, 3969y for Ca-47, 7.82E+5y for Ra-226, 2.05E+6y for Cs-137, 4.88E+6y for Tc-99 and 1.45E07 for Am-241.*

For structure Type 1 calculations of the penetration profiles should be performed separately for the two parts of the rock matrix. Using the parameters in Table 5-5 and the same procedures as for the Type 2 structure, we obtain the penetration profile for Part A of Type 1 matrix (Figure 5-3) and Part B (Figure 5-4).

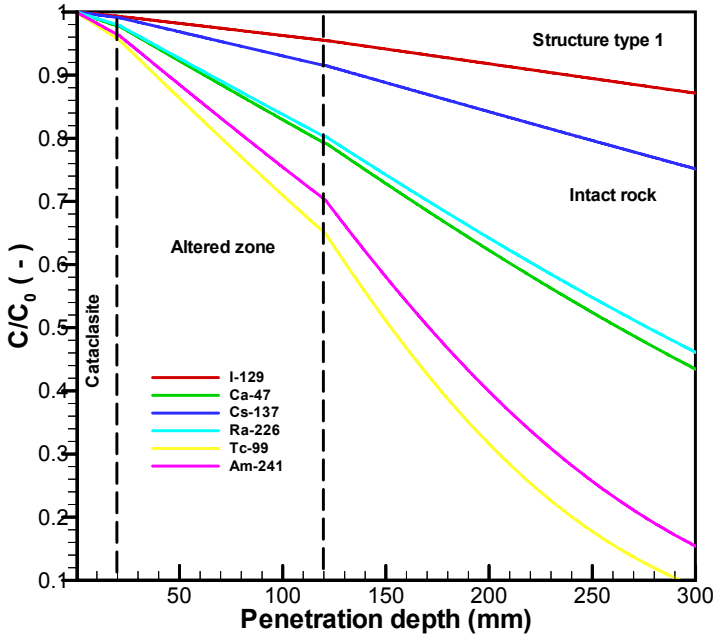

Figure 5-3. *Penetration profile for Part A of the matrix in structure Type 1. The profiles are calculated at the times of 85% mass recovery. The times are 936y for I-129, 3969y for Ca-47, 7.82E+5y for Ra-226, 2.05E+6y for Cs-137, 4.88E+6y for Tc-99 and 1.45E07 for Am-241.*

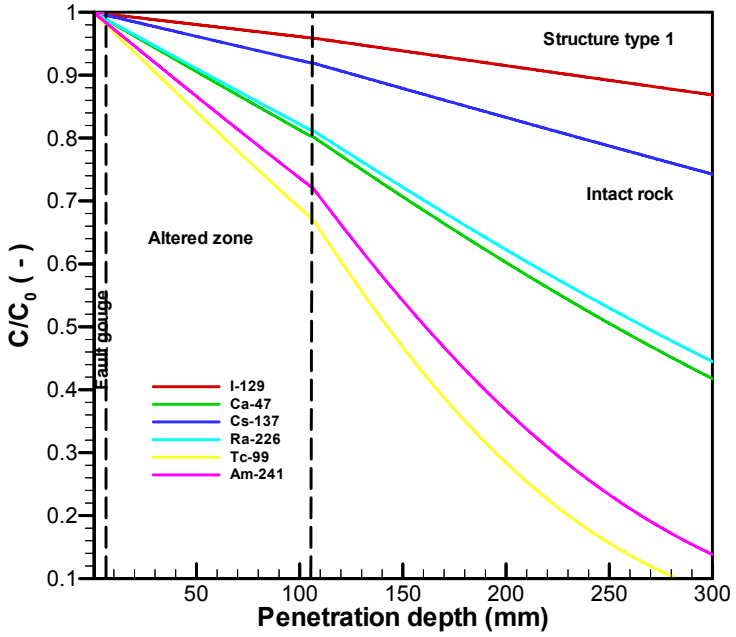

Figure 5-4. *Penetration profile for Part B of the matrix in structure Type 1. The profiles are calculated at the times of 85% mass recovery. The times are 936y for I-129, 3969y for Ca-47, 7.82E+5y for Ra-226, 2.05E+6y for Cs-137, 4.88E+6y for Tc-99 and 1.45E07 for Am-241.*

If C/C_0 = 15% is chosen as a limit of penetration, we obtain the penetration depths for both parts of the rock matrix in structure Type 1 as well as in structure Type 2 that are shown in Table 5-6.

Table 5-6. Penetration depths at 15% relative concentration of different tracers in structure Type 2 and the effective porosities based on the depths.

Tracer	Type 2		Type 1 (Part A)		Type 1 (Part B)		Effective $\theta_{e,t}$ (%)
	Depth (mm)	θ_e (%)	Depth (mm)	θ_e (%)	Depth (mm)	θ_e (%)	
I-129	2453	0.31	2466	0.32	2465	0.35	0.31
Ca-47	507	0.33	522	0.38	518	0.54	0.35
Ra-226	538	0.33	553	0.38	549	0.53	0.35
Cs-137	1237	0.31	1251	0.34	1248	0.40	0.32
Tc-99	230	0.37	258	0.47	253	0.79	0.41
Am-241	269	0.36	297	0.45	292	0.72	0.40

From Table 5-6 we find that the penetration depths of the tracers vary. The strongly sorbing tracers (e.g., Tc-99 and Am-241) have shorter penetration depths, while the conservative tracers diffuse deeper into the rock matrix. For the structure Type 2, all tracers penetrate deeply into the intact rock, with the conservative tracer having the deepest penetration depth. For both part of the rock matrix in structure Type 1, all tracers have passed through the cataclasite zone, or the fault gouge zone and altered zone, and diffuse further into the intact tock.

We calculate the effective parameters in the same way as for Task 6D penetration analysis, while we further account for the complexity factor. As shown in Table 5-4, there are 17.2% of Type 1 structure and 82.8% of Type 2 structure for the flow paths at x = 1920 m. So an effective porosity for I-129 by accounting for the complexity factor, for example, in the entire rock matrix would be

$$\theta_{e,t} = 0.31 \times 0.828 + \frac{0.32 + 0.35}{2} \times 0.172 = 0.31$$

The effective porosities thus calculated for the entire rock matrix for all the tracers are summarized in the last column of Table 5-6.

The sorption distribution coefficient K_d is also calculated by the same weighing method. The calculated effective K_d values for the entire rock matrix are presented in Table 5-7.

Table 5-7. Penetration depths and effective K_d values.

Tracer	Type 2		Type 1 (Cat.+Alt)		Type 1 (Goug.+ Alt.)		Effective $K_{d,t}$ (m^3/kg)
	Depth (mm)	K_d (m^3/kg)	Depth (mm)	K_d (m^3/kg)	Depth (mm)	K_d (m^3/kg)	
I-129	2453	0	2466	0	2465	0	0
Ca-47	507	4.83e-5	522	5.33E-5	518	5.77e-5	4.93e-5
Ra-226	538	9.66e-3	553	1.06e-2	549	1.14e-2	9.84e-3
Cs-137	1237	1.04e-2	1251	1.09e-2	1248	1.13e-2	1.05e-2
Tc-99	230	0.2	258	0.2	253	0.2	0.2
Am-241	269	0.5	297	0.5	292	0.5	0.5

We have obtained the effective porosities, θ, and the effective K_d values for all tracers, Table 5-8 presents the values of κ and K_a calculated by using the effective values of θ and K_d in Table 5-6 and Table 5-7. The values shown in Table 5-8 will be used later in calculating the BTCs at x = 1920 m.

Table 5-8. Summary of effective sorption and diffusion parameters at x = 1920 m based on penetration depths.

Tracer	θ (%)	F (-)	D_w (m^2/h)	K_d (m^3/kg)	K_a (m)	κ (m $y^{-1/2}$)
I-129	0.31	7.7E-5	7.20E-6	0	0	1.23E-4
Ca-47	0.35	9.4E-4	2.85E-6	4.93e-5	3.2E-4	5.65E-4
Ra-226	0.35	9.4E-4	3.20E-6	9.84e-3	6.0E-2	8.16E-3
Cs-137	0.32	8.1E-5	7.45E-6	1.05e-2	6.8E-2	1.23E-2
Tc-99	0.41	1.2E-4	1.8E-6	0.2	0.26	3.20E-2
Am-241	0.40	1.2E-5	2.14E-6	0.5	0.65	5.41E-2

ρ=2700kg/m^3

At x = 1880 m and x = 1800 m

From the calculation results at x = 1920 m it can be seen that the tracers penetrate deeply into the intact rock. For x = 1880 m, the mean travel time for the advection only is increased to $<\tau>$=3.65 y from $<\tau>$=1.44 y at x = 1920 m (Table 3-8). For x = 1800 m, there is an even longer travel time $<\tau>$=6.01 y. The calculation of the penetration profiles for x = 1880 m and x = 1800 m show that the effective parameters (θ and K_d) are essentially the same in values as the parameters for the intact rock. Table 5-9 lists the values of κ and K_a for the intact rock. The values shown in Table 5-9 will be used later in calculating the BTCs at x = 1880 m and x = 1800 m.

Table 5-9. Summary of effective sorption and diffusion parameters at *x* = 1880 m and *x* = 1800 m (from intact rock).

Tracer	θ (%)	F (-)	D_w (m^2/h)	K_d (m^3/kg)	K_a (m)	κ (m $y^{-1/2}$)
I-129	0.3	7.7E-5	7.20E-6	0	0	1.18E-4
Ca-47	0.3	7.7E-5	2.85E-6	4.4e-5	3.2E-4	4.72E-4
Ra-226	0.3	7.7E-5	3.20E-6	8.8e-3	6.0E-2	6.99E-3
Cs-137	0.3	7.7E-5	7.45E-6	1.0e-2	6.8E-2	1.14E-2
Tc-99	0.3	7.7E-5	1.8E-6	0.2	0.26	2.50E-2
Am-241	0.3	7.7E-5	2.14E-6	0.5	0.65	4.31E-2

ρ=2700kg/m^3

5.4 Results

5.4.1 Flow

Description of flow paths

At *x* = 1920 m

For the calculations of the flow paths, all structures including the background structures have been taken into account in our modelling. There are totally 1498 particles evenly distributed in the injection section and they are released into the flow field for particle tracking. The particle trajectories follow two main flow paths (Figure 5-5). The first path runs through a network of four structures, i.e., structures 23D → 1925B → 21D → 20D. The second path is in three deterministic structures 23D→22D→20D.

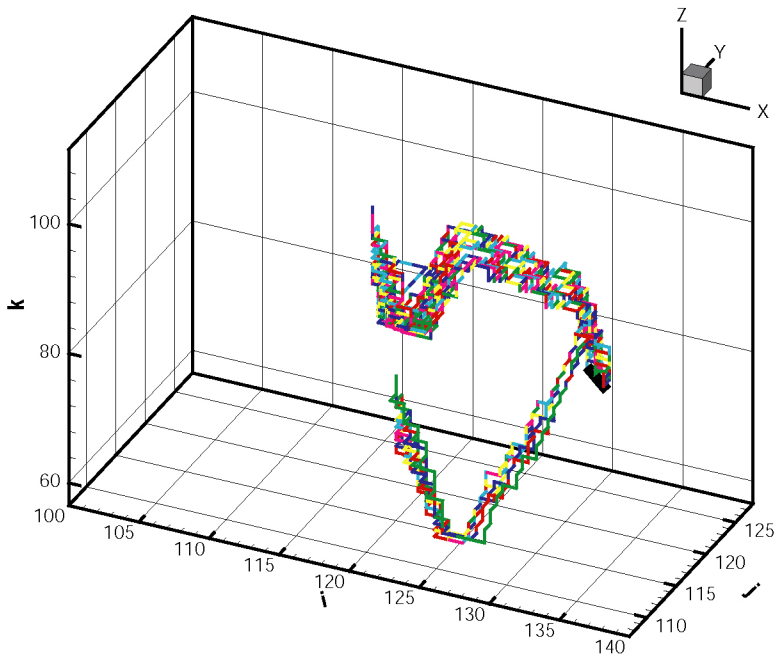

Figure 5-5. *Visualization of flow paths at x = 1920 m.*

At x = 1880 m

The flow paths at the CP of x = 1880 m are shown in Figure 5-6. The paths extend further to the west from x = 1920 m. The paths first converge into one main path and then spread out again.

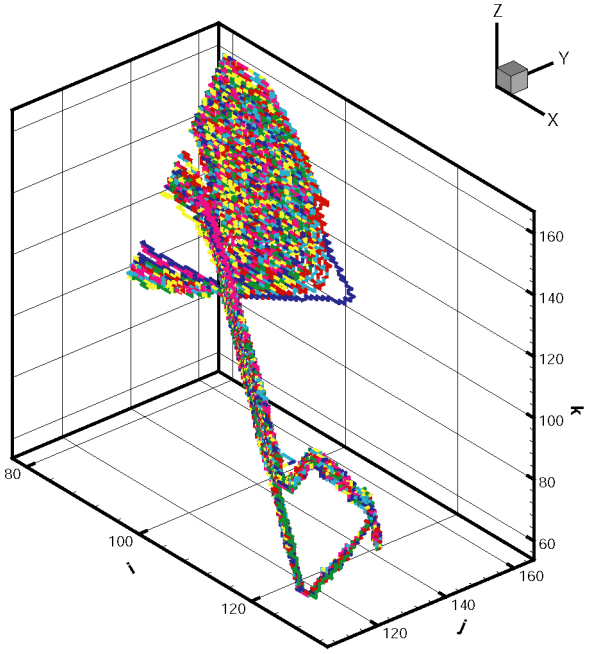

Figure 5-6. *Visualization of flow paths at x = 1880 m.*

At the west boundary (x = 1800 m)

The paths extend from the paths at x = 1880 m to the west boundary (Figure 5-7) and further spread out.

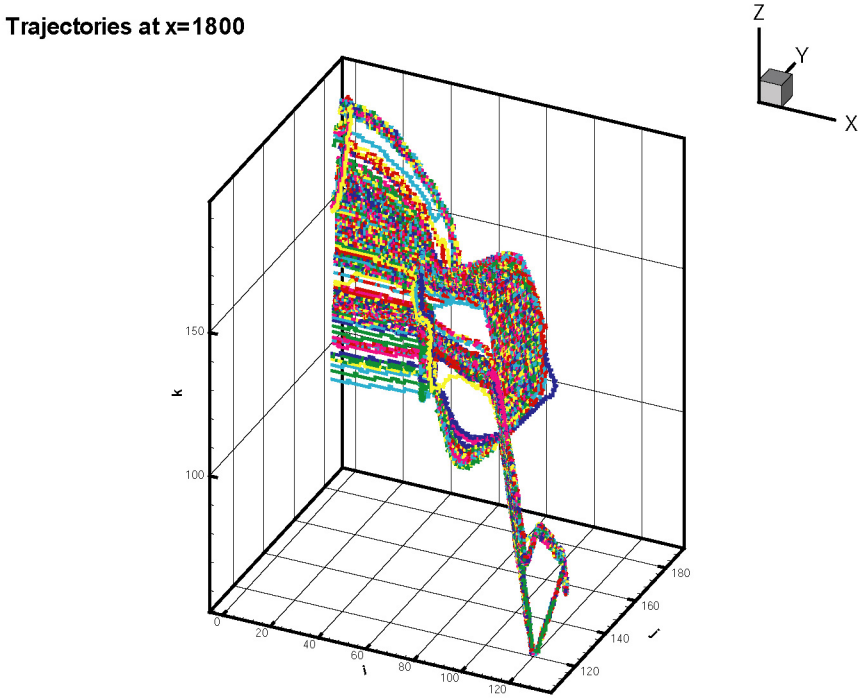

Figure 5-7. *Visualization of flow paths at x = 1800 m.*

Water residence time distribution

The CDFs of the water residence time are presented in Figure 5-8 for x = 1920 m, in Figure 5-9 for x = 1880 m and in Figure 5-10 for x = 1800 m, respectively. The simulated distributions of water residence time have approximately a shape of inverse-Gaussian. The means and variances of the water residence time are shown in Table 3-8.

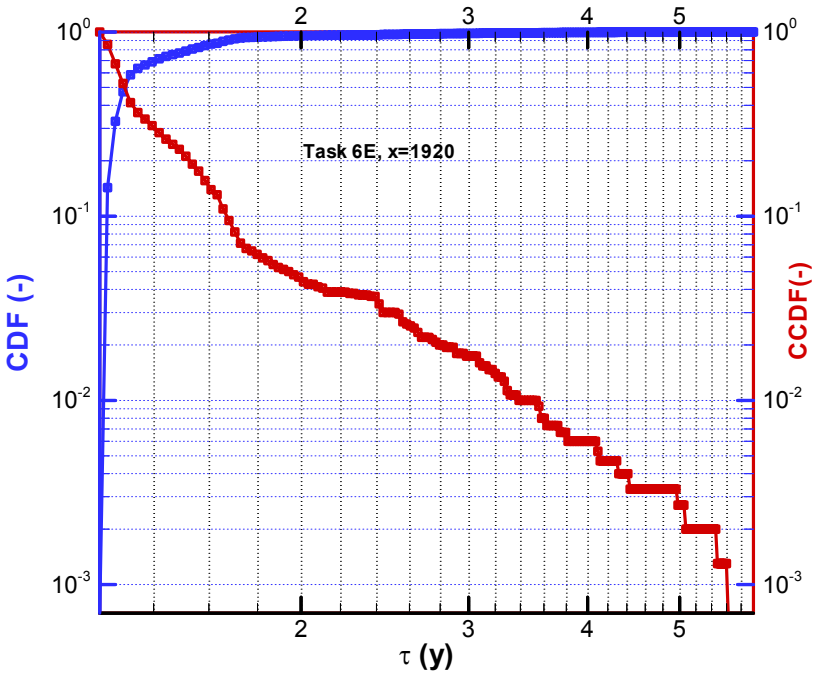

Figure 5-8. *Cumulative distribution function (CDF) and complementary Cumulative distribution function (CCDF) of the water residence time at x =1920 m.*

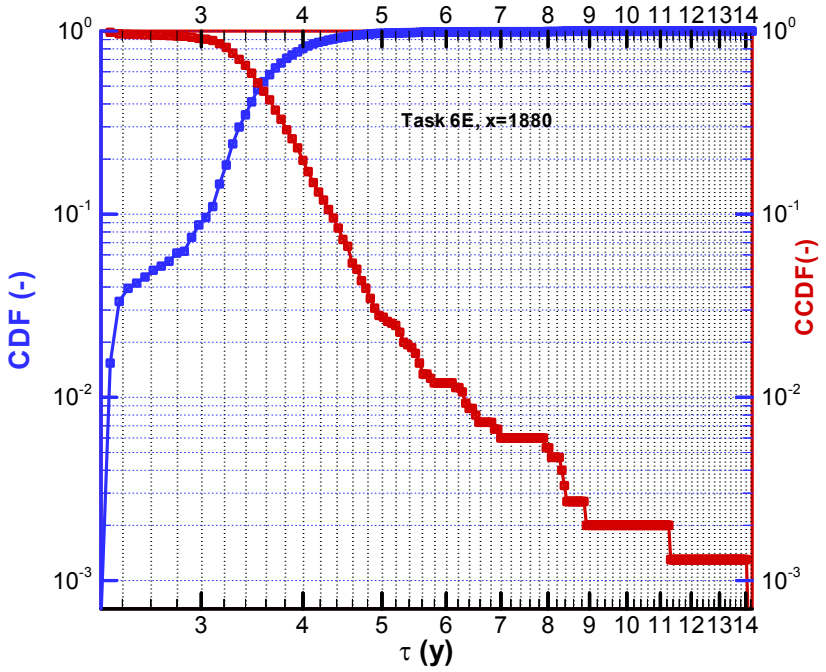

Figure 5-9. *Cumulative distribution function (CDF) and complementary Cumulative distribution function (CCDF) of the water residence time at x = 1880 m.*

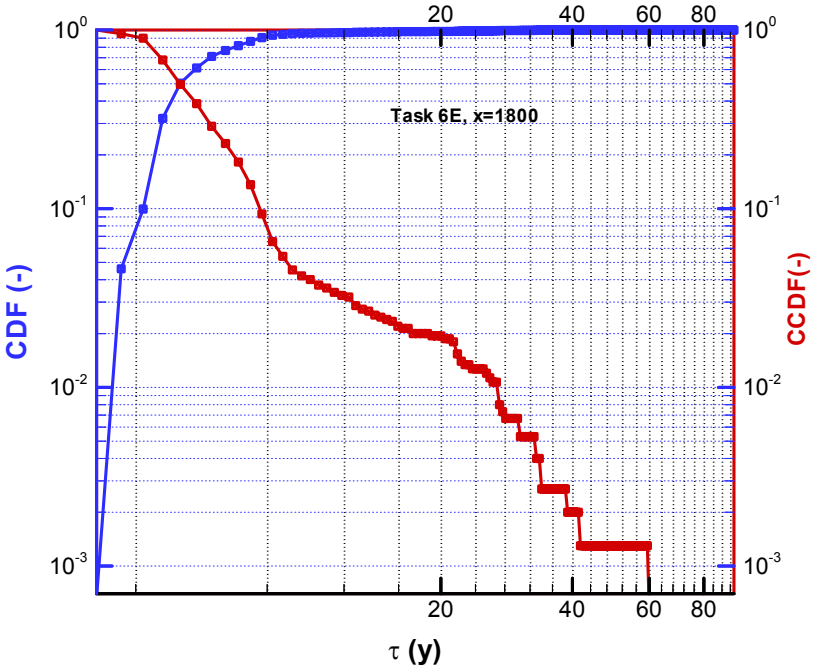

Figure 5-10. *Cumulative distribution function (CDF) and complementary Cumulative distribution function (CCDF) of the water residence time at x = 1800 m.*

5.4.2 Transport

β-parameter

The CDFs of the β parameter are presented in Figure 5-11 for x = 1920 m, in Figure 5-12 for x = 1880 m and in Figure 5-13 for x = 1800 m. The distribution of β has approximately a shape of the inverse-Gaussian distribution. The distribution data are not directly used in the calculation of the BTCs. We have assumed that β has a linear relation with τ. Table 3-8 shows the means and variances of the parameter β.

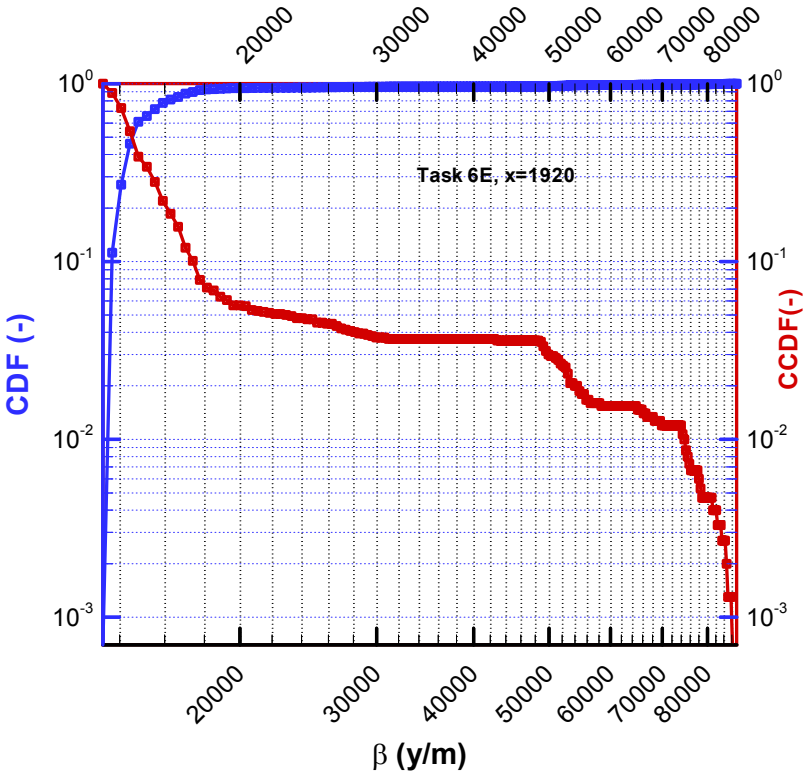

Figure 5-11. *Cumulative distribution function (CDF) and complementary Cumulative distribution function (CCDF) of the β parameter at x = 1920 m.*

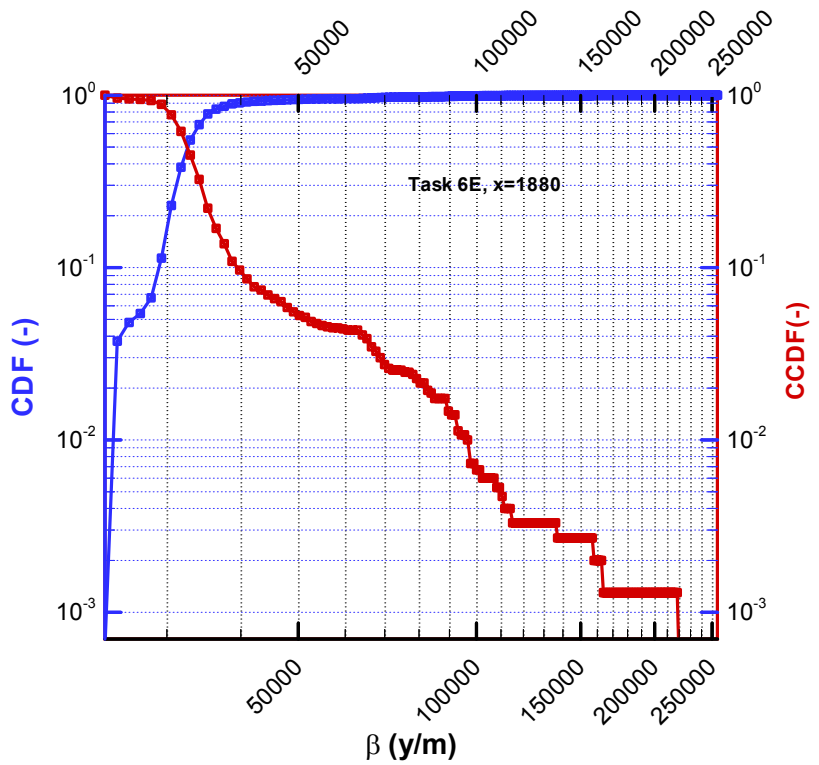

Figure 5-12. *Cumulative distribution function (CDF) and complementary Cumulative distribution function (CCDF) of the β parameter at x = 1880 m.*

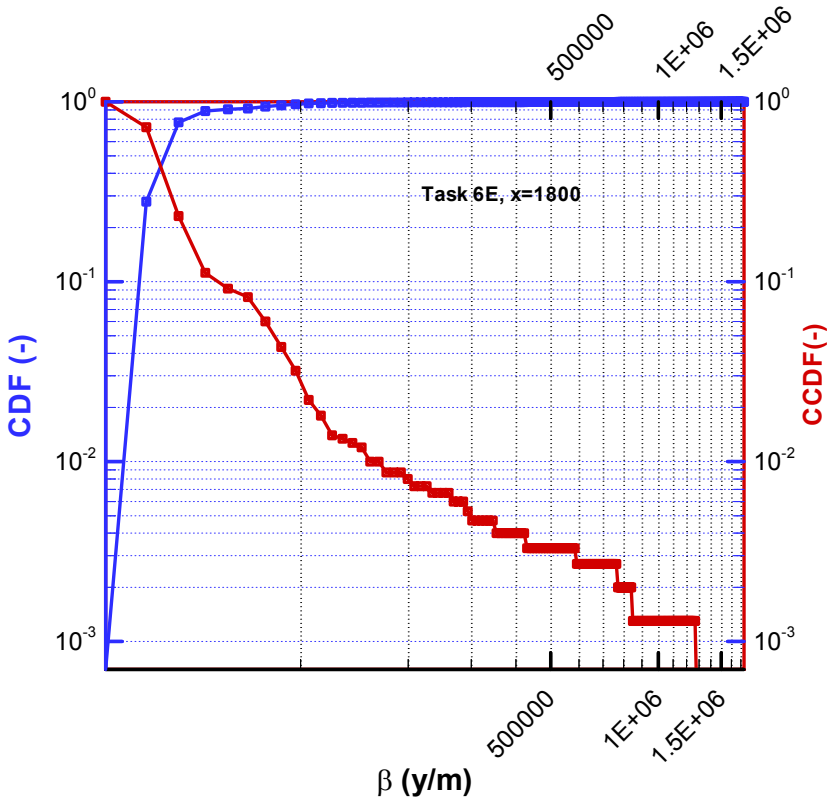

Figure 5-13. *Cumulative distribution function (CDF) and complementary Cumulative distribution function (CCDF) of the β parameter at x = 1800 m.*

Breakthrough time history for the tracers

The results of the calculated BTCs using the parameters summarized in Table 5-8 for the extended pulse injection are presented in Figure 5-14 for x = 1920 m. The calculated BTCs using the parameters given in Table 5-9 for the extended pulse injection are presented in Figure 5-15 for x = 1880 m and in Figure 5-16 for x = 1800 m. The moments of water residence time are the values of the ensemble mean and the variance obtained from the particle tracking simulations of 1498 trajectories from the relevant control planes (Table 3-8). The values of K_a were calculated from the values of K_d of the fracture coatings (Table 3-11).

Tracer I-129 is a conservative tracer. The BTC of I-129 has therefore the highest peak and arrives at the earliest time.

Tracer Ca-47 is a weakly sorbing tracer. The BTC of Ca-47 is shifted to the right and lower compared to that of I-129.

Tracers Cs-137 and Ra-229 are more strongly sorptive tracers. They have the longer retention times compared to the conservative and weakly sorbing tracers. Tracer Ra-226 is generally less sorptive than Cs-137. So the simulated BTC for Ra-226 is higher and shifted to the left compared with that of Cs-137. Ra-226 thus has a shorter retention time than Cs-137.

Tracers Tc-99 and Am-241 are the strongest sorbing tracers. Therefore they have the longest retention times as shown in Figure 4-4.

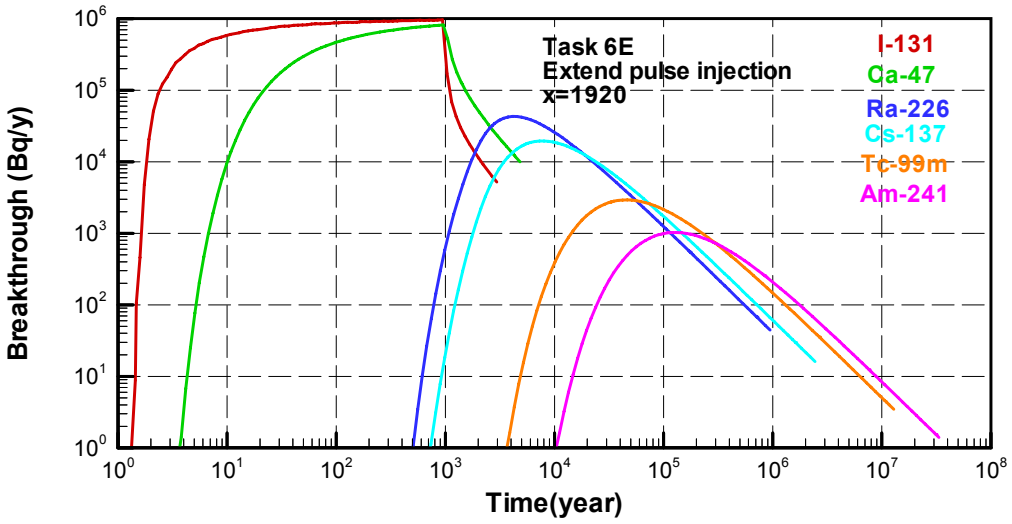

Figure 5-14. *Calculated BTCs for extended pulse injection at x = 1920 m. The red line is for I-129, green line for Ca-47, blue for Ra-226, cyan for Cs-137, orange for Tc-99 and purple for Am-241.*

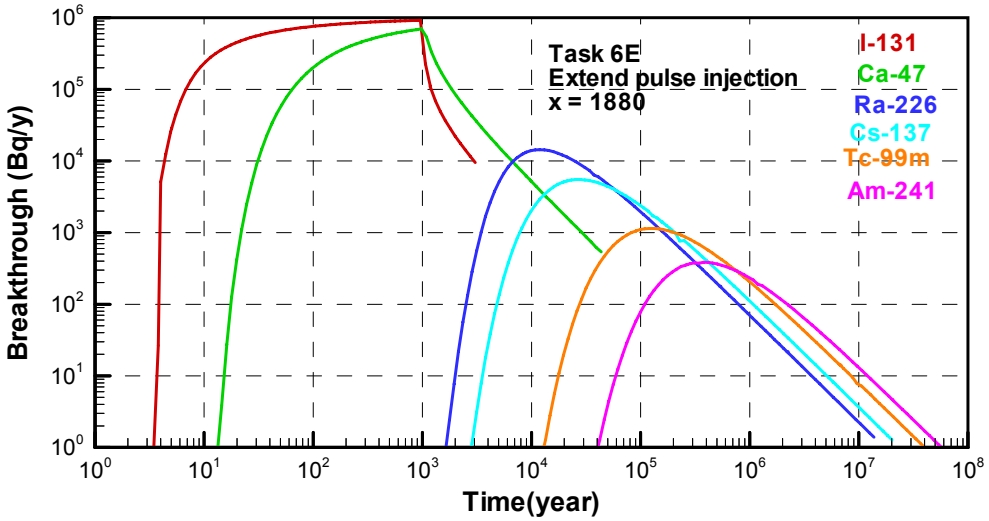

Figure 5-15. *Calculated BTCs for extended pulse injection at x=1880 m. The red line is for I-129, green line for Ca-47, blue for Ra-226, cyan for Cs-137, orange for Tc-99 and purple for Am-241.*

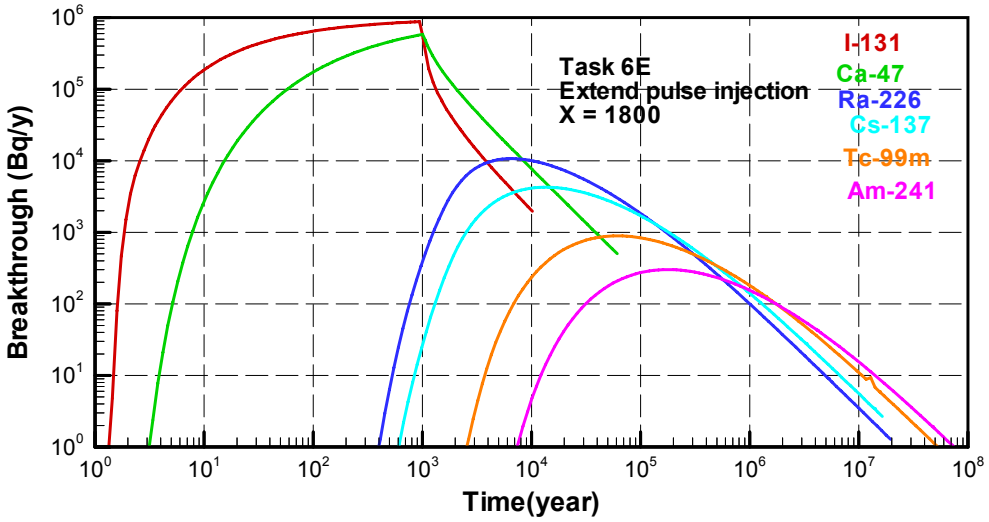

Figure 5-16. *Calculated BTCs for extended pulse injection at x = 1800 m. The red line is for I-129, green line for Ca-47, blue for Ra-226, cyan for Cs-137, orange for Tc-99 and purple for Am-241.*

The times for 5%, 50% and 95% mass recovery are given in Table 5-10 for x = 1920 m, in Table 5-11 for x = 1880 m and in Table 5-12 for x = 1800 m (the west boundary).

Table 5-10. Times for 5%, 50% and 95% mass recovery of the injected mass at x = 1920 m for the extended pulse injection.

Tracer	T_5 (y)	T_{50} (y)	T_{95} (y)
I-129	64.0	509.3	938.1
Ca-47	135.5	707.2	4260
Ra-226	3180	20580	715400
Cs-137	5715	44940	1.626E+6
Tc-99	33240	298100	1.1E+7
Am-241	92860	849500	3.142E+7

Table 5-11. Times for 5%, 50% and 95% mass recovery of the injected mass at x = 1880 m for the extended pulse injection.

Tracer	T_5 (y)	T_{50} (y)	T_{95} (y)
I-129	82.1	555.1	1179
Ca-47	213.8	894.1	9752
Ra-226	8794	61400	2.2E+6
Cs-137	19760	158500	6.115E+6
Tc-99	91500	758300	2.784E+7
Am-241	267100	2.261E+6	8.403E+7

Table 5-12. Times for 5%, 50% and 95% mass recovery of the injected mass at x = 1800 m for the extended pulse injection.

Tracer	T_5 (y)	T_{50} (y)	T_{95} (y)
I-129	96.87	612.6	2317
Ca-47	236.9	1068	21500
Ra-226	6639	112400	5249000
Cs-137	14840	292200	1.39E+7
Tc-99	68290	1404000	6.444E+7
Am-241	199400	4169000	>1e+8

Breakthrough curves for the Dirac pulse injection

The calculated BTCs for the Dirac pulse injection are shown in Figure 5-17 for x =1920 m, in Figure 5-18 for x = 1880 m and in Figure 5-19 for x = 1800 m. The curves clearly have the similar shapes and trends as the simulated BTCs for the extended pulse injection (shown in Figures 5-14 to 5-16).

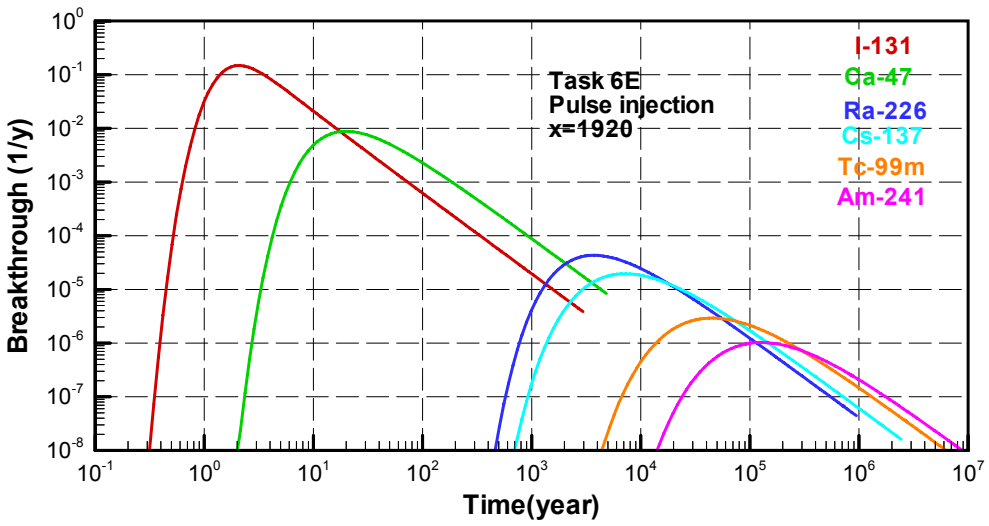

Figure 5-17. *Calculated BTCs for the Dirac pulse injection at x = 1920 m.*

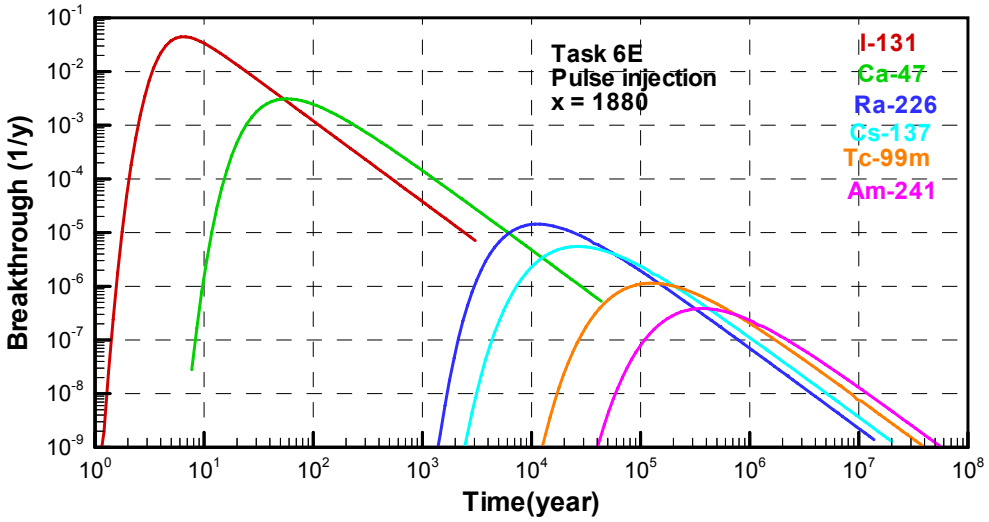

Figure 5-18. *Calculated BTCs for the Dirac pulse injection at x = 1880 m.*

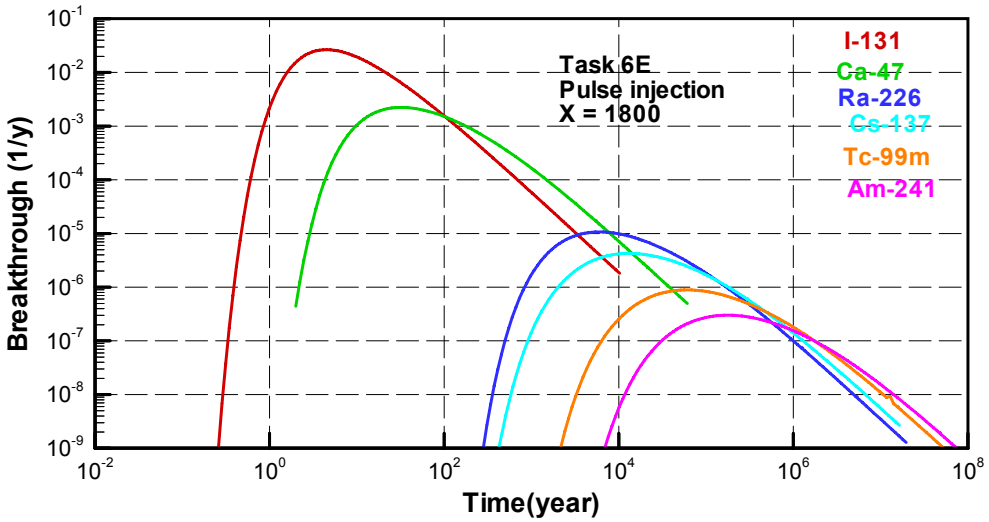

Figure 5-19. *Calculated BTCs for the Dirac pulse injection at x = 1800 m.*

The times of 5%, 50% and 95% mass recovery for the Dirac pulse injection are presented in Table 5-13 for x = 1920 m, in Table 5-14 for x = 1880 m and in Table 5-15 for x = 1800 m. These times are quite close to the times for the extended pulse injection given in Tables 5-10 to 5-12. However, apparent deviations of the arriving times for the conservative and weakly sorbing tracers are observed.

Table 5-13. Times for 5%, 50% and 95% mass recovery of the injected mass at x = 1920 m for the Dirac pulse injection.

Tracer	T_5 (y)	T_{50} (y)	T_{95} (y)
I-129	1.473	5.8	163.9
Ca-47	14.5	98.4	3436
Ra-226	2709	20110	715400
Cs-137	5240	44440	1.624E+6
Tc-99	32760	297700	1.1E+7
Am-241	92380	849000	3.141E+7

Table 5-14. Times for 5%, 50% and 95% mass recovery of the injected mass at x = 1880 m for the Dirac pulse injection.

Tracer	T_5 (y)	T_{50} (y)	T_{95} (y)
I-129	5.0	20.7	692.3
Ca-47	42.1	277.4	8896
Ra-226	8317	60900	2.2E+6
Cs-137	19290	158000	5.796E+6
Tc-99	91030	757600	2.779E+7
Am-241	266600	2.256E+6	8.334E+7

Table 5-15. Times for 5%, 50% and 95% mass recovery of the injected mass at *x* = 1800 m for the Dirac pulse injection.

Tracer	T_5 (y)	T_{50} (y)	T_{95} (y)
I-129	3.554	36.58	1497
Ca-47	31.07	510.1	21700
Ra-226	6160	112000	5249000
Cs-137	14360	291700	1.39E+7
Tc-99	67810	1404000	6.444E+7
Am-241	198900	4169000	>1e+8

Maximum release rate

Table 5-16 shows the maximum release rates of all tracers for the extended pulse injection. Table 5-17 shows the same rates for the Dirac pulse injection.

Table 5-16. Maximum release rates for the extended pulse injection (Bq/y).

Tracer	at x = 1920 m	at x = 1880 m	at x = 1800 m
I-129	963100	922500	878500
Ca-47	817400	698400	582900
Ra-226	43040	14400	10720
Cs-137	19560	5512	4266
Tc-99	2933	1144	892.2
Am-241	1026	385.7	301.7

Table 5-17. Maximum release rates for the Dirac pulse injection (1/y).

Tracer	at x = 1920 m	at x = 1880 m	at x = 1800 m
I-129	0.1486	0.04456	0.02664
Ca-47	0.008824	0.003114	0.002238
Ra-226	4.329E-5	1.438E-5	1.072E-5
Cs-137	1.96E-5	5.512E-6	4.27E-6
Tc-99	2.931E-6	1.144E-6	8.911E-7
Am-241	1.027E-6	3.857E-7	3.017E-7

5.4.3 Sensitivity analysis

6 Task 6F

6.1 Modelling strategy

The structures 1S and 4S are considered to have a Complexity Factor 1, i.e. only contain a single conductive fracture and with the primary geological structure type 100% of the area.

The complexity is not to be addressed in this exercise, i.e. all features are assumed to consist of one single fracture. Furthermore, the fracture is assumed to be homogenous with a constant aperture for both structure 1S and 4S. The case with heterogeneous fractures will be covered as one of the proposed optional tasks, see Task 6F2 Sensitivity analysis.

The boundary conditions are simplified with fixed head boundary conditions at two opposing boundaries of the selected features, while the other sides are treated as no-flow boundaries. The heads are set as to have an estimated groundwater travel time through 20 meter section of the features of 0.1, 1 and 10 years, respectively. The head differences required for this are presented in Table 6-2.

6.2 Model description

6.2.1 Flow model

The properties of the selected features as given in the Task 6C database are presented in Table 6-1. The boundary conditions are presented in Table 6-2.

Table 6-1. Properties of selected structures.

Structure Name	Width & Length	Geological Type	Complexity Factor	Transmissivity (m2/s)	Storativity	Aperture (m)
1S	112.44	1	2*	3.14E-07	2.80E-04	2.58E-04
4S	80.55	2	2*	1.90E-07	2.18E-04	2.01E-04

* For the purpose of this exercise considered to consist of a single fracture, i.e., with a complexity factor of 1 with 100% of the primary streucture.

Table 6-2. Head boundary conditions for different cases.

Case	Travel time (yr)	Head difference (m)	
		1S	4S
A	0.1	0.584	0.539
B	1	0.0584	0.0539
C	10	0.00584	0.00539

We need the first two moments of water residence time distribution from the flow field. As the structures (both 1S and 4S) are assumed to be homogeneous 2D fractures, we then have constant transmissivity (aperture) for both structures. We do not need to conduct numerical simulations for flow and particle tracking. We have constant velocity and straight lines of trajectories (Figure 6-1). The parameter β is related to travel time τ by a linear relationship $\beta=k\tau$. The values of β, τ and k are summarized in Table 6-3 for Structure 1S and Table 6-4 for structure 4S.

Table 6-3. Temporal moments and slope k for Structure 1S.

Case	$\langle\tau\rangle$ (year)	σ_τ (year)	k (m^{-1})
A1	0.1	0	7752
B1	1	0	7752
C1	10	0	7752

Table 6-4. Temporal moments and slope k for Structure 4S.

Case	$\langle\tau\rangle$ (year)	σ_τ (year)	k (m^{-1})
A2	0.1	0	9950
B2	1	0	9950
C2	10	0	9950

6.2.2 Transport model

The tracer source section is assumed to be an intersecting fracture with a linear extension of 3 meters. The source is modelled as several point sources on a line. No simulations are needed for transport modelling as the trajectories are straight lines with constant velocity (Figure 6-1). β and τ have constant values which depend on the boundary conditions for the corresponding cases.

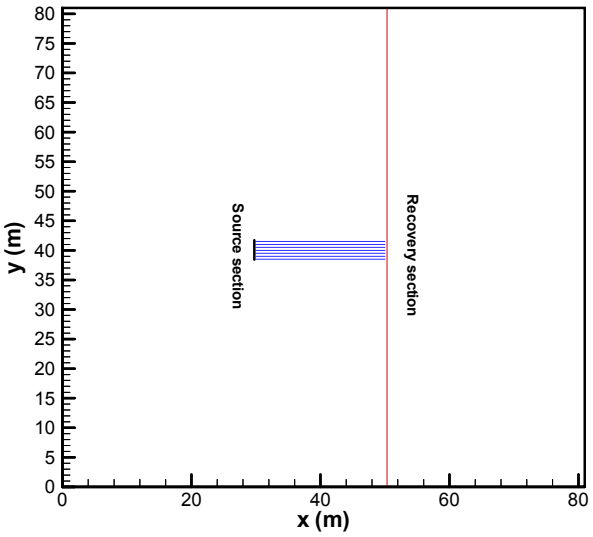

Figure 6-1. *Description of geometry and boundary conditions (Example for structure 4S).*

6.3 Calculated cases

The simulation cases are summarized in Table 6-5.

Table 6-5. Simulation cases for Task 6F.

Travel time (year)	Case for Structure 1S	Case for Structure 4S
0.1	A1	A2
1.0	B1	B2
10	C1	C2

6.4 Effective values of θ and K_d

6.4.1 Structure 1S

We follow the same procedures as for Task 6E to determine the effective values of θ and K_d for the entire rock matrix which are dependent on the penetration depths. We thus need to determine the penetration depths first. We do not repeat the detailed calculation procedure here, as it is already described in Chapter 5.

Table 6-6 summarizes the initial values of K_d and θ for the penetration analysis for Structure 1S.

Table 6-6. Initial values of θ and K_d for Structure 1S.

Case	Initial values of θ and K_d
A1	From altered zone
B1	From altered zone
C1	From intact rock

Using the parameters in Table 6-6 (actual parameter values in Table 6-7), we obtain the times for 85% mass for Cases A1 and B1 in Table 6-7. Using the parameters in Table 6-6 (actual parameter values in Table 6-8), we obtain the times for 85% mass for Case C1 in Table 6-8.

Table 6-7. Initial retention parameters and times of 85% mass recovery for Cases A1 and B1.

Tracer	D_w (m^2/h)	K_d (m^3/kg)	κ (m $y^{-1/2}$)	K_a (m)	T (y) (85%)	
					Case A1	B1
I-129	7.20E-6	0	2.88e-4	0	0.7550	66.54
Cs-137	7.45E-6	2.0E-2	2.78e-2	6.8E-2	6164	6.1E+5
Am-241	2.14E-6	0.5	7.45e-2	0.65	44390	4.3E+5

θ = 0.6%, F = 2.2E-4, ρ=2700kg/m^3

Table 6-8. Initial retention parameters and times of 85% mass recovery for Cases C1 from intact rock.

Tracer	D_w (m^2/h)	K_d (m^3/kg)	κ (m $y^{-1/2}$)	K_a (m)	T (y) (85%)
					Case C1
I-129	7.20E-6	0	1.178e-4	0	1107
Cs-137	7.45E-6	1.0E-2	1.137e-2	6.8E-2	1.02e+7
Am-241	2.14E-6	0.5	4.307e-2	0.65	1.47e+8

Using the parameters in Table 6-7, we obtain the penetration profiles for Case A1 shown in Figure 6-2, and Case B1 in Figure 6-3. The penetration depths for Case A1 in Figure 6-2 are presented in Table 6-9, for Case B1 in Table 6-10. For case C1 using the parameter in Table 6-8, the penetration profiles in Figure 6-4 show that all tracers penetrate deeply into the intact rock (>500 mm, Table 6-11), effective values of K_d and θ are basically equal to the values for intact rock. Table 6-12 summarizes effective values of K_d and θ for three cases in Structure 1S.

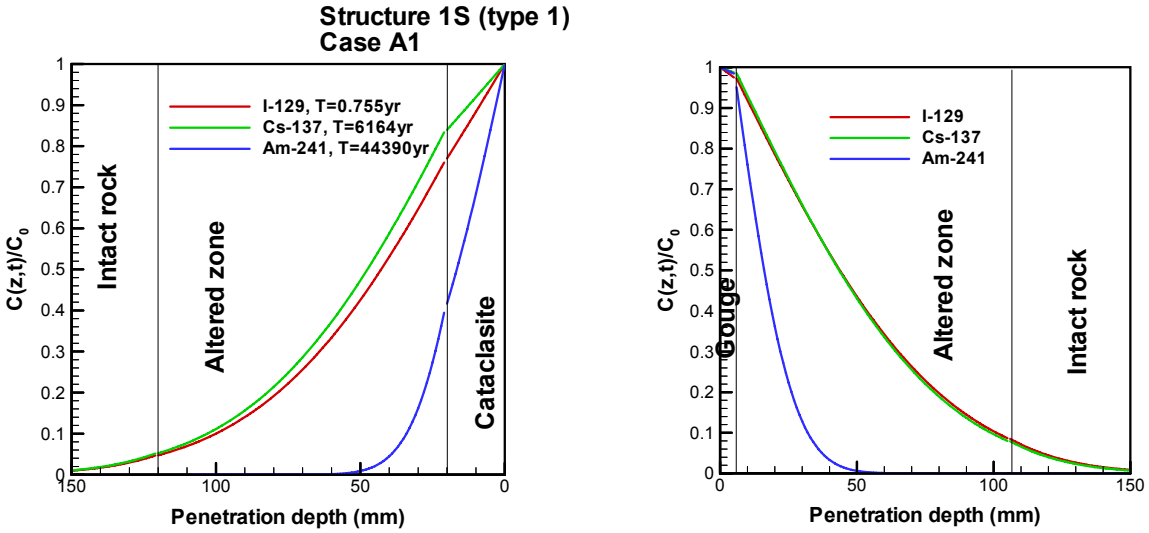

Figure 6-2. *Penetration profiles for Case A1.*

Table 6-9. Penetration depths and effective parameters for Case A1.

Tracer	Type1 (Part A)			Type1 (Part B)			Effective value		
	Depth (mm)	θ(%)	K_d (m^3/kg)	Depth (mm)	θ (%)	K_d (m^3/kg)	θ (%)	K_d (m^3/kg)	κ (m $y^{-1/2}$)
I-129	88	0.691	0	89	1.69	0	1.19	0	6.97e-4
Cs-137	91	0.688	1.89e-2	87	1.715	2.80e-2	1.20	2.35e-2	5.21e-2
Am-241	31	0.858	0.5	29	3.945	0.5	2.4	0.5	2.23e-1

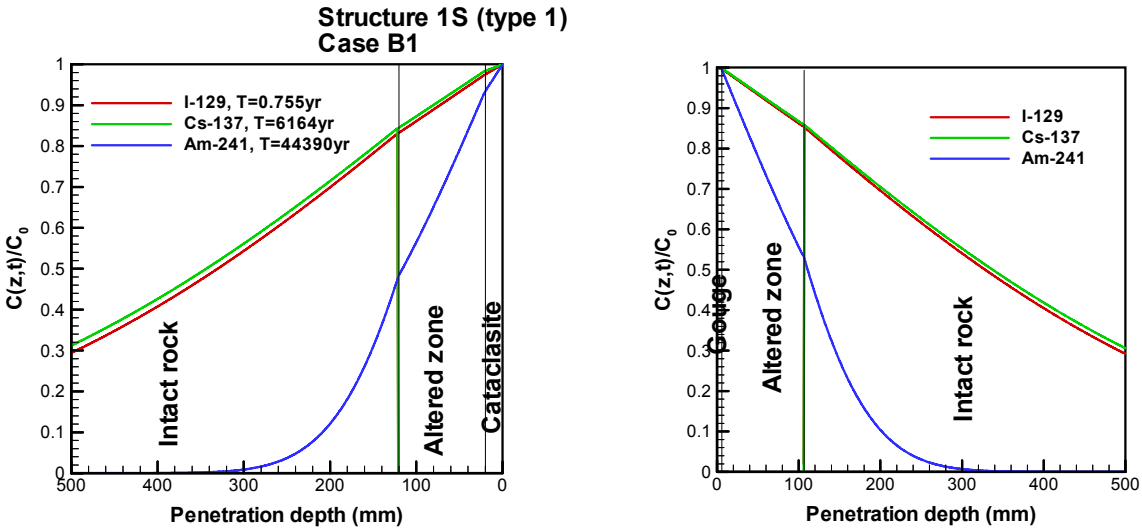

Figure 6-3. *Penetration profiles for Case B1.*

Table 6-10. Penetration depths and effective parameters for Case B1.

Tracer	Type1 (Cat+Alt)			Type1 (Gou+Alt)			Effective value		
	Depth (mm)	θ(%)	K_d (m^3/kg)	Depth (mm)	θ (%)	K_d (m^3/kg)	θ (%)	K_d (m^3/kg)	κ (m $y^{-1/2}$)
I-129	677	0.365	0	675	0.49	0	0.43	0	1.86e-4
Cs-137	699	0.363	1.16e-2	693	0.49	1.25e-2	0.42	1.20e-2	1.64e-2
Am-241	190	0.532	0.5	183	1.0	0.5	0.77	0.5	9.04e-2

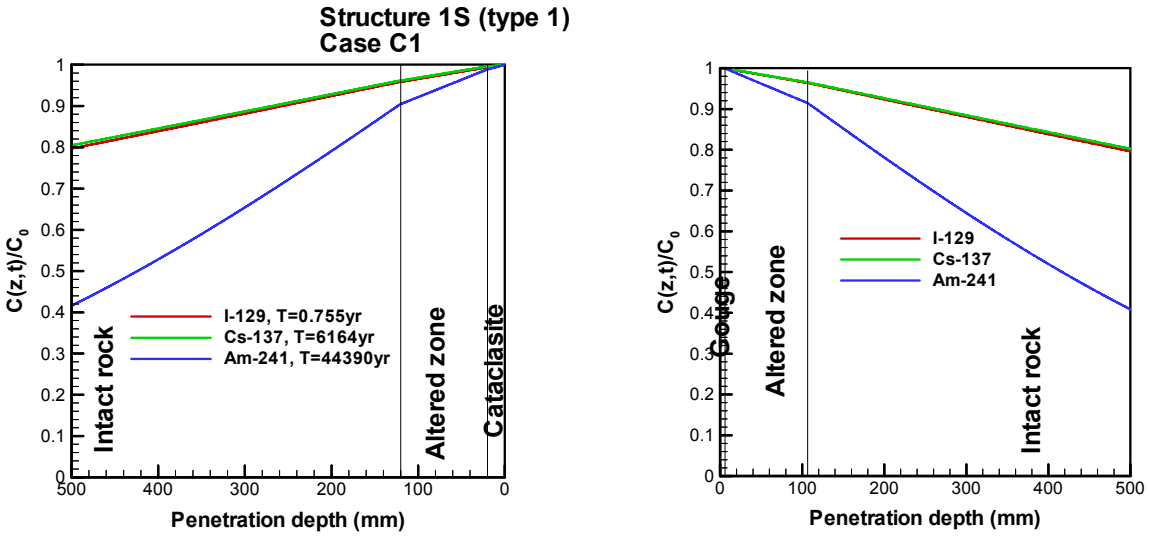

Figure 6-4. *Penetration profiles for Case C1.*

Table 6-11. Penetration depths and effective parameters for Case C1.

Tracer	Type1 (Part A)	Type1 (Part B)	Effective value (Intact rock)		
	Depth (mm)	Depth (mm)	θ (%)	K_d (m^3/kg)	κ (m $y^{-1/2}$)
I-129	>2200	>2200	0.3	0	1.18e-4
Cs-137	>2200	>2200	0.3	1.0e-2	1.14e-2
Am-241	842	836	0.3	0.5	4.31e-2

Table 6-12. Summary of effective retention parameters for Structure 1S.

Tracer	Effective value A1			Effective value B1			Effective value C1		
	θ	K_d (m^3/kg)	κ (my $^{-1/2}$)	θ	K_d (m^3/kg)	κ (m $y^{-1/2}$)	θ	K_d (m^3/kg)	κ (m $y^{-1/2}$)
I-129	1.19	0	6.97e-4	0.43	0	1.86e-4	0.3	0	1.18e-4
Cs-137	1.20	2.35e-2	5.21e-2	0.42	1.20e-2	1.64e-2	0.3	1.0e-2	1.14e-2
Am-241	2.4	0.5	2.23e-1	0.77	0.5	9.04e-2	0.3	0.5	4.31e-2

6.4.2 Structure 4S

Following the same procedure as for Structure 1S, initial values of K_d and θ for Structure 4S for penetration depth calculation are presented in Table 6-13.

Table 6-13. Initial values of θ and K_d for Structure 4S.

Case	Initial values of θ and K_d
A2	From altered zone
B2	From intact rock
C2	From intact rock

Using the parameters in Table 6-13 (actual parameter values in Table 6-14), we obtain the times for 85% mass for Case A2 given in Table 6-15. Using the 85% recovery times in Table 6-15, the penetration profiles for Case A2 are shown in Figure 6-5.

Table 6-14. Initial retention parameters and times of 85% mass recovery for Cases A2 from Altered zone.

Tracer	D_w (m^2/h)	K_d (m^3/kg)	κ (m $y^{-1/2}$)	K_a (m)	T (y) (85%)
					Case A2
I-129	7.20E-6	0	2.88e-4	0	1.179
Cs-137	7.45E-6	2.0E-2	2.78e-2	6.8E-2	1.013e+4
Am-241	2.14E-6	0.5	7.45e-2	0.65	7.29e+4

θ = 0.6%, F = 2.2E-4, ρ=2700kg/m^3

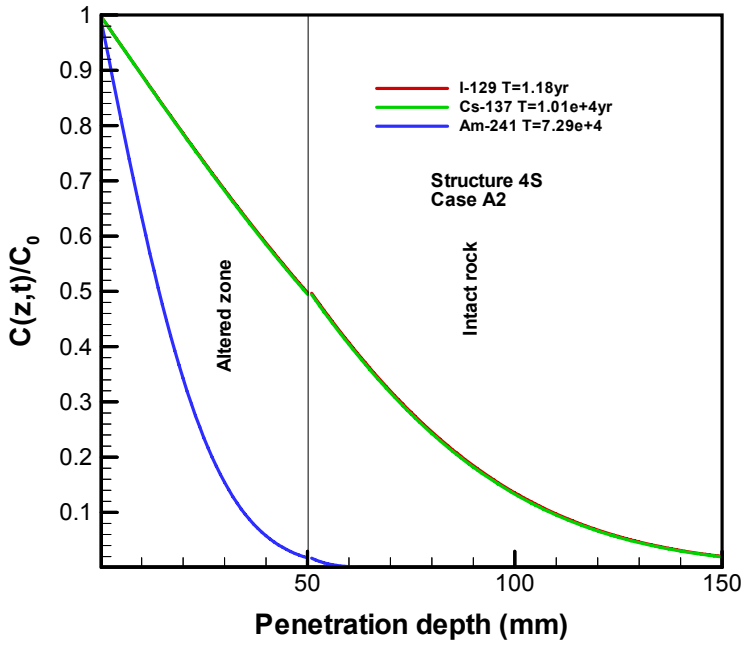

Figure 6-5. *Penetration profile for Case A2.*

The penetration depths for the normalized concentration C/C_0 =0.15 from Figure 6-5 for Case A2 are presented in Table 6-16.

Table 6-15. Penetration depths and effective parameters for Case A2.

Tracer	Type2 (Alt+Intact)	Effective values		
	Depth (mm)	θ(%)	K_d (m^3/kg)	κ ($my^{-1/2}$)
I-129	97	0.45	0	2.01e-4
Cs-137	96	0.46	1.52e-2	1.95e-2
Am-241	30	0.6	0.5	7.45e-2

Using the parameters in Table 6-13 (actual parameter values in Table 6-16), we obtain the times of 85% mass for Case B2 in Table 6-16. Using the 85% recovery times in Table 6-16, the penetration profiles for Case B2 are shown in Figure 6-6. The penetration depths for C/C_0=0.15 from Figure 6-6 and the effective values of K_d and θ thus obtained for Case B2 are presented in Table 6-17.

Table 6-16. Initial retention parameters and times of 85% mass recovery for Cases B2 from Altered zone.

Tracer	D_w (m^2/h)	K_d (m^3/kg)	κ (m $y^{-1/2}$)	K_a (m)	T (y) (85%)
					Case B2
I-129	7.20E-6	0	1.178e-4	0	19.062
Cs-137	7.45E-6	1.0E-2	1.137e-2	6.8E-2	1.69e+5
Am-241	2.14E-6	0.5	4.307e-2	0.65	2.42e+6

θ = 0.3% ρ=2700kg/m^3

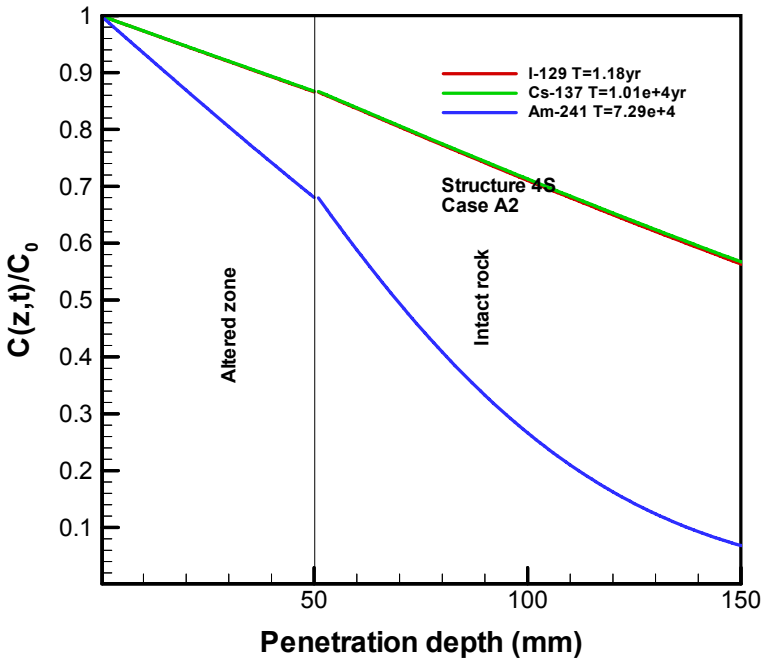

Figure 6-6. *Penetration profiles for Case B2.*

Table 6-17. Penetration depths and effective parameters for Case B2.

Tracer	Type2 (Alt+Intact)			
	Depth (mm)	θ(%)	K_d (m^3/kg)	κ (m $y^{-1/2}$)
I-129	359	0.34	0	1.39e-4
Cs-137	362	0.34	1.14e-2	1.34e-2
Am-241	123	0.42	0.5	5.64e-2

Since the very long time scale for Case C2, the effective values of K_d and θ could be obtained from values for intact rock. Table 6-19 summarizes the effective values of K_d and θ for all three cases for Structure 4S.

Table 6-18. Summary of effective retention parameters for Structure 4S.

Tracer	Effective value A2			Effective value B2			Effective value C2 (from intact rock)		
	θ(%)	K_d (m^3/kg)	κ(m $y^{-1/2}$)	θ(%)	K_d (m^3/kg)	κ (m $y^{-1/2}$)	θ	K_d (m^3/kg)	κ (m $y^{-1/2}$)
I-129	0.45	0	2.01e-4	0.34	0	1.39e-4	0.3	0	1.18e-4
Cs-137	0.46	1.52e-2	1.95e-2	0.34	1.14e-2	1.34e-2	0.3	1.0e-2	1.14e-2
Am-241	0.6	0.5	7.45e-2	0.42	0.5	5.64e-2	0.3	0.5	4.31e-2

6.5 Results

β-parameter

The parameter β has a constant value for each case. The values of β are summarized in Table 6-19.

Table 6-19. β values for all cases in Task 6F.

Case	β (y/m)	Case	β (y/m)
A1	775.2	A2	995
B1	7752	B2	9950
C1	77520	C2	99500

Breakthrough time history for the tracers

Breakthrough curves (BTCs) using the parameter from Table 6-12 for Cases A1, B1, and C1 for Dirac pulse injection are shown in Figure 6-7. BTCs using the parameters from Table 6-18 for Cases A2, B2 and C2 for Dirac pulse injection are shown in Figure 6-8.

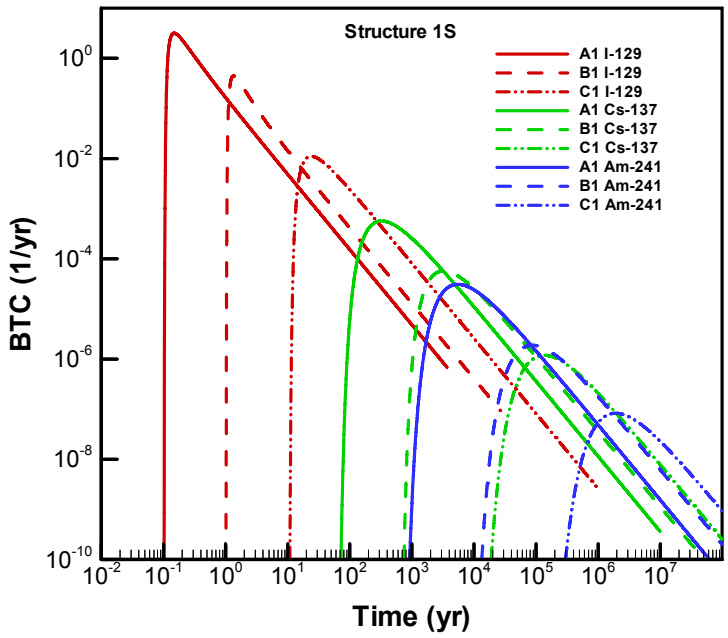

Figure 6-7. *Breakthrough curves for various cases in Structure 1S.*

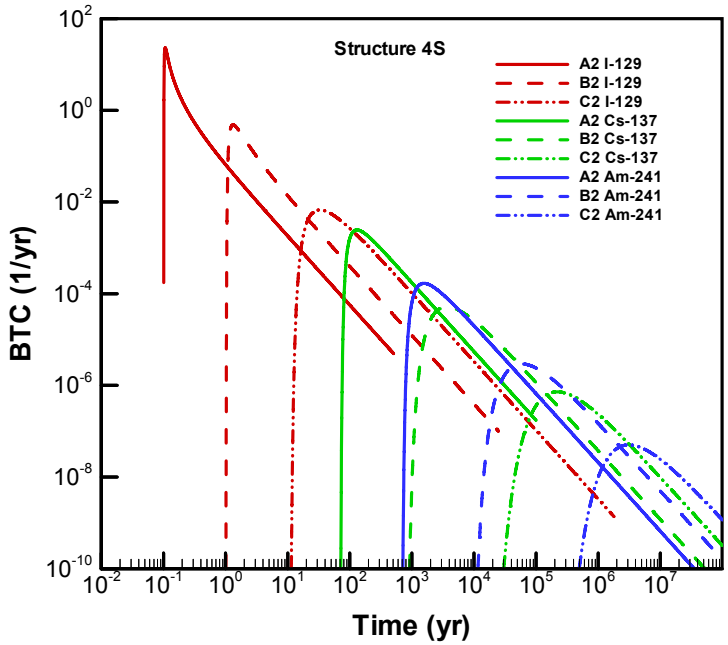

Figure 6-8. *Breakthrough curves for Structure 4S.*

The maximum release rates are summarized in Table 6-20.

Table 6-20. Maximum release rates for Task 6F.

Tracer	Maximum release rate (1/y)					
	Case A1	B1	C1	A2	B2	C2
I-129	3.17	0.44	0.011	23.1	0.48	6.73e-3
Cs-137	5.67e-4	5.72e-5	1.19e-6	2.46e-3	5.20e-5	7.23e-7
Am-241	3.10e-5	1.88e-6	8.30e-8	1.68e-4	2.94e-6	5.04e-8

7 Task 6F2

7.1 Modelling strategy

We consider water flow in a flow path consisting of a series of planar fractures with heterogeneous aperture distributions. The series of fractures consists of three sequentially connected single planar fractures (Figure 1). The three fractures have equal lengths and widths, while each of them have different heterogeneous aperture (or transmissivity) distributions.

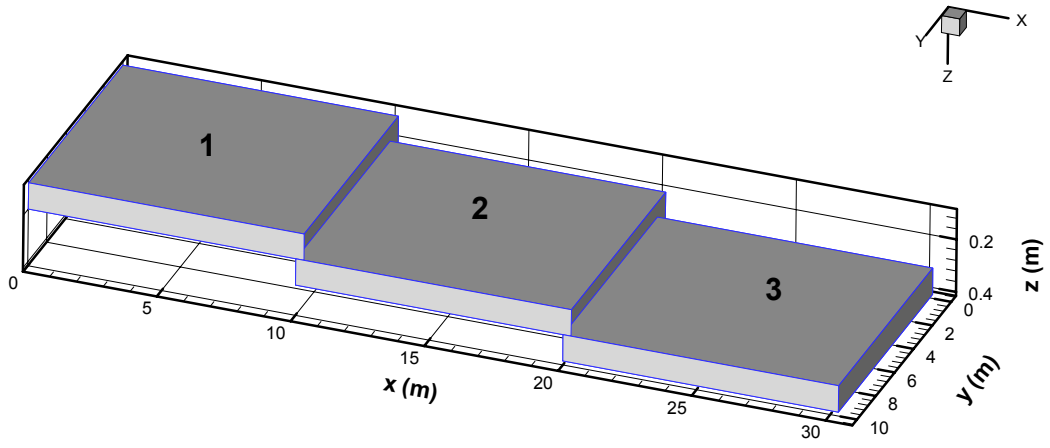

a

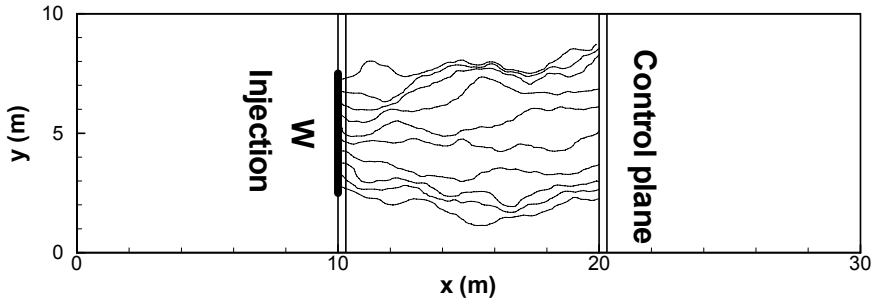

b

Figure 7-1. *(a) Configuration of three connected fractures; (b) a typical realization of trajectories with W = 5.0 m.*

7.2 Model description

For every fracture in a fracture series, the transmissivity $T(\mathbf{x})$ is considered to be a random space function (RSF) and $T(\mathbf{x})$ is assumed to be lognormally distributed with exponential correlation structure:

$$T_i(\mathbf{x}) = T_G^i e^{Y_i(\mathbf{x})} = T_G e^{Z_i} e^{Y_i(\mathbf{x})}$$
$$\mathrm{C_Y}(r) = \sigma_Y^2 e^{-r/I_Y} \qquad (7\text{-}1)$$

where $T_i(\mathbf{x})$ is the ith realization of the transmissivity fields. $Y_i(\mathbf{x})$ is a normally distributed RSF with the mean value and the variances described by $N(0,\sigma_Y^2)$. T_G^i is a random number computed by $T_G e^{Z_i}$, where T_G is the geometric mean for the entire fracture series, and Z_i is a random number characterized by $N(0,\sigma_Z^2)$.

We have two degrees of variability. The first degree of variability is the geometric mean for the ith realization T_G^i, which represents the variability between fractures (global heterogeneity). The second degree of variability is the spatial variability $Y_i(\mathbf{x})$ which represents the variability within a given fracture (internal heterogeneity). $T(\mathbf{x})$ will be determined by the variances of two parameters: σ_Z^2 and σ_Y^2.

Monte-Carlo simulations will be performed on the fracture system shown in Figure 7-1. More information is given in Cheng, (2005).

7.3 Correlation between β and τ

7.3.1 Analytical solution

For an ideal fracture with an uniform aperture, β and τ are related by an analytical expression:

$$\beta = \frac{\tau}{b} \qquad (7\text{-}1)$$

where b is half-aperture. For a heterogeneous fracture, b could be replaced by an effective value b_{eff}.

7.3.2 Calculated cases

The simulation cases are chosen to cover a wide range of two degrees of heterogeneities (global and internal) represented by σ_Z^2 and σ_Y^2. The main features of each simulation case, characterized by the variances σ_Z^2 and σ_Y^2, are summarized in Table 7-1.

Table 7-1. Cases investigated for β and τ correlation.

Case	1	2	3	4	5	6
σ_Z^2	0	0	0.1	0.1	2.0	2.0
σ_Y^2	0.1	2.0	0.1	2.0	0.1	2.0

In the first two cases, Z is kept to be constant (with σ_Z^2 =0). We change the internal heterogeneity from a small value of σ_Y^2=0.1, to a large value of σ_Y^2=2.0. In this way we are able to investigate how the internal heterogeneity alone affects the statistical properties of β and τ. For Cases 3 and 4, we introduce a small global heterogeneity with σ_Z^2=0.1. In cases 5 and 6 the global heterogeneity is further increased to σ_Z^2=2.0, while the internal heterogeneity varies between σ_Y^2=0.1 and σ_Y^2=2.0.

7.4 Results

Scattergrams of β and τ obtained for the cases considered in Table 7-1 are compared in Figure 7-2. To compare the scattergrams of different cases, the six figures in Figure 7-1 have the same axis range for both x- and y-axis.

The parameter β and the travel time τ are well correlated through a power-law relationship $\beta \sim \tau^m$ where m varies between 1.0 to 1.3 for the cases considered in the present study (Figure 7-2, Table 7-2).When the internal heterogeneity of the aperture is the same, the increase of the global heterogeneity will decrease the degree of correlation between β and τ. The increase of the global heterogeneity increases the mean values and variances of both β and τ significantly (Table 7-2). The value of σ_Z^2 is a dominating factor in determining the ensemble mean values of β and τ. For the same global heterogeneity, the increase of the internal heterogeneity will increase the spreading of β for a fixed τ, thus reduce the correlation between β and τ.

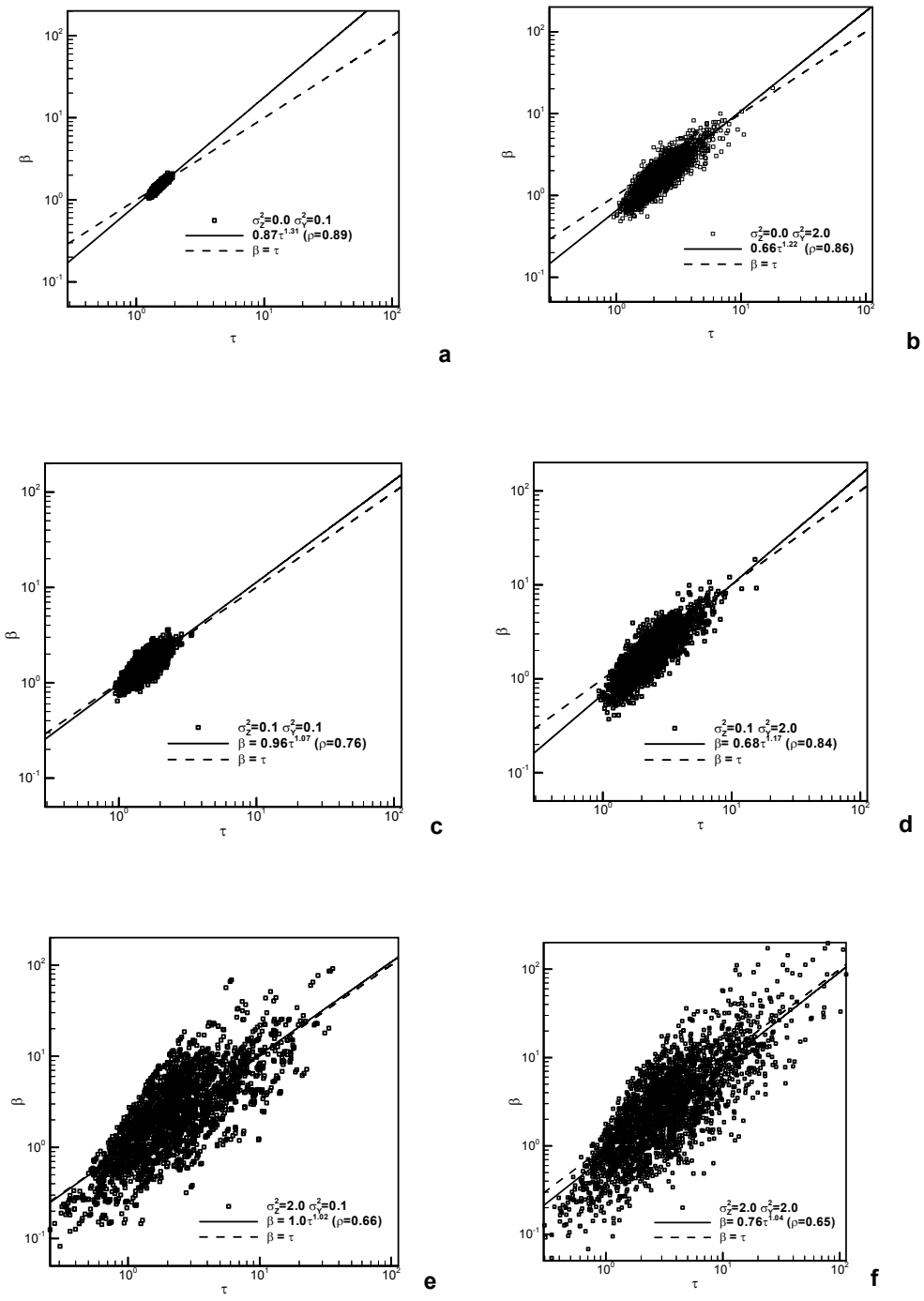

Figure 7-2. *Comparison of simulated β and τ correlation for the cases considered in Table 7-1 and analytical solution (7-1). (a) Case 1; (b) Case 2; (c) Case 3; (d) Case 4; (e) Case 5; (f) Case 6. Solid lines are power-law fits with correlation coefficient in parenthesis. Dashed lines are analytical solution (7-1). Note that β and τ are normalized by β_0 and τ_0 defined in Paper VI in Cheng, (2005).*

Table 7-2. Comparison of statistical moments of normalized β and τ.

Case	σ_Z^2	σ_Y^2	<τ>	σ_τ	<β>	σ_β	ρ(lnβ-lnτ)
1	0	0.1	1.52	0.11	1.51	0.15	0.89
2	0	2.0	2.37	0.97	1.96	1.11	0.86
3	0.1	0.1	1.57	0.30	1.58	0.41	0.76
4	0.1	2.0	2.46	1.15	2.06	1.32	0.84
5	2.0	0.1	3.18	3.52	4.00	6.06	0.66
6	2.0	2.0	5.15	7.38	5.49	11.43	0.65

7.5 Correlation between β and Q

7.5.1 Analytical solution

For a rectangular fracture with a constant aperture, β and Q are related by

$$\beta = \frac{2LW}{Q} \qquad (7\text{-}2)$$

where 2LW is the so-called flow-wetted surface (e.g., Moreno and Neretnieks, 1993) or specific area (Wels et al., 1996). The physical meaning of β is the available flow-wetted surface per unit volume of water flow. Note that Eq. (7-1) is valid for a trajectory, while Eq. (7-2) is valid for a streamtube.

Real fractures in fields are heterogeneous and the aperture variation within and among fractures causes the width of the flow path to fluctuate around W. Different W yields different Q even though Q is constant for a given W in a given realization. Aperture variation between different realizations will also cause Q to vary for a given W.

7.5.2 Simulation cases

The simulation cases are summarized in Table 7-3. For every case in Table 7-3. we have two subcases depending on the width of source section W. The two values of W are chosen as W=5.0 m and W=0.1 m.

Table 7-3. Simulation cases for β and Q correlation.

Case	1	2	3	4
σ_Z^2	0.1	0.1	2.0	2.0
σ_Y^2	0.1	2.0	0.1	2.0

7.5.3 Results

The simulation results are presented in Figure 7-3 for the cases for W=5.0 m, in Figure 7-4 for W=0.1 m.

β and Q are correlated through an inverse power law $\beta \sim Q^{-m}$ where m is between 0.3 to 1.0 for the cases studied in this work. When the internal heterogeneity of the aperture is the same, the increase of the global heterogeneity will increase the degree of correlation between β and Q. The increase of the global heterogeneity increases the mean values and variances of β significantly, while the mean values of Q change moderately.

For the same global heterogeneity, the increase of the internal heterogeneity will increase the spreading of β for a fixed Q, thus reduce the correlation between β and Q. For all levels of internal and global heterogeneities, the β and Q become less strongly correlated as the size of the source section decreases.

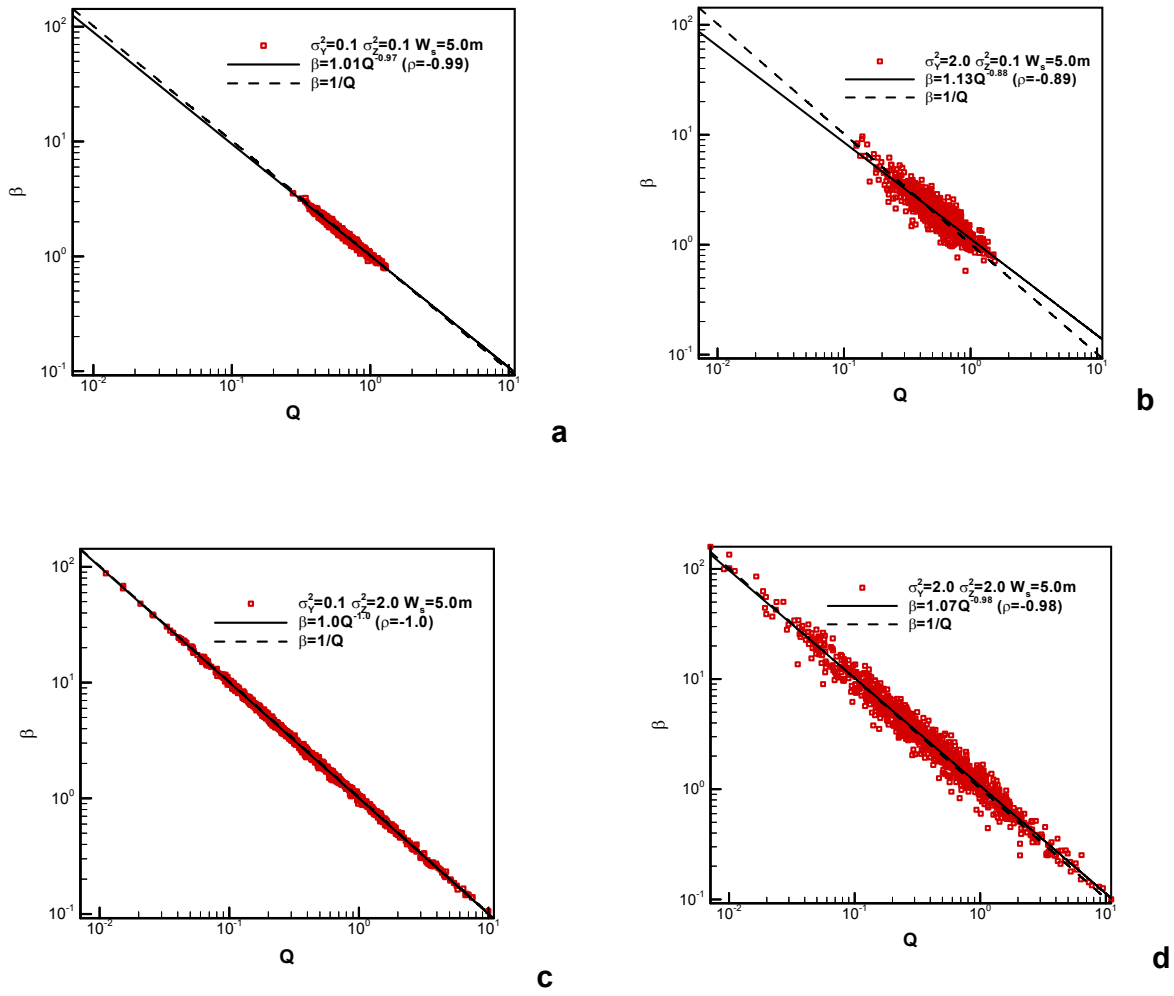

Figure 7-3. *Scattergram of normalized β and Q for the four cases considered in Table 7-3 and for W=5.0 m: (a) Case 1; (b) Case 2; (c) Case 3; and (d) Case 4. Solid lines are the best power-law fits. Dashed lines are analytical solution (7-2).*

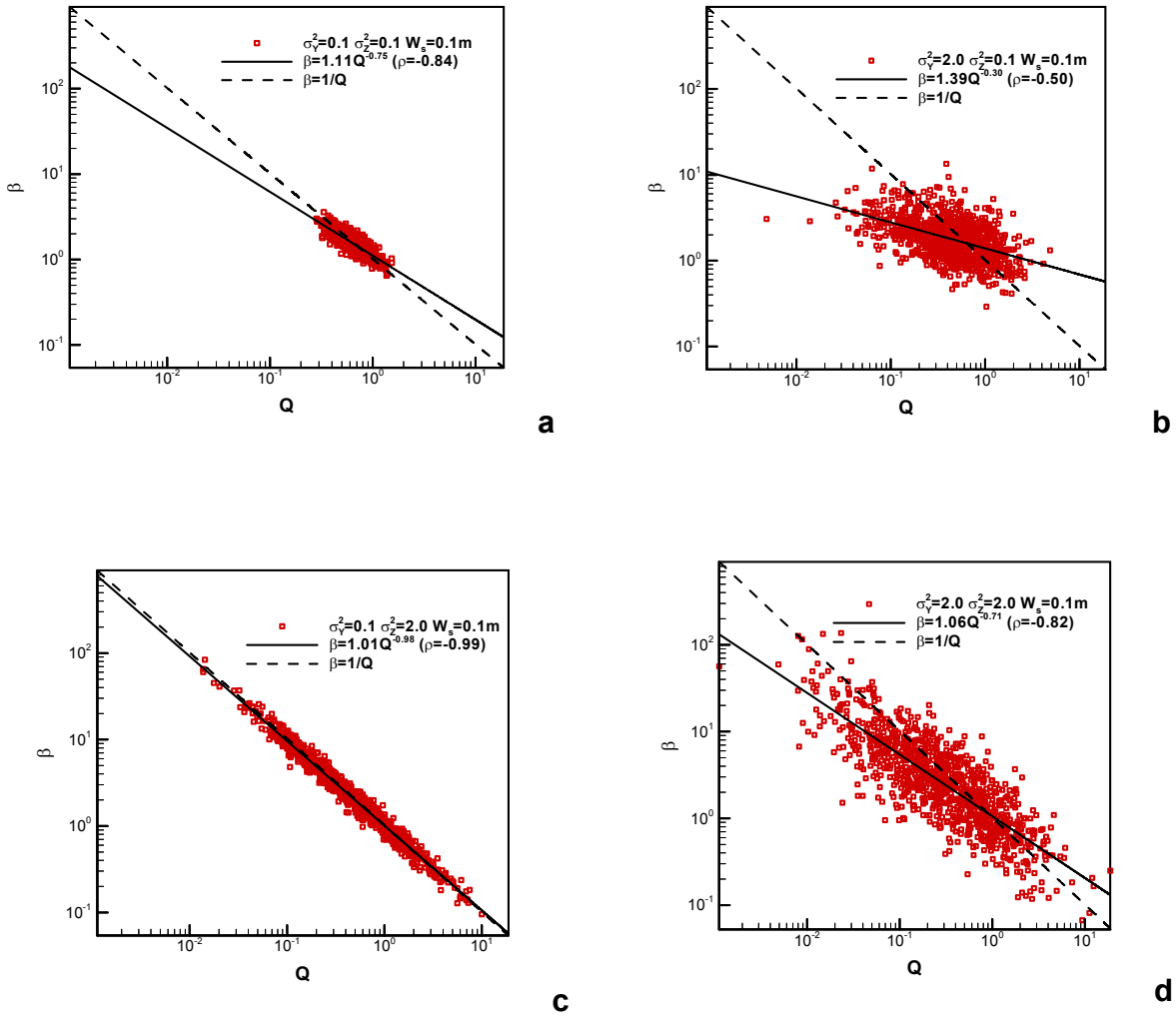

Figure 7-4. *Scattergram of normalized β and Q for the four cases considered in Table 7-3 and for W=0.1 m: (a) Case 1; (b) Case 2; (c) Case 3; and (d) Case 4. Solid lines are the best power-law fits. Dashed lines are analytical solution (7-2).*

8 Discussion and conclusions

8.1 Summary and discussions of the results

8.1.1 Flow-dependent parameters

The water residence time distribution $g(\tau)$ is first determined by deconvoluting BTCs of conservative tracers, while accounting for the diffusion into the rock matrix in Task 6D. The actual form of $g(\tau)$ is usually assumed to be inverse-Gaussian or lognormal. The first two statistical moments of the water residence time are then calibrated for each flow path.

Alternatively the values of transmissivity (T) of a fracture (or a fracture network), and boundary conditions are used in the Monte-Carlo numerical simulations to infer the first two statistical moments of τ, as we did in Task 6E. It should be noted that the data points measured in the fields are usually extremely scarce (only a few for the entire flow path in most of the cases), the statistical inference may not be very reliable and the uncertainties involved are large.

Previous numerical simulations have indicated that hydrodynamic control parameter β is closely correlated to the water residence time τ (Cvetkovic et al., 1999; Cvetkovic et al., 2000; Cheng et al., 2003; Cheng, 2005). In general the correlation between τ and β is nonlinear and follows a power-law. However, in this study correlations of τ and β is approximately linear, as is evidenced by the τ - β scattergrams (Figures 3-14 to 3-16).

By assuming an inverse-Gaussion distribution for τ. The distribution of β is also expressed by the distribution of τ through the linear τ - β relation.

8.1.2 Interpretation of the immobile zones in the rock matrix

The fracture coating is viewed as the fracture surface. We assume that the coating is evenly distributed on both sides of the fracture surface with a thickness of 0.25 mm on each side. The surface sorption coefficient K_a is calculated based on the distribution coefficient K_d for the coating.

There are two types of structures consisting of different retention zones: Type 1 and Type 2. In structure Type 2, there are only the altered zone and the intact rock in the rock matrix. The altered zone and the intact rock are both assumed evenly (symmetrically) distributed on both sides of the fracture immediately adjacent to the fracture coating.

For a Type 1 structure the rock matrix consists of four retention zones: the fault gouge, the cataclasite, the altered zone and the intact rock. It is unlike that the fault gouge is located solely on one side of the fracture while the cataclasite on the other side. In lack of any accurate information, we assume that the fault gouge and the cataclasite distribute alternatively on the two sides, with each side having 50% of the fault gouge and 50% of the cataclasite.

8.1.3 Complexity factor

We have accounted for the complexity factors in our Task 6E modeling. We calculated the average percentage of each structure type along a flow path. At x = 1920 m, we have an average geological class of 1.88, an average complexity factor of 2.12 with 17.2% of the Type 1 structure and 82.8% of the Type 2 structure. This implies that the flow paths from the injection section up to x = 1920 m are mainly made up of Type 2 structures. If we further track the tracers to x = 1880 m, we have more of the Type 1 structure (59.6%) and less of the Type 2 structure (39.4). The average geological type has decreased to 1.29. If we continue tracking the tracers to the west boundary, we have even more of the Type 1 structure (70.4%) and less of the Type 2 structure (29.6%). The average geological type has also decreased to 1.18.

8.1.4 Heterogeneity of retention parameters

The material retention parameter group κ for a given tracer by definition is determined by the porosities θ and the sorption coefficients K_d of the various retention zones a tracer has penetrated. However, the penetration depth is not known *a priori*. We need to know the times when most mass is recovered in order to calculate the penetration depth.

For the two fracture types, the porosity θ and the K_d profiles are already given in terms of the values in their various retention zones. An effective porosity has been obtained for each structure type by scooping calculations of the penetration depths of the various tracers and by taking an average value among the different retention zones of the different tracers based on the 85% recovery times from the modelled BTCs.

8.1.5 Results of Task 6D

From particle tracking simulations two main flow paths are obtained: one run only through the four deterministic structures (involving 69% of total particle trajectories) and the other runs mainly through the background fractures (31% of the total trajectories). The water residence time distribution and the distribution of β parameter are also obtained. The simulated distribution of water residence time has approximately a shape of inverse-Gaussian, while the peak is higher than the fitted inverse-Gaussian distribution. The distribution of the simulated β did not show a definite trend.

We have considered six tracers in the model: I-129, Ca-47, Cs-137, Ra-226, Tc-99 and Am-241. The modelled breakthrough curves (BTCs) for both the experimental injection and the Dirac pulse injection are provided and based on the parameters obtained by calibration on the measured BTCs. The times of 5%, 50% and 95% mass recovery are also provided.

The effects of discretization on the modelled BTCs have been investigated by comparing the τ and β moments and the modelled BTCs with different types of discretization. With a coarser discretization the mean of the water residence time becomes shorter and the variance larger. It therefore yields BTCs that arrive earlier, spread more widely and have higher peak values.

The effects of the background fractures have also been studied. If the particles are only transported through the network of the deterministic structures, the mean of the water residence time also becomes shorter but the variance is about the same as in the case with all structures. This yields BTCs that arrive earlier, but the effects are less profound than those caused by discretization.

In both comparisons the tails of the calculated BTCs are relatively close to each other in different cases since the tails are largely determined by the injection function.

The penetration depth by diffusion of the tracers over the time scale of Task 6D has been calculated. The penetration depth seems to be tracer-dependent, i.e., tracers penetrate different parts of the rock matrix. As the part of the rock matrix close to the fracture surface has larger porosity, the sorbing tracers that can penetrate only into this part encounter regions of larger porosities. The modelled BTCs with varying porosities deviate from those with constant porosities but not significantly.

8.1.6 Results of Task 6E

From particle tracking simulations the flow paths are obtained at three control planes. The water residence time distribution and the distribution of β parameter are also obtained at those three CPs. The simulated distributions of water residence time have approximately a shape of inverse-Gaussian (or log-normal). The distributions of the simulated β have also approximately a shape of inverse-Gaussian (or log-normal).

We have considered six tracers in the model: I-129, Ca-47, Cs-137, Ra-226, Tc-99 and Am-241. The modelled breakthrough curves (BTCs) for both the extended pulse injection and the Dirac pulse injection are provided based on the parameters obtained by the penetration profiles. The times of 5%, 50% and 95% mass recovery are also provided.

The penetration depth by diffusion of the tracers over the time scale of Task 6E has been calculated. The penetration depth seems to be tracer-dependent, i.e., tracers penetrate into different parts of the rock matrix. As the part of the rock matrix close to the fracture surface has larger porosities, the sorbing tracers that can penetrate only into this part encounter regions of larger porosities.

8.2 Main conclusions

1. The semi-synthetic hydro-structural model developed in Task 6C has provided a good basis for Task 6D and 6E modelling.

2. Depth-wise heterogeneity of the retention parameters may have consequences for the evaluation of the retention of different tracers in the rock matrix. Considerable deviation from real situations may result if one single value of "representative" porosity is used for all tracers.

3. The effects of discretization and background fractures on modelled BTCs are appreciable in Task 6D modelling. However the results were based on two-step flow simulations and further investigations may be conducted directly with a single-step approach on 200m blocks.

4. The Monte-Carlo simulations at three control planes (x=1920m, 1880m and 1800m) for Task 6E indicate a linear trend for the τ-β relationship. The simulations also give a range of the slope k from 9420 to 12380 m^{-1} if we assume τ=kβ applicable for the three control planes. However, more extensive simulations which combine full discrete fracture network modelling with internal fracture variability, are required for quantifying β-statistics on large scales.

5. The probability distribution of τ and β has approximately a trend of lognormal or inverse-Gaussian distribution.

6. The modeling results for the PA modelling indicate that the retention in the unaltered rock is an important process in contrast to the SC time scale where the retention in the rim zone adjacent to the fracture is dominating.

8.3 Lessons learned and implications for Task 6 objectives

In the PA modelling, the water flow is assumed to occur under natural gradient boundary conditions giving water travel times corresponding to the "PA time scale", in contrast to that in the SC modelling where the flow is subject to an enhanced gradient of pumping. Both SC and PA modelling in Task 6 have been conducted in the same spatial scale defined in Task 6C.

The LaSAR approach was developed in generic flow fields, and has been applied to both SC modelling and PA modelling in Task 6. The modellings have been implemented in terms of setting up different boundary conditions for flow in both SC and PA.

Regarding the objectives of Task 6, the following implications can be obtained:

- As the detailed LaSAR model is used in this report, and the PA modelling is forward modelling and the SC modelling is inverse modelling, it is generally difficult to justify whether the simplifications made in the PA modelling are legitimate or not.

- The flow experiment and tracer test can, to some extent, provide constraints of the retention parameters to the PA modelling. For example, the fracture heterogeneity characterised by the transmissivity obtained in flow experiments can provide insights to the PA modelling concerning the parameters of residence time, the τ-β relation, and the stochastic approach, at least qualitatively. On the other hand, when the time scales of the SC and the PA modelling are concerned, it might be more likely that the SC experiments and modelling will better provide the lumped effect of the different retention mechanisms rather than the detailed resolution of the contribution of each mechanism to the retention.

- The Task 6 modelling has also indicated that the SC experiments and modelling need to focus on the understanding of different retention mechanisms, especially on the long term effects of these effects. It should be noted that this understanding might be limited by the short time scale involved in the SC analysis.

- The spatial variations of the retention properties seem to be more readily characterised in the SC than the temporal effects of these retention properties.

9 References

Andersson, P:, Byegård, J., Dershowitz, B., Doe, T., Hermanson, J., Meier, P., Tullborg, E.-L., and Winberg, A. (2002a). TRUE Block Scale Project Final Report – 1. Characterisation and model development. Swedish Nuclear Fuel and Waste management Company (SKB), Technical report TR-02-13.

Andersson P., Byegård, J., Holmqvist M., Skålberg M., Wass, E.,and Widestrand H., (2001). Tracer test stage-Tracer tests, Phase C, Swedish Nuclear Fuel and Waste management Company (SKB), International progress report IPR-01-33.

Andersson P., Byegård, J., Nordqvist R., and Wass, E., (2005). TRUE Block Scale Continuation, BS2B tracer tests with sorbing tracers. Swedish Nuclear Fuel and Waste management Company (SKB), International progress report IPR-05-01.

Andersson, P:, Byegård, J., and Winberg, A. (2002b). TRUE Block Scale Project Final Report – 2. Tracer tests in the block scale. Swedish Nuclear Fuel and Waste management Company (SKB), Technical report TR-02-14.

Andersson P., Johansson H., Skarnemark G., Skålberg M., and Wass E., (1999). TRUE 1st stage tracer test programme. Tracer tests with sorbing tracers, STT-1b. Experimental description and preliminary evaluation. Swedish Nuclear Fuel and Waste management Company (SKB), International progress report IPR-99-12.

Andersson P., Ludvigsson, J-E, Wass, E.,and Holmqvist M., (2000a). Interference tests, dilution tests and tracer tests, Phase A, Swedish Nuclear Fuel and Waste management Company (SKB), International progress report IPR-00-28.

Andersson P., Wass, E., Holmqvist M., and Fierz T., (2000b). Tracer tests, Phase B, Swedish Nuclear Fuel and Waste management Company (SKB), International progress report IPR-00-29.

Benabderrahmane, H., Dershowitz, W.S., Selroos, J-O., Uchida, M. and Winberg A., (2000). Task 6 proposal - Performance Assessment Modelling Using Site Characterisation Data (PASC). Unpublished proposal to the Äspö Task Force, November 2000.

Bäckblom, G., and Olsson, O., (1994). Program for tracer retention understanding expeiments, SKB HRL Progress Report, PR 25-94-24.

Cheng (2005). Hydrodynamic control of retention in heterogeneous aquifers and fractured rock. Doctoral thesis. Royal Institute of Technology, Stockholm, Sweden.

Cheng, H. and Cvetkovic V. (2003), Modelling of sorbing tracer breakthrough for Tasks 6A, 6B and 6B2. Swedish Nuclear Fuel and Waste Management 7Company (SKB). Äspö Hard Rock Laboratory. International Progress Report IPR-04-30.

Cheng, H. and Cvetkovic, V. (2005). Evaluation of the BS2B sorbing tracer tests using the LASAR approach. TRUE Block Scale Continuation Project. Swedish Nuclear Fuel and Waste Management Company (SKB). International Progress Report IPR-05-39.

Cheng H., Cvetkovic V. and Selroos J.-O. (2003). Hydrodynamic control of tracer retention in heterogeneous rock fractures. Water Resour. Res., 39, 1130-1139.

Cvetkovic V. and Cheng H., (2002). Evaluation of block scale tracer retention understanding experiments at Äspö HRL. Swedish Nuclear Fuel and Waste ManagementCompany (SKB). Äspö Hard Rock Laboratory. International Progress Report IPR-02-33.

Cvetkovic, V., Cheng, H., and Selroos, J.-O., (2000). Evaluation of Tracer Retention Understanding Experiments (first stage) at Äspö, International Cooperation Report, ICR-00-01, SKB.

Cvetkovic V., Painter S., Outters N. and Selroos J.-O. (2004). Stochastic simulation of radionuclide migration in discretely fractured rock near the Äspö Hard Rock Laboratory. Water Resour. Res., 40, W02404, doi:10.1029 /2003WR002655.

Cvetkovic, V., Selroos, J.-O., and Cheng, H., (1999). Transport of reactive tracers in rock fractures, J. Fluid Mech., 378, 335-356.

Dershowitz, B., Winberg, A., Hermansson, J., Byegård, J., Tullborg, E.-L., Andersson, P., and Mazurek, M., (2003). Task 6C. A Semi-synthetic model of block scale conductive structures at the Äspö HRL. Swedish Nuclear Fuel and Waste ManagementCompany (SKB). International Progress Report SKB IPR-03-13.

Frick, U., Alexander, W.R., Bayens, B., Bossart, P., Bradbury, M.H., Bühler, C., Eikenberg, J., Fierz, T., Heer, W., Hoehn, E., McKinley, I.G. and Smith, P.A., (1992). Grimsel Test Site : The radionuclide migration Experiment – Overview of investigations 1985-1990. NAGRA Technical Report NTB 91-04. NAGRA Wettingen, Schweiz.

Haderman, J. and Heer, W., (1996). The Grimsel (Switzerland) migration experiment : integrating field experiments, laboratory investigations and modelling. J. of Contaminant Hydrol., vol. 21, pp. 87-100.

Harbaugh, A.W., Edward, R.B., Marry, C.H., and Mcdonald, M.G., MODFLOW-2000, (2000). The U.S. Geological Survey Modular Ground-water Model – user guide to modularization concepts and the ground-water flow process. U.S Geological Survey, OFR 00-92.

Heer, W. and Smith, P.A. (1998). Modelling the radionuclide migration experiments at Grimsel. What have we learned? Mat. Res. Soc. Proc., vol. 506, pp. 663-670.

Elert, M., and Selroos, J.-O., (2001). Task 6B2 modelling task specification, SKB.

Elert, M., and Selroos, J.-O., (2002). Task 6D modelling task specification, version 1.0, SKB.

Elert, M., and Selroos, J.-O., (2004). Task 6E modelling task specification, version 3.0, SKB.

Kulmala, S., Hakanen, M. (1995). Sorption of alkaline-earth elements Sr, Ba and Ra from groundwater on rocks from two investigation areas, Report YJT-95-03, Nuclear Waste Commission of Finnish Power Companies.

Mose, R., Siegel P., and Ackerer P., (1994). Application of the mixed hybrid finite element approximation in a groundwater flow model: Luxury or necessity?, Water Resour. Res., 30, 3001-3012.

Outters, N. and Shuttle, D., (2000). Sensitivity analysis of a discrete fracture network model for performance assessment of aberg. Report R-00-48, SKB.

Poteri. A., Billaux, D., Dershowitz, W., Gómez-Hernández, J-J., Cvetkovic, V., Hautojärvi, A., Holton, D., Medina, A. and A. Winberg, (2002). Final Report of the TRUE Block Scale Project, 3. Modelling of flow and transport. Swedish Nuclear Fuel and Waste Management Company. Technical Report TR-02-15.

Selroos, J. O., and Cvetkovic, V., (1996). On the characterization of retention mechanisms in rock fractures, SKB Technical Report TR 96-20.

Selroos, J.-O., and Elert, M., (2001). Task 6A & 6B modelling task specification, SKB.

Winberg, A., Andersson, P., Hermanson, J., Byegård, J., Cvetkovic, V., and Birgersson, L., (2000). Äspö Hard Rock Laboratory, Final report of the first stage of the tracer retention understanding experiments. Technical report TR-00-07, SKB.

Winberg, A., Andersson, P:, Byegård, J., Poteri, A., Cvetkovic, V., Dershowitz, W., Doe, T., Hermanson, J., Gomez-Hernandez, J., J., Hautojärvi, A., Billaux, A., Tullborg, E.-L., Holton, D., Meier, P., and Medina, A., (2003). TRUE Block Scale Project Final Report – 4. Synthesis of flow, transport and retention in the block scale. Swedish Nuclear Fuel and Waste management Company (SKB), Technical report TR-02-16.